# MICROSTRUCTURAL CHARACTERIZATION AND MODELLING IN PRIMARY CRYSTALLIZATION

Pere Bruna Escuer

Co-directors: Daniel Crespo Artiaga & Eloi Pineda Soler

Programa de doctorat de Física Aplicada i Simulació en Ciències

Universitat Politècnica de Catalunya

Barcelona, octubre del 2007

*Als meus pares,*

*sense el sacrifici dels qual no estaria on estic.*

## Agraïments institucionals

Aquest treball no hauria pogut ser realitzat sense la financiació d'una beca FPU del programa 2000 concedida pel Ministerio de Educación, Cultura y Deportes, els projectes CICYT MAT1998-0672-C02-02, MAT2001-00957 i MAT2004-01214 i els projectes de la Generalitat de Catalunya 2001SGR00190 i 2005SGR00201.

## Agraïments personals

En primer lloc haig de transmetre el meu més profund agraïment a en Dani Crespo, per haver confiat en mi des del primer moment que vaig entrar al seu despatx per preguntar-li si podia dirigir-me la tesi. Des d'aleshores, i a pesar de les meves errades, sempre ha estat al meu costat, tant professionalment com personalment. És un autèntic plaer poder treballar al seu costat, aprendre continuament de la seva experiència i gaudir de la seva amistat. Així mateix, poder compartir tots aquests anys amb l'Eloi Pineda, primer tots dos com a doctorands i ara ell com a co-director meu, ha estat una oportunitat única. Hem passat moltes hores junts, per l'escola, durant els congressos i sempre, fos quina fos la conversa que mantinguessim, sempre he après i he rigut molt. I no només he après de ciència, sinó també sobre moltíssims altres temes, sempre des de la seva molt lúcida visió del món en el que vivim. No exagero si dic que sense l'Eloi aquesta tesi no hauria pogut existir. També ha sigut molt important el paper de la Trinitat Pradell, amb qui havia de fer inicialment la tesi sobre espectroscopia Mössbauer. Ella m'ha ensenyat tot el que se sobre aquesta tècnica i sobre totes les altres tècniques habituals de caracterització de materials i gràcies a això he pogut mantenir una línia de recerca paral·lela que m'ha permès conèixer a molta gent interessant de molt diversos àmbits de la ciència, amb l'enriquiment personal que això suposa. Però en el grup de recerca no només hi som nosaltres tres, també vull agraïr aquesta tesi a en Víctor Garrido, que encara que no ens veiem sovint sempre t'alegra el dia amb el seu bon humor i amb la seva passió per la física (o hauria de dir per les matemàtiques?) i que sempre recordaré com la persona que em va deixar el primer llibre de Kierkegaard que he llegit. I a en Pep Rojas, que m'està mostrant com un enginyer aeronàutic pot sobreviure envoltat de físics. També voldria mencionar a José Calderón i a Mónica Popa, que sempre han mostrat una bona professionalitat i que s'han vist inmersos en unes circumstàncies incomprensibles.

En la vida ha d'haver temps per tot, no només per treballar i aquests moments d'oci que em permeten relaxar i disfrutar del dia a dia no serien possible sense la presència dels meus amics. Ells són els que m'han aguantat durant aquests anys d'elaboració de la tesi, els que m'han recolzat quan ho he passat malament i sobretot ells són els que fan que la vida valgui la pena ser viscuda. Tinc molta sort de tenir els amics que tinc i a ells també els hi vull agraïr aquest primer llibre. A en Paco, pel seu somriure burleta aquell llunyà dia en què li vaig fer una pregunta sobre sistemes de referència inercials a primer de carrera, somriure que va ser el principi d'una llarga i bonica amistat. A l'Oliver, el que sempre està bé, el que sempre té una rialla a punt i amb qui sempre et sents molt bé al seu costat, una persona amb moltes facetes totes elles dignes de conèixer. A la Maite, pel seu curs de socialització i les moltes hores compartides al llarg d'aquests anys, pels seus consells i per entendre'm tant bé. A en Marc, pel nostre viatge a Nova Anglaterra amb la Maite, per les nostres excursions per la muntanya, per la seva sinceritat i pels nostres silencis compartits. A en Raimon i la Rosario (i en Pau) per tenir sempre obertes les portes de casa seva i per la seva alegria. Al Lluis, amb qui no em veig gaire sovint, però amb

qui comparteixo una amistat reforçada per les viscissituds viscudes. A l'Eva, persona molt especial que em va ensenyar una nova manera d'enfocar el món, que literalment va canviar la meva vida obrint una porta que creia tancada, que té l'enorme paciència d'escoltar les meves cabòries i que sempre em fa les preguntes correctes. A la Clara, pel seu coratge i la seva lucidesa i per ajudar-me sempre a trobar la perspectiva adient. Al Tito pel seu humor absurd que tants bon moments ens fa passar. A l'Esteban per les fantàstiques digressions que sempre em sorprenen i em deixen meravellat. Al David, per la seva demagogia, la seva passió per la vida, el seu bon humor i el seu sentit de la responsabilitat. Al Pablo, amb qui no comparteixo moltes opinions però amb qui passo bones estones tot dinant. A l'Adeline, amb qui he compartit moltes hores de tren, dinars i sopars i que sempre em sorpren amb la seva afició als esports més estranys. A la Mònica, per les sessions de cine viscudes plegats, pels llibres recomanats i el seu sentit comú. Al Jordi Mazón, per les converses mantingudes els divendres a la tarda, per les assignatures compartides, per la seva passió per la meteorologia i la docència i per les coses que aprenc d'ell. I a la Iolanda, companya de despatx, autora de la portada d'aquesta tesi, per mostrar-me una visió alternativa de la societat en què vivim, per ensenyar-me que un món millor és possible i que encara està ple d'injusticies, per escoltar les meves confidències i pels seus bojos consells. Gràcies a tots. A tots vosaltres voldria dir-vos moltes més coses, i molt del que dic d'uns ho diria també dels altres, però ja em coneixeu, soc un home de poques paraules i prefereixo mostrar-vos el meu agraïment estant al vostre costat, cultivant aquesta amistat que em resulta tant preciosa i ajudant-vos sempre en el que bonament pugui.

Hi ha altres persones amb qui m'he trobat al llarg d'aquest camí que és la vida, persones que han sigut molt especials per uns motius o altres, i amb qui ara mantinc una bona relació d'amistat, una simple relació freda i professional o que s'han perdut en el tel boirós, a vegades incomprensible, de les relacions humanes. Per això també vull agraïr aquesta tesi a la Muriel, per les moltes hores compartides, el seu humor surreal i la seva visió de la vida; a la Luisa, per rescatar-me en un moment molt difícil de la meva vida i que em va mostrar el món de la immigració sudamericana al Japó; a l'Alba pel petit tros de vida que vam fer junts i a la Dorofia pels somnis que malauradament no vam poder fer realitat.

No em vull oblidar de persones que potser no han sigut tant importants com les esmentades anteriorment però que han fet que el meu dia a dia fos també més agradable. Als companys passats i presents de l'ESAB: Dani, Quim, Gerard, Roger i Marta. A la Karina pel nostre treball plegats. A en Joakim, a la gent de la UAB que em van acollir amb els braços oberts: Joan, Aitor, David i Marta, al Nick que no és responsable del meu baix nivell d'anglès, a la Pilar i el Jordi per sempre estar disposats a donar-me un cop de ma en tasques de coordinació, a en Fernando i a en Toni pel seu inestimable suport informàtic, a la Cesca per acollir-me al Campus Nord i a qui ara puc tornar el favor acollint-la a Castelldefels, al Ricard per deixar-me el seu codi phase-field i ensenyar-me'n els rudiments, als matemàtics que he conegut recentment, especialment la Maite i l'Anna, però sense oblidar la Isabel, la Sònia, l'Abel i l'Oscar i finalment a l'administració

del departament, especialment a la Silvia, per tractar-me sempre tant bé. I a ells no els he conegut, però sens dubte la meva vida seria més avorrida sense el suport moral de Fiodor Dostoievsky, Albert Camus, Woody Allen, Ingmar Bergman i Stanley Kubrick. A ells també els hi agraeixo aquest treball.

Però evidentment, aquesta tesi està especialment dedicada a les persones més properes que són les autèntiques responsables de la seva existència: la meva familia. A la iaia Carmeta, per estar sempre disposada a donar un cop de ma, a la iaia Carmen i a l'avi, que tot i que ja no hi són entre nosaltres mai els podré oblidar, al Ramon per les nostres converses de diumenge a la tarda, al meu germà i mestre Jordi, sense la presència del qual no hauria arribat on soc i sobretot als meus pares, que han fet tot el possible per donar-nos a mi i al meu germà el millor de tot, moltes vegades sacrificant-se per nosaltres. Gràcies.

# Contents

# Chapter 1

# Introduction

In the eigthies, a new field of reasearch appeared in materials science: metallic glasses. These materials are usually obtained from fast solidification, with cooling rates as high as $10^6$ $K/s$, of metal-non metal alloys or from mechanical alloying. The topology of the resultant product is similar to the one found in the liquid state of the same material, that is, with short-order spatial atomic correlations (around 5Å). Because of that, these materials are also refered as amorphous materials. Their importance lies in its excellent magnetic properties (if in their constituents there are ferromagnetic elements [1]-[7]) and mechanical (mainly with Al based glasses [8, 9]). The main disadvantge, that in turn avoids the use of these materials in the industry, is their thermal unstability because the undercooled state is metastable and then, any contribution of thermal energy is able to activate the solid state processes like the diffusion of some of the constituent species, that results in the atomic ordering and the subsequent cristallization of the material. In many cases, the crystalline phase that appears does not transform completely the material; is a primary crystallization that can be followed by the precipitation of a second phase at higher temperatures. Thus, the study of the materials obtained from the heat treatment of metallic glasses was initially devoted to prevent its crystallization or to delay it to higher temperatures. From these studies it was discovered that these partially crystallized materials had properties as good or better as their amorphous precursors and with the advantage of being thermally stable. The reason for the good properties of these kind of composite materials lies in the size of the crystals that grow in the amorphous matrix and that are usually of nanometric scale (tipically between 20 and 50 $nm$ [10, 11]). These partially crystallized materials with appropriated compositions allow to obtain materials that exhibit useful mechanical properties (increased ductility, increased flow stress and fracture strength and superplasticity [12, 13]) as well as hard and soft-magnetic properties (low coercivity, high saturation magnetization, reduced high frequency losses and stress-induced anisotropy [1, 14, 15]). In general, composite materials are multiphase mixtures that are technologically important because they can be produced with a wide variety of components to obtain a desired set

of properties. They usually consist in a phase embedded in a matrix which can have different composition, different crystalline phase or can be amorphous. Some examples are graphite fibers in an Ag-Cu alloy matrix where the fibers are used to control the mechanical properties of the matrix or steels composed of several phases like cast irons which are a mixture of graphite, bainitic ferrite, martensite and austenite and that are useful for car part fabrication due to its optimal combination of ductility, thermal conductivity and low weight [16, 17]. Some examples of composites with a metallic amorphous matrix and with actual industrial applications are materials with compositions based on Fe-Nd-B that with its excellent hard magnetic properties are widely used as permanent magnets and the so-called FINEMET (materials based on Fe-Si-B-Nb-Cu), NANOPERM (Fe-Zr-B-Cu) and HITPERM (Fe-Co-Zr-B-Cu) used in choke coils or as high-frequency transformer cores due to its soft magnetic properties.

A common feature of all these materials is that their macroscopic properties strongly depend on their nanostructure. Thus, it is crucial to have general theories able to predict the developed microstructure as a consequence of a particular heat treatment and to explain the relation between that microstructure and the observed macroscopic properties. One of the main factors to predict the microstructure is the kinetics of these transformations. The formation mechanism of nanomaterials from the controlled heat treatment of metallic glasses follows a nucleation and growth kinetics. The thermodynamic fluctuations induce the appearance of nuclei that grow until they impinge, directly or indirectly throuhg their concentration gradients. Thus, the kinetics corresponds to the phase crystallization in an undercooled liquid and is studied in the framework of first-order phase transitions. Accordingly, the KJMA model is a commonly used tool to describe the nanocrystallization process and it relates the global kinetics of the system with the parameters that control the transformation, namely, the nucleation and the growth rates. But this model has some limitations [18, 19, 20] that make unclear its validity in these transformations. Extensions of this model must be developed or other tools used, as for example, phase-field model simulations that allow to solve the diffusion equation in all the space yielding the kinetics of the transformation as well as the generated microstructure.

The aim of this thesis is to study the kinetics of primary crystallization in metallic glasses by means of phase-field model simulations. Simulation results will be compared with KJMA-based models and will allow us to introduce a new mechanism that may have an important role in the nanocrystallization process and that are not described by any previous model. In this introductory chapter, the description of primary crystallization is presented. First of all, the formation mechanism of a glass will be shown. Then, the nucleation and growth process that leads to the partial nanocrystallization of a metallic glass is described. The KJMA model is introduced, as well as the extensions of this model that, in principle, circumvent some of its limitations. The phase-field model technique is described and a brief introduction of diffusion in liquids and amorphous solids is presented for the importance that diffusion has in this kind of transformations. Finally a short description of the subsequent chapters of this thesis is presented.

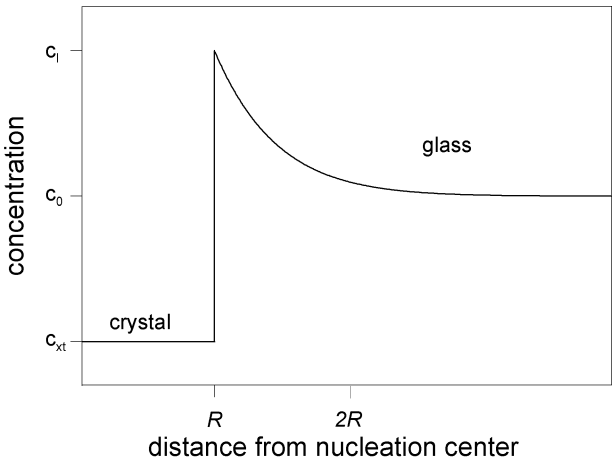


Figure 1.1: Composition profile expected surrounding a primary crystal.

## 1.1 Primary crystallization

Glasses are metastable materials that can devitrify through several reactions, being the driving force the free energy difference between the glass and the correspondent crystalline phase. If the product phase has the same composition from that of the glass, the transformation is called polymorphous. If several stable phases can exist in the system, the glass can reduce its free energy crystallizing simultaneuosly these stable crystalline phase in a similar way as an eutectic crystallization; it is called an eutectoid transformation. In a primary crystallization a phase of different composition from that of the glass is formed with a composition $c_{xt}$ which is less than that of the glass $c_0$. Thus, a concentration gradient is stablished between the new grain and the remaining glass the composition of which evolves towards the equilibrium concentration between the glass and the primary crystal $c_l$. A sketch of the formed concentration profiles can be seen in figure 1.1 and the relation between $c_0$, $c_{xt}$ and $c_l$ can be stablished through the appropiate free energy diagram as the one shown in figure 1.2. In general, the growth of these primary crystals can appear from a liquid, a crystalline solid solution or a glass. We will focus our attention in the nanostructured composites generated from the primary crystallization of a glass, thus, it is important to know how to synthesize glasses. The key point is to circumvent the crystallization process cooling the liquid rapidly enough. That this is possible can be easily seen looking to a schematic time-temperature-transformation (TTT) diagram (figure 1.3); in this kind of diagrams the time needed to begin the crystallization is represented as a function of the temperature and an essential feature is that as the liquid is cooled down below the equilibrium melting point $T_m$, the onset of the crystallization does not accelerate indefinitely but reaches a maximum at a temperature $T_n$. This is the consequence of two competing

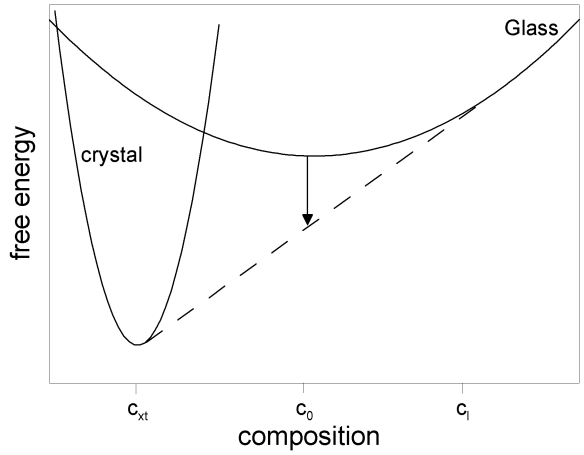


Figure 1.2: Hypothetical free energy diagram to illustrate a primary crystallization and showing the relationship between $c_0$, $c_{xt}$ and $c_l$

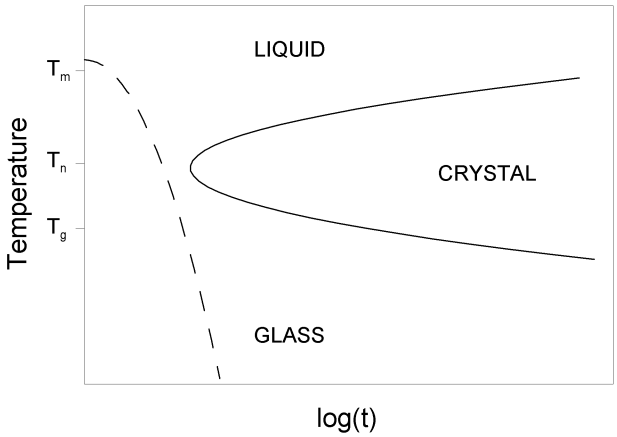


Figure 1.3: Schematic TTT diagram for crystal growth in an undercooled melt (continuous line) and a possible fast cooling path to form a glass (discontinuous line)

effects as the temperature is reduced: on the one hand the undercooling of the liquid, and hence the driving force for the crystallization, increases and on the other hand the mobility of the atoms diminishes due to the increase in the viscosity of the liquid that dominates at very high undercoolings, slowing down the beginning of the crystallization. Thus, if the liquid is quenched from above $T_m$ to well below $T_n$ in a time less than $t_{min}$(the minimum time for crystallization) the undercooled melt is retained and at the glass transition temperature $T_g$ the configuration of the liquid is frozen to form the glass. A possible cooling rate for forming a glass is showed in the figure in discontinuous line.

The range of compositions of alloys that can be vitrified depend on the production method; glass formation is assured if the still uncrystallized liquid is cooled to the glass transition temperature $T_g$, hence it is expected to obtain a glass in those compositions for which the liquid is relatively stable with respect to the crystalline phases, that is near deep depressions in the liquidus (eutectic points). There is a correlation between the glass forming ability (GFA) of a system (the ability of a liquid to cool without crystallization) and the reduced glass temperature $T_{rg} = \frac{T_g}{T_l}$ (being $T_l$ the liquidus temperature): the higher the $T_{rg}$ the higher the GFA. Metallic glasses that are good glass formers have typical values of $T_{rg}$ around 0.6. Factors that can enhance the GFA of an alloy are, for example, the enthalpy of formation, relative size of the constituent atoms, electron concentration and electronegativity differences between the components.

Let's see in more detail the transition from a liquid cooled below its melting temperature to the glassy state and how is the crystallization kinetics from this state.

### 1.1.1 Supercooled liquids and glasses

A supercooled liquid is a liquid that remains uncrystallized below $T_m$. The specific volume, the entropy and other thermodynamic properties of the supercooled liquid are those expected from the extrapolation to slower temperatures of the liquid properties above $T_m$. The crystallization of a liquid below $T_m$ is a first-order phase transition and hence it results in discontinuities in some properties like the entropy or specific volume. In contrast, as a supercooled liquid is cooled to lower temperatures, its atoms move more and more slowly due to the increase of viscosity of the liquid. If we look, for example, at the specific volume $v$, at some temperature the atoms do not have the possibility of arranging themselves in order to attain the new equilibrium value of $v$ before the temperature is lowered further, and hence the experimental values of $v$ begins to deviate from the equilibrium values (see figure 1.4). The structure of the material is frozen in the time scale of experimental observations, and we call it a glass.

The glass transition temperature $T_g$ is defined as the temperature at which the viscosity $\eta$ of the liquid is $\eta = 10^{13}\, Poise$. Another usual way of defining $T_g$ is through the thermal expansion coefficient (that is $[d(ln\, v)/dT]_p$) that changes smoothly during the glass transition, defining a range of temperatures called the glass transformation range [21]. Hence, in order to characterize a glass, the fictive temperature $T_f$ has been defined as the temperature at which the

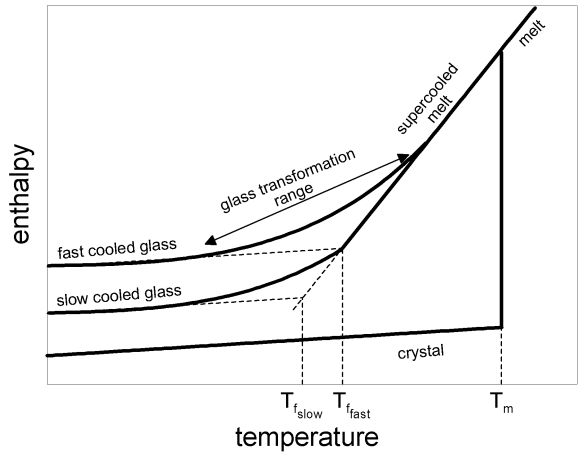


Figure 1.4: Effect of the temperature in the enthalpy (and hence in the volume) of a glass forming material

intersection between the equilibrium value of the entropy (or the specific volume) in the supercooled liquid and the corresponding value in the glass state occur. But defined in this way, $T_g$ is different for different cooling rates: slower cooling rates allow the liquid to stay in the supercooled state until lower temperatures.

The nature of the glass transition is not fully understood [21, 22]; but it is important to emphasize the fact that the supercooled liquid is a metastable state while the glass state is unstable, in the sense that for a single component glass at constant $P$ and $T$, the Gibbs free energy will not be in a minimum. Hence, the glass is continually relaxing towards the local free energy minimum but at time scales impossible to measure.

It is also of interest to know how is the dynamics of the liquid as $T_g$ is approached. The viscosity of a liquid increases considerably near $T_g$; however this change is not universal but a function of the supercooled liquid. A magnitude directly related to the viscosity is the relaxation time, that is, the time needed for the molecules of the liquid to recover its original state after the action of some perturbation like and electric field or an applied stress: the more viscous is the liquid, the larger is the relaxation time. Accordingly, there are *strong* and *fragile* supercooled liquids. *Strong* liquids have relaxation processes that follows an Arrhenius law while *fragile* liquids have non-Arrhenius relaxation processes. Canonical examples of this classification are the $SiO_2$ as *strong* and the *o-terphenyl* as *fragile* (figure 1.5). The temperature dependence of relaxation times or the viscosity for supercooled liquids is often described by the Vogel-Tammann-Fulcher (VTF) equation [23, 24, 25]:

$$\eta = A_0 exp\left(\frac{B_0}{T - T_0}\right) \tag{1.1}$$

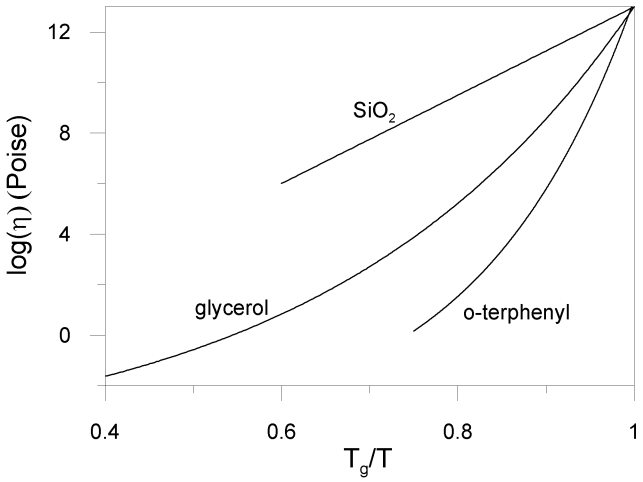


Figure 1.5: Viscosity as a function of reduced inverse temperature for three liquids (from [21])

where $A_0$ and $B_0$ are temperature independent but composition dependent positive constants [26] and $T_0$ is the temperature at which the viscosity is predicted to be infinite. Hence $T_g$ is always greater than $T_0$. If $T_0 = 0$ the Arrhenius equation is recovered.

### 1.1.2 Structural relaxation and crystallization in metallic glasses

As stated before, the glassy state is unstable; therefore, when a glass is annealed below $T_g$ to the glass transformation range it may undergoes a transformation to a more stable glass in which there is a readjustment of the structure reducing its volume. This process is called structural relaxation and notwithstanding that the change in the density during this process is small (usually less than 1%), there could be important changes in the viscosity or the ductility of the glass and also in its magnetic, electric, elastic and diffusion properties [27]. It is also possible that a glass relaxes to its supercooled liquid state, a process called super-relaxation [28].

The structural relaxation process is different depending on the annealing temperature $T_a$. Well below $T_g$ some atomic ordering occurs locally in a more or less rigid matrix while near $T_g$ a long range relaxation that reduces the structural heterogeneity of the glass takes place. For example, in the $PdCuSi$ system, these two temperature regions are $T_g - 200K < T_a < T_g - 100K$ in the first case and $T_a > T_g - 100K$ in the second case [27]. And the extent in which some of the properties of the glass changes during the structural relaxation also depends on its thermal story and hence on the way it was produced.

A particular class of glasses, and the focus of this thesis, are metallic glasses that in the last decades have been produced in a wide range of compositions not only for its practical applications and fundamental interest but also as precursors for new nanocrystalline materials with useful properties. That is because crystalline products made from a glass may have a very fine and uniform microstructure that comes from the chemical uniformity of the glass. That fine microstructure is also a consequence of obtaining the crystals heating from the glass instead of cooling from the liquid, thus at the annealing temperatures the nucleation frequency is much higher than the growth rate, resulting in a fine dispersion of nanocrystals. The cooling rates needed to produce metallic glasses are between $10^4$ and $10^6$ K/s and they are usually obtained with the melt-spinning technique. But, there are also other possible techniques that include rapid liquid cooling (like melt-spinning [29]), undercooling of clean liquids (like fluxing [30]), physical vapor deposition (like sputtering [31]) or mechanical methods (like mechanical alloying [32]). More conventional solidification routes with slower cooling rates can be used in the so-called bulk metallic glasses produced with diameters as large as 40 mm using copper mold casting techniques [33]. These new glasses were developed recently and are intensely studied materials at present due to its excellent mechanical properties and its potential use in industrial applications (for a recent review in the subject see reference [34]).

In conventional metallic glasses, the crystallization temperature is very close to $T_g$, implying that super-relaxation is avoided in this case by the onset of crystallization. However, it can occur in bulk metallic glasses due to its more stable undercooled melt [28].

The crystallization of metallic glasses occurs by a nucleation and growth process that is described subsequently.

### Nucleation

The driving force for the crystallization process is the Gibbs free energy difference between the amorphous phase and the corresponding crystalline phase. Heterophase fluctuations of density or concentration, that is, fluctuations that lead to local phase transformations, are the responsible for the nucleation process via the formation of energetically stable clusters, called nuclei.

The classical nucleation theory (CNT) was developed to study the condensation of supersaturated vapour by Volmer [35] and by Becker and Döring [36] and is the basis of all the classical theories devoted to the understanding of liquid-solid and solid-solid nucleation and growth transformations. In particular, the CNT with the pertinent adaptations has been extensively applied to the crystallization of amorphous phases. CNT treats the fluctuations as droplets of the new equilibrium precipitate phase $\beta$ embedded in the $\alpha$ amorphous matrix; in this model the interface between $\beta$ and $\alpha$ is assumed to be sharp and the droplet of the new phase $\beta$ is treated as having bulk properties and hence, its interfacial free energy and its Gibbs free energy can also be considered macroscopic in nature and then evaluated.

The formation of a spherical droplet with radius $R$ leads to a change of the

Gibbs free energy:

$$\Delta G(R) = \Delta g_{\alpha\beta} \frac{4\pi}{3} R^3 + 4\pi R^2 \sigma_{\alpha\beta} \tag{1.2}$$

where $\Delta g_{\alpha\beta}$ is the driving force per unit volume and $\sigma_{\alpha\beta}$ is the specific interfacial energy. The first term scales with $R^3$ and accounts for the reduction of free energy on forming the droplet and, hence, is negative, while the second term scales with $R^2$ and is the energy required to form the interphase boundary and, hence, is positive. As a consequence, $\Delta G(R)$ passes through a maximum at $R^* = \frac{2\sigma_{\alpha\beta}}{-\Delta g_{\alpha\beta}}$; therefore, only clusters with a radii greater than $R^*$ (critical radius) are predicted to grow continuously. This means that in order to become a critical nucleus, a fluctuation must overcome the activation barrier for nucleation, i.e., $\Delta G(R^*) \equiv \Delta G^*$. In solid-solid transformations, the change of volume that usually acompanies most phase transformation may have important effects, thus the associated strain energy is an important factor to consider in order to evaluate the probability of appearance of a new nuclei. In this kind of transformations, the driving force per unit volume will have two contributions: *(a)* $g_\beta - g_\alpha$, the difference between the free energies per volume of the bulk phases, and *(b)* $\Delta g_s$, the elastic energy per volume, mainly due to the different lattice parameters between the new phase and the amorphous matrix. As $\Delta g_s$ is positive, the elastic energy reduces the driving force of the reaction, and then, nucleation will not be possible unless $g_\beta - g_\alpha > \Delta g_s$. The importance of this elastic energy will be strongly dependent on the size and shape of the precipitating particles and the coherence or incoherence between the interface of the two phases, and hence, the treatment of each particular system must be done independently [39].

The nucleation frequency, i.e., the number of stable nuclei formed in the system in unit time, will depend on the number of clusters that become greater than the critical size after the incorporation of new atoms by a fluctuation. The CNT assumes that, even in the later stages of the transformation, there is a stationary distribution of clusters of the new phase embedded in the matrix and, hence, there is a constant flux of clusters with radii greater than the critical radius. This flux correspond to the nucleation frequency and can be calculated from the assumption of this stationary state and from the probability of existence of a cluster of a certain number of atoms in equilibrium [10, 37]:

$$I = 4 \left( \frac{\sigma_{\alpha\beta}}{RT} \right)^{\frac{1}{2}} N_v \nu exp \left[ -\frac{16\pi \sigma_{\alpha\beta}^3}{3RT(\Delta G^*)^2} \right] \tag{1.3}$$

where $N_v$ is the density of nucleation sites in the matrix and $\nu$ is the average frequency with which an atom crosses the interface in one direction. This frequency depends on the activation energy barrier to the addition and removal of atoms from clusters. Moreover, the presence of this activation energy may mean that there is a transient time before the formation of a cluster of certain size, and thus the stationary distribution of clusters is not attained instantly. This transient will only be important if the period of observation is of short duration

compared with it. Therefore, the nucleation frequency is time dependent and is commonly considered in terms of an incubation time $\tau$ as [38]:

$$I^*(t) = Iexp\left[-\frac{\tau}{t}\right] \tag{1.4}$$

with:

$$\tau \approx \frac{K}{\nu}\left(\frac{3\Delta G^*}{\sigma_{\alpha\beta}}\right)^2 \tag{1.5}$$

being $K \approx 3\text{x}10^{-4}$. If the steady-state is reached quickly compared to the global kinetic of the process, it can be said that a constant nucleation process takes place.

This steady-state nucleation rate implicitly assumes an homogeneous nucleation, but there are two factors that must be taken into account. Firstly, the presence of defects or impurities in the preexisting phase, because the presence of the walls of the defects reduces the interfacial energy due to the reduction of the surface and then, the defects act as nucleation centers. Secondly, in primary crystallization there is a difference in the concentration between the parent and the new phase, resulting in a concentration profile like the one sketched in figure 1.1. As it will be shown later, as the transformation proceeds there are changes in the matrix composition that lead to its progressive stabilization, thus resulting in a time dependent and composition dependent nucleation rate. Althouhg primary crystallization from a metallic glass is a transformation from a metastable to a stable phase, we will consider that the change in the free energy difference between the two phases due to these compositional changes can be calculated from the equilibrium diagrams and then, the nucleation rate becomes [40]:

$$I(c) = I_0 \exp\left\{-Q\left[\frac{1}{\ln^2\left(\frac{c}{c_l}\right)} - \frac{1}{\ln^2\left(\frac{c_0}{c_l}\right)}\right]\right\} \tag{1.6}$$

where $c$ is the time dependent concentration in the matrix, $c_l$ is its equilibrium concentration and $c_0$ its initial concentration. As the value of $c$ changes from $c_0$ to $c_l$ the nucleation rate goes from a maximum (at the beginning of the transformation) to 0 in the interface between the matrix and the precipitating phase. That induces an inhibition of the nucleation (sometimes called non-random nucleation) in the surrounding area of the growing crystallites, being the parameter $Q$ who determines the extent of this area (figure 1.6).

In many metallic glasses, the experimental densities of the crystallized nanostructures is of the order of $10^{20}$- $10^{23}m^{-3}$, much higher than the expected from the CNT. Therefore, the validity of the CNT for glassy systems has been questioned [41] and new mechanisms have been proposed, including icosaedral short-range order in the glass, quenched-in nuclei, heterogeneous precipitate formation, phase separation, the influence of composition and diffusion-controlled nucleation [42]. As the purpose of the present thesis is not to study the nucleation process in a primary crystallization, but the kinetics, the CNT will be assumed.

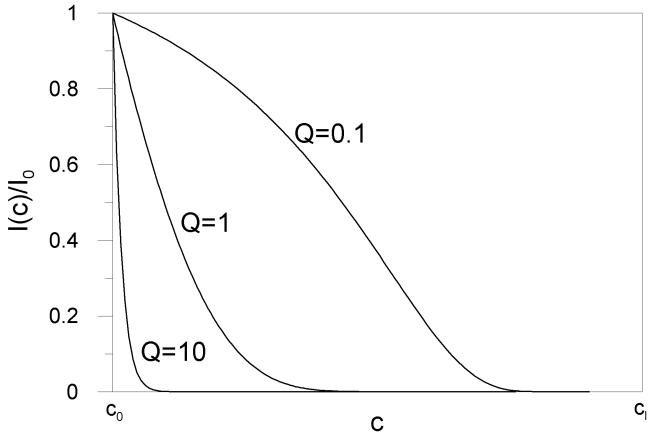


Figure 1.6: Nucleation rate as function of the concentration and the $Q$ value. Larger $Q$ values imply a smaller area where the nucleation is possible.

### Growth

In a primary crystallization, once a stable nucleus is formed it is embedded in an amorphous phase that initially is still supersaturated, then there is a concentration difference between the particle and its surroundings. Therefore, the growth of the nucleus takes place by two simultaneuos processes. On one hand, atoms move across the interface in order to reduce its Gibbs free energy. This movement depends on the interface mobility of the atoms. On the other hand, the concentration gradient between the crystallite and the amorphous phase gives rise the diffusion of the atoms to reduce this gradient, a process controlled by the diffusion coefficient. The growth will be controled by the slowest of these mechanisms.

It will be assumed that the growth of the particle is produced by the movement of one atomic species from the matrix (where it is in excess) to the crystallite[1]. At the beginning, the rate of attachment at the interface of the atoms of this species will be controlled only by its interface mobility. That process is interface-controlled. Once the particle has grown to a certain size the concentration of the species in the surroundings of the particle reaches the equilibrium concentration between the two phases $c_l$, value that depends on the curvature of the interface (Gibbs-Thomson effect). Therefore, the growth of the particle will still be due to the attachment of these atoms to the interface, but now it is controlled by the rate at which diffusion modifies the concentration at the surroundings of the particle. Hence, it is a diffusion-controlled process. The transition from one mechanism to the other depends on the relative magnitudes of the diffusion coefficient and the interface mobility.

[1]The description is analogous if one considers that the growth is due to the movement of one atomic species from the crystallite to the amorphous matrix (where it is deffective).

The interface-controlled growth is a process determined by the difference in the Gibbs free energy that can be considered constant as long as the transformation is possible; therefore, in this stage of the growth the particle radius grows at constant velocity.

The theoretical analysis of diffusion-controlled grain growth has attracted considerable attention for many years. Such analyses have to deal with the troublesome problem of resolving the diffusion equation in the matrix, while satisfying boundary conditions in the moving precipitate-matrix interfaces. The diffusion equation

$$D\nabla^2 c = \frac{\partial c}{\partial t}, \tag{1.7}$$

where $D$ is the diffusion coefficient (assumed independent of the composition), rules the evolution of the concentration field $c = c\left(\overrightarrow{r}, t\right)$ of a given component in the amorphous matrix. The other main equation involved is the concentration flux balance at the moving interface

$$\left(c_x - c_R\right) \frac{dR}{dt} = D \left(\frac{\partial c}{\partial r}\right)_{r=R}, \tag{1.8}$$

where $R$ is the crystalline particle radius and $\left(\frac{\partial c}{\partial r}\right)_{r=R}$ the concentration gradient in the untransformed side of the interface. Here, $c_x$ is the concentration inside the crystalline precipitate, and $c_R$ is the equilibrium concentration of the liquid phase at the interface of a particle of radius $R$. The dependence of $c_R$ on the precipitate radius is determined by the capillarity condition

$$c_R = c_l + c_l \Gamma \kappa \tag{1.9}$$

where $\kappa = \frac{\Lambda}{R}$ is the mean curvature in a growing $(\Lambda+1)$-dimensional hypersphere and $\Gamma$ is the capillary length.

Even in the case of an isolated particle growing in an infinite matrix, exact analytical solutions of the equations (1.7) and (1.8) are only known if constant equilibrium concentration at the interface ($c_R = c_l$) is considered, that is neglecting capillarity. The classical work of Zener [43] gives the exact solution for the case of spherical precipitates with boundary conditions

$$\begin{array}{ll} c\left(r = R, t\right) = c_l & 0 < t \leq \infty \\ c\left(r, t = 0\right) = c_0 & 0 < r \leq \infty \\ c\left(r = \infty, t\right) = c_0 & 0 < t \leq \infty \end{array}, \tag{1.10}$$

where $c_0$ is the initial concentration of the matrix. However, even in such a case, the obtained solution is rather too cumbersome to use conveniently, and approximations giving simpler expressions are often used. In another classical reference, Aaron et al. [44] review the different analytical approximations to the diffusion-controlled growth kinetics of single precipitate particles. The result is always a radius time dependence of the kind

$$R = \lambda \left(Dt\right)^{\frac{1}{2}} \tag{1.11}$$

where $\lambda$ is a dimensionless parameter depending on the value of the initial supersaturation

$$\gamma = \frac{c_l - c_0}{c_l - c_x} \tag{1.12}$$

The specific form of $\lambda$ differs in each approximation.

These results do not take into account the destabilization of the interface. Spherical growth of precipitate particles is stable only for small particle sizes. In the case of $\gamma \ll 1$, the spherical shape is strictly stable in a size range going from $R^*$ to $21R^*$, where $R^*$ is the critical nucleation radius above which the sphere grows and below which it shrinks [45]. In such small radius range the capillarity effect is not negligible, thus invalidating the solutions presented above (eq. (1.11)). However, inside a range going from $10R^*$ to $100R^*$, spherical shape is not unduly unstable and diffusion-controlled growth of particles neglecting capillarity is a good approximation. Further growth above this range is governed by side-branching interaction leading to dendritic patterns [46]. Notwithstanding, particle growth as described by eq. (1.11) is used in many works giving good results in the analysis of primary crystallization, as spherical particles showing diffusion-controlled growth are expected in the devitrification of many amorphous metallic alloys [47, 48].

## 1.2 Modelling of primary crystallization

In a system out of the equilibrium the kinetics of the transformation is the key point to predict its temporal evolution and microstructure, that can be crucial to predict the macroscopic properties of the particular material. In this section the different models existing in the literature are presented. First of all, a general model for nucleation and growth transformations, the KJMA model, is described and the limitations of the model for explaining primary crystallizations are presented. Next, two different ways of solving these limitations are derived and compared with experimental results. Finally phase-field model simulations will be also presented, due to the fact that in such simulations the diffusion equation is solved in all the space, thus becoming a useful tool to study primary crystallizations.

### 1.2.1 KJMA model for nucleation and growth transformations

When the precipitate particles reach a certain size, competition between neighboring particles begins to interfere with the growth. In polymorphic transformations this competition is purely geometric, that is particles stop growing because of direct impingement. In this case the overall transformation rate is well-described by the Kolmogorov, Johnson-Mehl and Avrami (KJMA) equation [49, 50, 51]

$$dx\left(t\right) = \left[1 - x\left(t\right)\right] d\widetilde{x}\left(t\right) \tag{1.13}$$

or its integral counterpart

$$x(t) = 1 - \exp\left[-\tilde{x}(t)\right] \tag{1.14}$$

This equation relates the transformed volume fraction at a given time $x(t)$ with its extended counterpart $\tilde{x}(t)$. This extended transformed fraction is defined as the volume fraction occupied by the growing crystallites neglecting impingement, that is

$$\widetilde{x}(t) = \frac{4\pi}{3} \int_0^t I(\tau) R^3(\tau, t)\, d\tau, \tag{1.15}$$

where $I(\tau)$ is the crystallite nucleation rate per volume unit and $R(\tau, t)$ is the radius of a crystallite nucleated at time $\tau$. In isothermal crystallization where the thermodynamic conditions determining the growth and nucleation laws are expected to be constant, it is possible to write the extended fraction as a power of time, that is

$$x(t) = 1 - \exp\left(-kt^n\right), \tag{1.16}$$

where $k$ is known as the reaction constant and $n$ is the so-called Avrami exponent. The value of the Avrami exponent is then directly related to the time-dependence of the growth and nucleation laws [39]. It is also possible to write equation (1.16) in non-isothermal crystallization, but then, the problem is if the obtained Avrami exponents mean something [52].

When analyzing the results obtained from experimental data the Avrami exponent can be split in two parts, $n = n_I + n_G$, related respectively to the nucleation and growth mechanisms. In 3 dimensional growth, $n_I$ is expected to have values varying from 1 (constant nucleation-rate) to 0 (preexisting or quenched-in nuclei) while $n_G$ have typical values of 3 (constant growth-rate) and of 1.5 (parabolic or diffusion-controlled growth). Other more complex nucleation and growth mechanisms lead to values of the Avrami exponent different than the ones just mentioned. One should note here that different combinations of nucleation and growth mechanisms can lead to the same $n$ value, being necessary an adequate theoretical description to interpret the experimental crystallization data [53].

The KJMA model is only valid for a random distribution of particle nuclei, isotropic growth with direct impingement and particle growth-rate not decreasing with time [54, 55]. However, it is used as a good approximation in many transformations not strictly fulfilling these conditions due to its simplicity and robustness. Indeed, some approaches based on the KJMA equation (eq. (1.14)) describe transformations with different kinds of non-random nucleation and anisotropic growth [56, 57, 58, 59].

Two main objections arise when applying the KJMA model to primary crystallization. Firstly, the parabolic growth-law of equation (1.11) provides a growth rate decreasing with time, thus breaking one of the KJMA validity conditions [20]. However, it has been demonstrated that the deviation of equation (1.14) in the prediction of the transformed fraction evolution for such a

case is less than 0.9% [56, 58], so in this work we will consider that the KJMA model gives an adequate description of transformations with parabolic growth laws. Secondly, competition between neighboring particles through the overlap of concentration fields breaks some of the KJMA-model applicability requirements. On one hand, the growth of the particles does not stop because of direct impingement but gradually decreases due to the overlapping of the concentration profiles. The concentration gradients surrounding the particles become progressively flatter, thus reducing the diffusion-controlled growth-rate. This is the so-called soft-impingement (SI) effect. In an analytical approach, Ham [60] found that the Avrami exponent keeps its value of $n = \frac{3}{2}$ (preexisting nuclei and diffusion-controlled growth) in the case of a regular array of spheroidal precipitate particles, but there is not any demonstration of the validity of the KJMA model for SI between not regularly distributed particles. On the other hand, nucleation of new crystallites is easier further away from previously existing ones, as the concentration gradients of the particles make the untransformed phase around the existing crystallites more stable to nucleation. This is the non-random nucleation (NRN) effect [62, 98]. Neither SI nor NRN effects are taken into account in the KJMA model.

Indeed, the KJMA model, which is based on the geometrical interference between particles, can not be applied to transformations with low supersaturation values and so with final crystallized fractions $\gamma \leq 0.1$. In such cases, the behavior of the kinetic parameters throughout the transformation can be well described by introducing a mean-field approach of the compositional change in the matrix [63]. However, in transformations with $\gamma \geq 0.1$ some degree of geometric interference between growing grains is expected and, accordingly, primary crystallization was described classically by means of the KJMA equation [64]. In such cases the volume transformed fractions $x(t)$ and $\widetilde{x}(t)$ are normalized by the final crystallized volume fraction, which corresponds to the initial supersaturation. Hence equation (1.14) is re-written as

$$\xi(t) = 1 - \exp\left[-\widetilde{\xi}(t)\right], \tag{1.17}$$

where $\xi = \gamma^{-1} x(t)$ and $\widetilde{\xi} = \gamma^{-1}\widetilde{x}(t)$ [39]. The Avrami exponent is then calculated as

$$n(t) = \frac{d\ln\left[-\ln\left[1-\xi(t)\right]\right]}{d\ln(t)} = \frac{d\ln\left[\widetilde{\xi}(t)\right]}{d\ln(t)}. \tag{1.18}$$

Equations (1.17) and (1.18) are widely used in studying primary crystallization of amorphous alloys. Frequently, complex behavior and unusual low values of the Avrami exponent are reported [65, 66, 67]. Figure 1.7 shows an experimental determination of $n(\xi(t))$ from ref. [53] where the Avrami exponent varies from $n \simeq 4$ at the initial stages of the transformation to $n < 1$ at the final stages. These low values are usually related to the SI and/or to the NRN [48][56], both effects being expected to become specially important at the final stages of the transformation. However, as stated before, primary crystallization does not fulfill the validity conditions of the KJMA model [54, 55]. Even more,

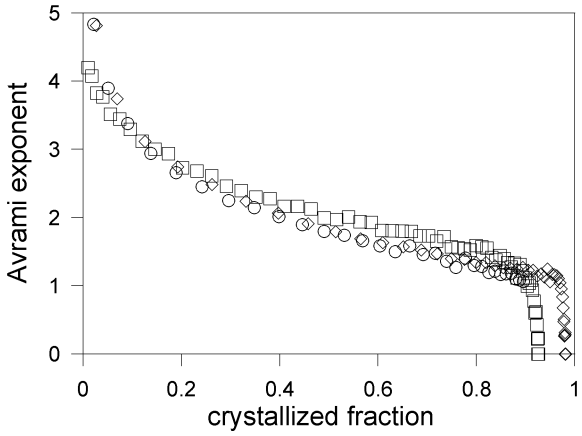


Figure 1.7: Experimentally determined Avrami exponents vs crystallization fraction for a FINEMET metallic glass from [53]. Annealing at 763 K (squares), at 773 K (hexagons) and at 783 K (circles)

the normalization by $\gamma$ of both real and extended transformed volume fractions is not clearly justified.

In the next subsection, different ways of dealing with the limitations of the KJMA model will be presented.

### 1.2.2 Kinetic models

#### Non-random nucleation model

In order to introduce the non-randomness into the KJMA model, different regions around the growing crystallite can be defined, each one with a different value of the nucleation rate [57]. In the simplest case, the authors considered a region of thickness $\delta$ around the existing grains where the nucleation is inhibited. This description affect both, nucleation and growth: on the one hand, a smaller efective nucleation rate is obtained; on the other hand, the effective growth rate of the grains is higher than the nominal growth rate just after nucleation, because a collision with other grain (and thus a reduction in the growth rate) is not possible until the grain reaches at least $\delta/2$.

The effective nucleation rate may be obtained considering the untransformed volume divided into two regions: the boundary volume where the nucleation is not allowed, $x_B(t)$, and the remaining untransformed volume where the nucleation rate is $I_0$. Then, the extended transformed fraction can be written as:

$$\widetilde{x}(t) = \int_0^t I_0 \left(1 - \frac{1 - x(t) - x_B(t)}{1 - x(t)}\right) \frac{4}{3}\pi G_0^3 (t-\tau)^3 d\tau \qquad (1.19)$$

where $G_0$ is the grain growth rate and $\tau$ is the time where the grain was born. In order to evaluate $x_B(t)$, the region that includes the grain plus the boundary zone where the nucleation is inhibited is considered to satisfy the Avrami equation. In a similar way, the computation of the $x(t)$ value is obtained with a modified Avrami equation that takes into account the growth rate changes due to the non-randomness in the nucleation. That is done considering the probability of finding free space for growing, that is different at the first stage of growth ($r \leq \delta/2$) when actual grains can not collide with other grains and at the second stage of growth ($r \geq \delta/2$) when collision of actual grains with other grains nucleated in regions accessible during growth is possible. The Avrami equation can be written, then, as:

$$\frac{dx}{d\tilde{x}} = [1 - x(t)]\,[1 + f(r)x(t)] \tag{1.20}$$

with:

$$f(r) = \begin{cases} 1 & r < \delta/2 \\ \frac{1}{2}\left(\frac{\delta}{r}\right)^3 - \frac{3}{16}\left(\frac{\delta}{r}\right)^4 & r > \delta/2 \end{cases} \tag{1.21}$$

As is expected, equation (1.20) reproduces the Avrami equation in the case $\delta = 0$, i.e., when nucleation is allowed in all the space.

In the more general case in which the nucleation is not fully suppressed in the region of thicknes $\delta$, but reduced by a factor $\alpha < 1$, it is also possible to write a modified Avrami equation:

$$\frac{dx}{d\tilde{x}} = [1 - x(t)]\,[1 + f(r)x(t)]^{1-\alpha} \tag{1.22}$$

that also reduces to equation (1.20) in the proper limit.

This model allows to use the Avrami formalism in transformations with non-random nucleation, but also shows that the deviations from the original Avrami equations are small, even for large non-randomness. However, this model is not able to explain the non-constant Avrami exponents with extremely low final values found for the crystallyzation of amorphous materials.

### A mean-field model

Another way for dealing with the stabilization of the untransformed matrix in primary crystallizations is the reduction of the kinetic parameters by means of a mean-field approach [48]. In order to account for the increase (or decrease) of the average concentration in the amorphous matrix as the transformation proceeds, a mean-field approach is adopted by calculating the average concentration in the untransformed matrix at time $t$, $c\,(t)$. By means of a global mass balance

$$x\,(t)\,c_x + [1 - x\,(t)]\,c\,(t) = c_0 \tag{1.23}$$

the variation of the mean supersaturation of the untransformed matrix can be written as

$$\frac{c_l - c\,(t)}{c_l - c_x} = \gamma \frac{1 - \gamma^{-1} x\,(t)}{1 - x\,(t)} \tag{1.24}$$

where $\gamma$ is the initial supersaturation given in equation (1.12). The factor $\varphi(t) = \frac{1-\gamma^{-1}x(t)}{1-x(t)}$, varying from $1 \to 0$ as $x(t)$ varies from $0 \to \gamma$, indicates the average stabilization of the matrix and is called the soft-impingement factor.

Considering that the driving force of the transformation is proportional to the supersaturation of the matrix, when the mean supersaturation decreases so does the driving force. Then, the kinetics of the primary crystallization can be modelled by introducing a decreasing driving force into the computation of the kinetic parameters, that is

$$I(\gamma, t) \to I(\gamma\varphi(t), t) \tag{1.25}$$

and

$$G(\gamma, \tau, t) \to G(\gamma\varphi(t), \tau, t). \tag{1.26}$$

It is worth to say here that different nucleation and growth models with empirically adjusted parameters are able to describe the kinetics of this kind of transformations. In fact, the approach described by the previous equations has been made by different authors, assuming diverse dependences of the kinetic parameters on $c(t)$ [69]. However, all these models have in common that the kinetic parameters become null at the end of the transformation, that is $I \to 0$ and $G \to 0$ when $\gamma\varphi(t) \to 0$, as it is physically expected.

After taking into account the diminishing driving force in the kinetic parameters expressions, the geometrical impingement is modelled by means of the Avrami equation. Therefore, in this approach, the crystallized fraction given by the Avrami equation (1.14) reaches a final value of $\gamma$ not because of the exhaustion of the untransformed volume but because of the vanishing of the kinetic parameters used for the calculation of the extended fraction, that is $\frac{d\tilde{x}(t)}{dt} \to 0$ as $x(t) \to \gamma$.

Summarizing, this model accounts for the SI and NRN effects described above by considering the stabilization of the matrix a global process, while maintaining the applicability of the KJMA equation in order to deal with the geometric impingement. This is a first order approach and, although the mean reduction of the kinetic parameters has a physical sense, the applicability of the KJMA equation under these premises is of uncertain validity. On one hand, SI prevents direct impingement between the growing crystallites, against one of the main hypothesis of the KJMA theory. On the other hand, NRN is opposite to the random nucleation required by KJMA.

### 1.2.3 Phase-field models

The evolution of microstructures is a feature that appears not only in phase transformations but in many fields including biology [70] or hydrodynamics [71], and as stated in 1.1 the structural features in a microstructure play a critical role in determining the physical macroscopic properties of a given material. But due to the complexity and the possible nonlinearity of microstructure evolution, and the length scales involved, theoretical models are not satisfactory. A well known

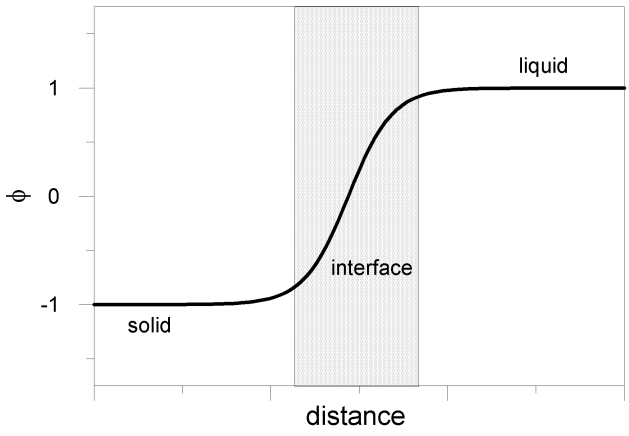


Figure 1.8: Schematic representation of the smooth change in the phase-field variable across a solid-liquid interphase.

example in solidification processes is the formation of complex structures like dendritic sidebranching. In these kinds of problems is crucial to determine the interface position between the liquid and the solid phase at any instant of time. In a sharp interface model, a interface without width is considered and the time evolution of the system is governed by macroscopic equations, like the diffusion equation, with the corresponding boundary conditions at the interface, or the Gibbs-Thomson equation. Moreover, certain magnitudes must be conserved at the interface, like the latent heat of the transformation in a solidification process. So, the interface dynamics is linked to the bulk dynamics and hence the problem is mathematically complex to deal with due to the integro-differential equation that must be solved, and numerical methods are often used.

In this context *phase-field models* (PFM) or *diffuse interface models* appeared as an alternative to the study of solidification problems and in general for modeling many types of microstructural evolution processes. It is based on a diffuse-interface description developed by van der Walls [72] and more recently and independently by Cahn and Hilliard [73]. The introduction of a non-conserved scalar order parameter or phase field $\phi$ allows to transform a moving interface into a set of coupled partial differential equations. The phase field is continuous in the space and takes constant values in each phase, in this way the interface is the region of thickness $\epsilon$ in which that field changes smoothly (figure 1.8). The coupling between the phase field and the corresponding conserved quantity (heat or concentration) is through adding a source term in the diffusion equation to include the boundary conditions at the interface. The microstructure temporal evolution is described by two well-known equations: the Cahn-Hilliard equation for the conserved quantity [74] and the Allen-Cahn (a time dependent Ginzburg-Landau equation) for the non-conserved parameter

$\phi$ [75]. Integrating the equations the system is considered as a whole without distinction between the interface and the bulk. In this way the location of the interface does not have to be explicitly determined because is given by those points where the phase field varies in a certain range, as for example $0.4 < \phi < 0.6$.

In the derivation of a PFM, the value of the interface thickness $\epsilon$ is a key point because the original sharp interface model must be recovered in the limit $\epsilon \to 0$. This asymptotic behaviour of the PFM allows to relate the parameters that enter in the PFM equations with physical magnitudes of relevance in the macroscopic problem. At the same time, in order to obtain meaningful results $\epsilon$ must be much lower than the shortest characteristic length of the original problem, $l_c$, introducing a limitation in the simulations because, as will be shown, decreasing the interface width implies the diminution of the time step needed in the numerical treatment of the equations, hence increasing the computing time.

One of the major drawbacks that has been argued against PFM is the lack of physical meaning of the phase field $\phi$. But diffuse interface models are a variation of the *model C* [76] presented in the framework of the theory of dynamical critical phenomena. This model can be applied to a variety of physical systems like structural phase transitions, magnetic phase transitions or order-disorder transitions in alloys. In this context PFM can be derived from a free energy functional, but it is worth to note that this is not a necessary condition as far as the PFM is able to reproduce the sharp interface model in the limit $\epsilon \to 0$.

In a PFM with one conserved ($c$) and one non-conserved ($\phi$) quantity and a given total free energy $F$, the Cahn-Hilliard and Allen-Cahn equations can be written as [77]:

$$\frac{\partial c}{\partial t} = \nabla M \nabla \frac{\partial F}{\partial c} \tag{1.27}$$

$$\frac{\partial \phi}{\partial t} = -L \frac{\partial F}{\partial \phi} \tag{1.28}$$

where $M$ and $L$ are related to atom and interface mobility, respectively. Hence, to define the particular PFM one must give an expression for the free energy, that can be derived from thermodynamic arguments or constructed *ad-hoc*. In general, $F$ can be written in two terms, one for the bulk contribution and one for the interface contribution:

$$F = \int \left[ f(c,\phi) + \alpha \left(\nabla c\right)^2 \right] d^3r \tag{1.29}$$

The first term of the integral represents the local free energy density from short-range chemical interactions while the gradient term accounts for the interfacial energy (it is a nonzero term only in the interface). In a more general case, two extra terms can be added to the total free energy: *a)* a gradient term in the integral for the non-conserved phase and, *b)* a second volume integral representing the contributions from long-range interactions like elastic or electrostatic interactions [77]. The most distinctive component of a given PFM is the local free energy density function $f(c,\phi)$ that usually have a double-well form and

depends only on the phase-field variable:

$$f(\phi) = 4\Delta f \left( -\frac{1}{2}\phi^2 + \frac{1}{4}\phi^4 \right) \tag{1.30}$$

or

$$f(\phi) = 4\Delta f \phi^2 (1-\phi)^2 \tag{1.31}$$

depending on the location of the two minima of the free energy. In the first equation they are located at $\phi = -1$ and $\phi = +1$, whereas in the second they are located at 0 and 1. $\Delta f$ is the potential difference between the two minima and for some transformations can represent its driving force. These two functions (1.30)-(1.31) are particularly useful in the modelling of solidification processes, where one of the minima represents the liquid state and the other one the solid state. In many applications of the PFM to real materials it is necessary to use more complex local free energy densities, to introduce more than one field variable or to couple in its dependence the field variable with the conserved quantity.

Existing phase-field applications have been mainly focused on solidification processes, solid-state phase transformations and grain growth and coarsening, but recently they have been applied to thin films and surfaces, dislocation dynamics, crack propagation or electromigration. For an excellent review see [77].

As PFM solve the diffusion equation in all the space and also take into account the proper boundary conditions for the particular problem studied, they are a useful tool to study the soft-impingement effect that appear in primary crystallizations. Moreover, PFM also allow to study the effects on the kinetics of any nucleation protocol introducing it *ad-hoc* in the implementation of the model or added as a noise term to the governing equations [78]. The present thesis will not focus on the microstructural evolution in primary crystallization but in the kinetics. In this way, PFM will be used to check the validity of the existing kinetics models (introduced in 1.2.2), i.e., to determine if the kinetic in a primary crystallization is only affected by the SI and NRN effects or there are changes in other physical properties that must be taken into account in the modelling of this kind of phase transformations.

A first step in this direction can be found in [79] where a two-dimensional PFM is used to test the KJMA model comparing the transformed fraction obtained with the two methods. In that work, the PFM only have a non-conserved quantity and the agreement between the simulated and the KJMA kinetics is very good. That is because there is no coupling between the phase-field variable and the concentration, and hence the growing particles impinges directly with their interfaces instead of through the concentration profiles, thus verifying one of the hypothesis of the KJMA model. In a more realistic simulation, the concentration field must be included in the PFM, and this is what is done in chapter 2. Nevertheless, the work by Jou and Lusk [79] is useful because it demonstrate the capability of PFM for predicting the kinetics of phase transformations and not only to describe the microstructure.

## 1.3 Diffusion in liquids and amorphous solids

The atomic structure of an amorphous alloy determines in a great extent its properties, and it is very sensitive to heat treatments. Therefore, processes like structural relaxation, phase separation or crystallization that involve significant rearrangements of the constituent atoms cause changes in the amorphous alloy properties. In general, these processes are controlled by diffusion of atoms through the structure of the amorphous alloys and, hence, the understanding of atomic diffusion in these materials is a key point in order to control the macroscopic properties useful from a technological point of view. As an example, in section 1.1.2 the importance of diffusion in primary crystallizations was stated. In this section different diffusion mechanisms will be presented and the effects of temperature, pressure or composition in the diffusion coefficient will be studied. Finally, a discussion about which is the diffusion mechanism in amorphous alloys and the differences with the mechanism in the corresponding supercooled liquid will be presented.

### 1.3.1 Mechanisms of diffusion

The fundamental property of a diffusion process is the diffusion coefficient $D$ defined through the Fick's law as the constant of proportionality between the flux of diffusing atoms ($\overrightarrow{J}$) and the concentration gradient of diffusing atoms ($\overrightarrow{\bigtriangledown} c$):

$$\overrightarrow{J} = -D\overrightarrow{\bigtriangledown} c \tag{1.32}$$

Applying the law of conservation of mass to every volume element with a concentration field $c$, the time evolution of that field (the diffusion equation) is obtained:

$$\frac{dc}{dt} = \overrightarrow{\bigtriangledown}(D\overrightarrow{\bigtriangledown} c) \tag{1.33}$$

when $D$ is constant over the concentration field, equation (1.7) is recovered.

Before talking about diffusion in amorphous alloys, it is important to know the mechanisms which give rise to diffusion in crystalline solids. Mainly, an atom can diffuse by an interstitial or a vacancy method. In the first case the diffusing atom passes from one interstitial site to one of its nearest-neighbor interstitial sites without permanently displacing any of the matrix atoms, thus the local distortion of the lattice that must occur before the jump constitutes the barrier that must be overcomed. If the interstitial atom is relatively large it will produce a large distortion if it diffuses interstitially, hence there is another mechanism called interstitialcy in which the diffusing atom pushes one of its nearest-neighbor atoms into an interstitial position and occupies the lattice site previously occupied by the displaced atom [80]. In the second case, one of the atoms adjacent to a vacancy jump into it and the diffusion rate will be determined by the fraction of vacant sites available. In any case it can be distinguished between impurity diffusion, when the diffusing species are not a component of the matrix, and self-diffusion when the diffusing species is also a

component of the matrix. Vacancy migration is the most common mechanism of both self-diffusion and impurity diffusion in crystalline metals and alloys [39]. In crystalline alloys the diffusion equation can be expressed by an Arrhenius equation:

$$D = D_0 exp(-H/k_B T) \tag{1.34}$$

where $H$ is the activation enthalpy for diffusion, $k_B$ is the Boltzmann constant and $T$ is the temperature. Then, a possible change in the diffusion mechanism over a range of temperatures can be studied with the help of an Arrhenius plot ($\ln D$ vs. $1/T$). Moreover, there is a correlation between the preexponential factor $D_0$ and the activation enthalpy, valid for self and impurity diffusion in crystalline alloys involving both substitutional and interstitial solid solutions [81]:

$$D_0 = A \exp(H/B) \tag{1.35}$$

where $A$ and $B$ are constants.

In materials that undergo a primary crystallization, the diffusion coefficient can be modified as the transformation proceed due to the evolution of the concentration gradients that appear surrounding the growing nucleus. This variation in the diffusion coefficient can be considered as a local change (as it will be considered in chapter 4) or as a mean-field change through the introduction of the so-called thermodynamic factor that multiply the diffusion coefficient and the rest of the kinetic paramaters [48].

The diffusion mechanism in crystalline solids is also affected by the size of the solute, directly through the elastic strains that it exerts on the surrounding matrix due to the size misfit and indirectly through the electronic interaction. In the first case, bigger atoms mean an increase of the elastic work needed to push the atom through the matrix and thus, an increase of the enthalpy of diffusion and a corresponding decrease in the diffusion coefficient. In the second case, the diffusivity will depend on the valence of the solvent and the solute, therefore an universal correlation between size and activation enthalpy can not be formulated. But in general an increasing activation enthalpy with increasing size can be taken as a sign that the dominant interaction between solute and solvent is elastic (typical of an interstitial or interstitialcy diffusion mechanism), while a decreasing activation enthalpy with increasing size can be taken as a sign that the dominant interaction is electronic (typical of a vacancy mechanism [28]).

Another way of getting information about the diffusion mechanisms is through the pressure dependence of the diffusion coefficient at constant temperature, that can be expressed in terms of an activation volume. The main contribution to the activation volume is from the formation volume of vacancies, and hence, for direct interstitial diffusion, which does not involve any formation volume, no significant pressure dependence has been observed [82].

### 1.3.2 Diffusion in metallic glasses

Diffusion studies in metallic glasses have used the same concepts than in crystalline solids, and the kinks observed in Arrhenius plots have been interpreted as a change in the diffusion mechanisms at the glass transition: from single atom jumps to viscous flow. By contrast, recent experimental evidence (reviewed in reference [28]) indicates that in glasses the diffusion mechanism is a highly collective hopping process that also controls the diffusion in the corresponding supercooled liquid.

In metallic glasses of different compositions, a reduction in the diffusivity after an annealing has been observed, as long as the annealing does not induce the crystallization. This reduction, that can be as high as an order of magnitude, is due to the structural relaxation that suffer these materials. Thus, the diffusion coefficient not only depends on the particular material but also on the thermal history and how the glass has been produced. Isotope effect experiments suggest that in relaxed glasses diffusion involve the simultaneous movement of several atoms while in as-quenched glasses there are only single atom jumps similar to the vacancy-mediated diffusion mechanism in crystalline solids [83]. Moreover, in metallic glasses the relationship between the preexponential factor $D_0$ and the activation enthalpy (eq. (1.35)) still holds but with values of $A$ and $B$ very different for amorphous and corresponding crystalline systems, another indication that the mechanism of diffusion in amorphous alloys can not be only explained with single atom jumps.

In order to explain the motion of atoms in metallic glasses an extension of the free-volume model is used [84]. According to this approach, the diffusivity and the viscosity in amorphous alloys are mediated by defects which result from free-volume fluctuations and that are frozen in the process of cooling the alloy through the glass transition. In particular, the Arrhenius expression for the diffusion coefficient (eq. (1.34)) is modified to take into account the diffusion-defect concentration $c_d$:

$$D = D_0^{'} c_d exp\,(-H/k_B T)$$

with:

$$c_d \propto exp\,(-B_0/2(T - T_0))$$

where $B_0$ is the same constant that relates the viscosity $\eta$ with the temperature (the VTF equation (1.1)), and $D_0^{'}$ represents a preexponential factor. Moreover, it was shown that the Stokes-Einstein relation between diffusion coefficient and viscosity $D\eta/k_B T = const.$ is not valid in amorphous alloys, no matter if they are relaxed or not, and in the supercooled liquid state, thus indicating that hydrodynamic flow does not control the atomic transport mechanisms in these materials. This point will be explained in more detail in the last chapter of this thesis.

This change of mechanism is also supported by predictions of the mode-coupling theory [85] that is considered the most advanced theory of the glass transition at present. In this theory the neighboring atoms of a given atom

freezes in at a critical temperature $T_c$ (that is well above the glass transition temperature) due to the increase in density. Due to this effect, liquidlike viscous flow can not take place below $T_c$ and atomic transport proceeds exclusively via local collective processes.

Summarizing, diffusion in the glassy state as well as in the supercooled liquid state below $T_c$ takes place by highly collective hopping processes and while the diffusivity drops about an order of magnitude near $T_g$, there are no changes in the mechanism of diffusion.

## 1.4 Aim of the thesis

The aim of the present work is to study the kinetic of a primary crystallization in order to elucidate which are the processes that really affect the transformed fraction evolution in this kind of phase transformations. In order to approach this problem from a different point of view, the phase-field model simulations are used to validate or discard the theoretical models presented in 1.2. Is for that reason that in chapter 2 the particular phase-field model used is derived and several checks about its validity are performed. In chapter 3, results from simulations with a constant diffusion coefficient are used to discover that something else beside the soft-impingement and non-random nucleation must be taken into account in order to predict the kinetic of a primary crystallization. Thus, considering the analysis presented in section 1.3 it is reasonable to think that some changes in the transport mechanism must occur along a primary crystallization, changes that we translate into a concentration dependence of the diffusion coefficient justified in chapter 4. Phase-field simulations with this new dependence are performed and compared with the kinetic of an actual primary crystallization. Finally in chapter 5 the conclusions of this thesis are presented and further work proposed.

# Chapter 2

# Phase-field modelling of primary crystallization

This chapter is structured in three parts. First of all, the particular phase-field model used in this work will be presented followed by a discussion about the use of this model instead of more sophisticated ones that are able to treat a wide variety of phenomena. Secondly, the numerical methods used to solve the coupled partial differential equations of the model will be shown and the values of the several parameters that enter into the equations will be justified. Moreover, the numerical characteristics of the simulations of this work will be discussed. Finally, to check the validity of the model, the results of simulations will be compared with several analytical predictions.

## 2.1 Phase-field model for primary crystallization

### 2.1.1 Derivation of the model

In this section we will summarize the derivation of the particular PFM used throughout this work. It is originally developed to study the crystallization of a pure substance from its melt [86] and it has been also used in the study of dendritic growth either controlled by heat diffusion [87] or by diffusion of solute [78].

That model is based on an entropy functional and it guarantees a local positive entropy production, so it is thermodynamically consistent and it is not only a phenomenological approach. Moreover, it allows a particular choice of the phase-field functions that could lead to several specific physical models. The main assumptions of the model are: *a)* to consider a solid-liquid first order phase transition of a pure substance in a closed volume, *b)* the system is in mechanical equilibrium, so the density is uniform and there is no convection in the liquid, *c)* the values for the phase-field variable $\phi$ are set to 0 for the solid and to 1 for

the liquid and *d)* the assumed functional for the entropy is:

$$S = \int_V \left[ s(e,\phi) - \frac{\epsilon^2}{2} \left( \overrightarrow{\bigtriangledown} \phi \right)^2 \right] dv \tag{2.1}$$

where $e$ is the internal energy density, $s(e,\phi)$ is the entropy density and $\epsilon$ is a constant.

Applying the first and second laws of thermodynamics, the time evolution of the internal energy and the phase-field can be found:

$$\frac{\partial e}{\partial t} = \overrightarrow{\bigtriangledown} \left[ c_p D \overrightarrow{\bigtriangledown} T \right] \tag{2.2}$$

$$\tau \frac{\partial \phi}{\partial t} = -\frac{1}{T} \left( \frac{\partial e}{\partial \phi} \right)_s + \epsilon^2 \bigtriangledown^2 \phi \tag{2.3}$$

where $T$ is the temperature, $c_p$ is a constant specific heat, $\tau$ is a positive constant and $D$ is the thermal diffusivity of the liquid. At this point is useful to work with the Helmoltz free energy density $f = e - Ts$. From its differential form and considering that $e$ is a function of $s$ and $\phi$, the following relationships can be obtained:

$$\left( \frac{\partial e}{\partial \phi} \right)_s = \left( \frac{\partial f}{\partial \phi} \right)_T \tag{2.4}$$

$$\left( \frac{\partial \left[ f/T \right]}{\partial T} \right)_\phi = -\frac{e}{T^2} \tag{2.5}$$

The integration of the latter equation at constant $\phi$ yields:

$$f(T,\phi) = T \left[ -\int_{T_m}^{T} \frac{e(\zeta,\phi)}{\zeta^2} d\zeta + G(\phi) \right] \tag{2.6}$$

where $G(\phi)$ is an undetermined function of $\phi$ and $T_m$ is the melting point. To proceed further, the internal energy density is assumed to have the following form:

$$e = e_L(T) + [p(\phi) - 1] L(T) \tag{2.7}$$

with $L(T) = e_L(T) - e_S(T)$ where $e_S(T)$ and $e_L(T)$ are the internal energy densities of the solid and the liquid phase, respectively and $p(\phi)$ satisfies $p(0) = 0$ and $p(1) = 1$; we note that $L(T_m) \equiv L_0$ is the latent heat of fusion. It is the particular choice of this function $p(\phi)$ that will lead to a specific PFM. Thermodynamic considerations requires $f$ to have, for all values of $T$, local minima with respect to $\phi$ at 0 and 1, and accordingly a symmetric double well potential with minima at 0 and 1 has been chosen:

$$G(\phi) = \frac{1}{4a} \phi^2 (1 - \phi)^2 \tag{2.8}$$

where $a$ is a positive constant related to the energy difference between the two local minima (figure 2.1). With the assumed internal energy density (equation

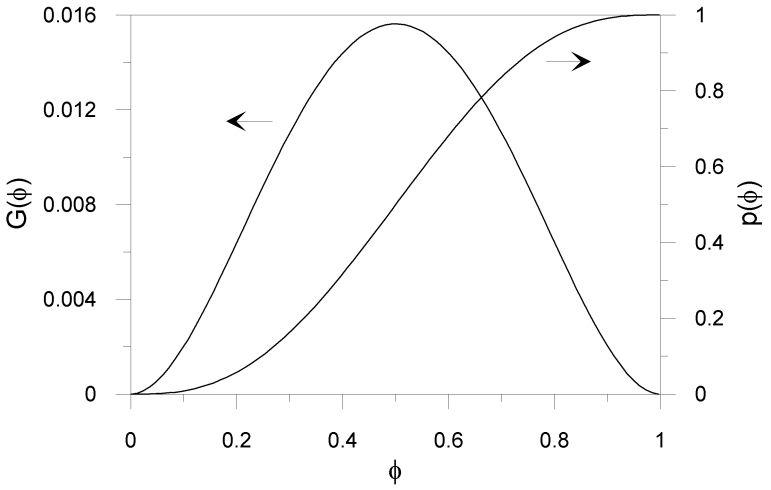


Figure 2.1: Functions $G(\phi)$ and $p(\phi)$ that define the employed PFM

(2.7)), equation (2.6) and the relationship (2.4), the governing equations (2.2) and (2.3) can be written as:

$$\left\{\frac{\partial e_L}{\partial T} + (p(\phi) - 1)\frac{\partial L}{\partial T}\right\}\frac{\partial T}{\partial t} + L(T)\frac{\partial p(\phi)}{\partial \phi}\frac{\partial \phi}{\partial t} = \overrightarrow{\bigtriangledown}\left[c_p D \overrightarrow{\bigtriangledown} T\right] \tag{2.9}$$

$$\tau\frac{\partial \phi}{\partial t} = Q(T)\frac{\partial p(\phi)}{\partial \phi} - \frac{\partial G(\phi)}{\partial \phi} + \epsilon^2 \bigtriangledown^2 \phi \tag{2.10}$$

$Q(T)$ being:

$$Q(T) = \int_{T_m}^{T} \frac{L(z)}{z^2} dz \tag{2.11}$$

In order to complete the PFM model, the functions $e_L(T)$ and $p(\phi)$ must be specified. We assume the energy density in the liquid to be a linear function of temperature:

$$e_L(T) = e_L(T_m) + c_p(T - T_m) \tag{2.12}$$

and following [78] we choose (figure 2.1 right):

$$p(\phi) = \phi^3\left(10 - 15\phi + 6\phi^2\right) \tag{2.13}$$

With this choice of $p(\phi)$, the function $Q(T)$ has no restrictions, and then, for simplicity we can choose its value so that $L(T) = L_0$ [86].

At this point is it possible to relate the parameters $a$ and $\epsilon$ with the interface thickness $\delta$ and the surface free energy $\sigma$. To do that, the one-dimensional solution of equation (2.10) under equilibrium conditions ($T = T_m$) will be considered. It will be assumed that the interface is locate at $x = 0$, that the solid

phase is in the region $-\infty < x < 0$ and the liquid phase is in $0 < x < +\infty$. Hence, the equation to solve is:

$$\epsilon^2 \frac{d^2\phi}{dx^2} - \frac{dG(\phi)}{d\phi} = 0 \tag{2.14}$$

with boundary conditions $\phi(-\infty) = 0$ and $\phi(\infty) = 1$. A solution of this equation is

$$\phi(x) = \frac{1}{2}\left[\tanh\left(\frac{x}{2\sqrt{2a}\epsilon}\right) + 1\right] \tag{2.15}$$

from where it is clear that the interface has a characteristic thickness that depends on $a$ and $\epsilon$:

$$\delta = \sqrt{a}\epsilon \tag{2.16}$$

The surface free energy associated with the one-dimensional solution can be calculated using the Helmholtz free energy at $T_m$ that can be written as:

$$\mathcal{F} = \int_V \left[f(T_m, \phi) + \frac{\epsilon^2 T_m}{2}\left(\frac{d\phi}{dx}\right)^2\right] dv \tag{2.17}$$

Then, the surface free energy will be the difference between the total free energy and the energy associated to the bulk phases:

$$\begin{aligned} \sigma = \textstyle\int_{-\infty}^{\infty} \left[f(T_m, \phi) + \frac{\epsilon^2 T_m}{2}\left(\frac{d\phi}{dx}\right)^2\right] dx - \\ - \textstyle\int_{-\infty}^{0} \left[f(T_m, 0)\right] dx - \int_{0}^{\infty} \left[f(T_m, 1)\right] dx \end{aligned} \tag{2.18}$$

that recalling $f(T_m, 0) = f(T_m, 1) = 0$ becomes:

$$\sigma = \int_{-\infty}^{\infty} \left[f(T_m, \phi) + \frac{\epsilon^2 T_m}{2}\left(\frac{d\phi}{dx}\right)^2\right] dx \tag{2.19}$$

Finally, using equations (2.14) and (2.15), the surface free energy can be evaluated to yield:

$$\sigma = \frac{\sqrt{2}\delta T_m}{12a} \tag{2.20}$$

that again depends on $a$ and $\epsilon$.

It is useful to write the governing equations in a dimensionless form, hence we introduce a characteristic length $w$ and a dimensionless temperature $u$ ($u = \frac{T - T_m}{\triangle T}$, with $\triangle T$ being the undercooling). The dimensionless space and time are:

$$\tilde{x} = \frac{x}{w} \quad \text{and} \quad \tilde{t} = \frac{t}{w^2/D} \tag{2.21}$$

and the time evolution equations for the phase-field and the dimensionless temperature become, from equations (2.9) and (2.10) and assuming a constant diffusion coefficient :

$$\frac{\varepsilon^2}{m}\frac{\partial\phi}{\partial\tilde{t}} = \phi(1-\phi)[\phi - \frac{1}{2} + 30\varepsilon\alpha Su\phi(1-\phi)] + \varepsilon^2 \tilde{\bigtriangledown}^2 \phi \tag{2.22}$$

$$\frac{\partial u}{\partial \tilde{t}} + \frac{1}{S}(30\phi^2 - 60\phi^3 + 30\phi^4)\frac{\partial \phi}{\partial \tilde{t}} = \tilde{\bigtriangledown}^2 \tilde{u} \tag{2.23}$$

Here, a tilde denotes the dimensionless equivalent of a dimensional quantitaty or a derivative with respect a dimensionless quantity. The dimensionless interface thickness has been defined as $\varepsilon = \frac{\delta}{w}$. The rest of the parameters that appears in the latter equations as a consequence of writting the equations in a dimensionless form are:

$$S = \frac{c_p \bigtriangleup T}{L_0} \tag{2.24}$$

$$\alpha = \frac{\sqrt{2} w L_0^2}{12 c_p \sigma T_m} \tag{2.25}$$

$$m = \frac{6\sqrt{2}\delta\sigma}{\tau D T_m} \tag{2.26}$$

With these relations, it can be seen that $S$ is the dimensionless undercooling. A capillary length can be defined as [88]:

$$d_0 = \frac{c_p T_m \sigma}{L_0^2} \tag{2.27}$$

thus, $\alpha\varepsilon = \frac{\sqrt{2}\delta}{12 d_0}$. Therefore, $\alpha\varepsilon$ is proportional to the ratio between the interfacial width and the capillary length. Finally, $m$ can be related to the interface kinetic coefficient $\mu$ performing an asymptotic analysis of equation (2.22) in the limit $\varepsilon \to 0$:

$$m = \frac{\mu \sigma T_m}{D L_0} \tag{2.28}$$

Hence, comparing equations (2.26) and (2.28), it can be seen that the positive constant $\tau$ is proportional to the inverse of the interface kinetic coefficient, so it is a measure of the rate at which atoms will attach themselves to the interface.

The PFM used throughout this work is then characterized by the equations (2.22) and (2.23) and by the parameters $S$, $\varepsilon$, $\alpha$ and $m$ that can be related to physical parameters.

### 2.1.2 Application to primary crystallization

In order to apply this model to a transformation that takes place isothermally and then the growth of the new phase is controlled by the diffusion of concentration fields instead of a temperature field, the equations (2.24) - (2.28) must be written in terms of concentrations. In the case of study, the growth of the crystalline phase takes place inside an amorphous solid matrix, so the values for the phase-field variable will be:

$$\begin{cases} \phi = 0 & \text{for the crystalline phase} \\ \phi = 1 & \text{for the amorphous phase} \end{cases} \tag{2.29}$$

with the supersaturated amorphous matrix playing the role of the undercooled liquid. Comparing the diffusion equation in the case of heat diffusion and solute

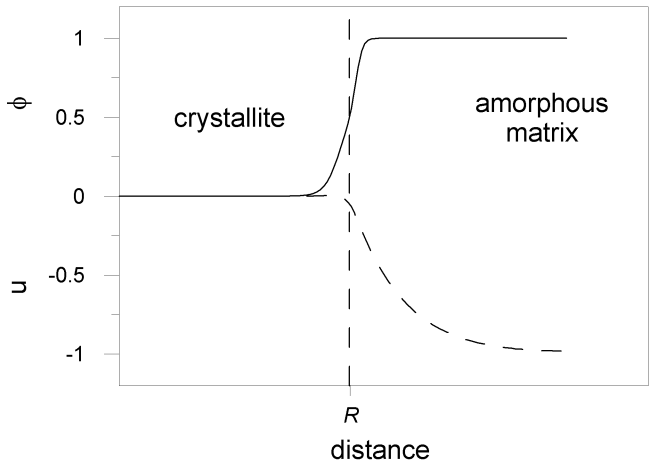


Figure 2.2: Profiles considered for the dimensionless concentration (dashed line) and the phase-field variable (solid line)

diffusion and the requirement of energy and solute conservation in the interface, we can relate $c$, $L_0$ and $T_m$ with $c_0$, $c_l$ and $c_{xt}$ that are, as explained before, the initial concentration of the matrix, the equilibrium concentration of the matrix at the interface and the concentration inside the crystalline precipitate respectively (see figure 1.1 in chapter 1):

$$c_p = 1, \qquad L_0 = c_l - c_{xt}, \qquad T_m = c_l \tag{2.30}$$

and then, the dimensionless concentration and the supersaturation of the matrix can be written as:

$$u = \frac{c - c_l}{c_l - c_0} \tag{2.31}$$

$$S = \frac{c_l - c_0}{c_l - c_{xt}} \tag{2.32}$$

The driving force of the transformation is the supersaturation $S$ and as the values of $c_0$ are comprised between $c_{xt}$ and $c_l$, we can set without loss of generality the values of $c_{xt}$ and $c_l$ as 0 and 1 respectively. With that choice $S \in [0, 1]$ and $u \in [-1, 0]$, i.e. :

$$\begin{cases} u = 0 & \text{for the crystalline phase} \\ u = -1 & \text{for the amorphous phase} \end{cases} \tag{2.33}$$

The simulated concentration and phase-field profiles are shown in figure 2.2. As can be seen, in the simulations the crystallite has the same concentration as the equilibrium concentration of the matrix at the interface. This will have consequences in the way the mass balance is calculated (see section 2.3.3). Now,

we can write the $m$ parameter that appear in the time evolution equation of the phase-field as:

$$m = \frac{\mu\sigma}{D} \tag{2.34}$$

that with (2.25), (2.32) and $\varepsilon$ constitute the parameters that define the employed PFM applied to primary crystallization. The particular values of these parameters are discussed in section 2.2.

### 2.1.3 Discussion

As stated before, the PFM used in this work has been successfully used in the study of sidebranching in solutal dendritic growth and also in anisotropic heat diffusion phenomena like needle crystal growth [89]. In recent years much effort has been devoted to the PFM in order to develop models able to predict the experimental results obtained in processes that lead to microstructure formation [90]. Mainly, there are two problems to achieve a quantitative phase field modelling:

1. Resolution of the interface thickness: the interface region extends over few nanometers, which is usually some orders of magnitude smaller than the studied object, so the resolution required in the numeric solving of the phase-field equations is too high to be carried out in standard desktop computers. Thus, interface widths broader than physical ones are usually used and then, care must be taken to ensure that the phase-field calculations deliver the proper interface dynamics. Work has been done to compensate the unphysical effects of thick interfaces introducing new terms in the phase-field equations, thus obtaining more complex models [93]. As we are not trying to compare quantitatively the simulations with experimental results, but trying to understand the physical processes that govern primary crystallizations, we do not need to use complex models and the interface width will be a model parameter.

2. Application of the theory under strong anisotropies of the interface free energy: except multi-phase field models [91, 92], there are no models able to describe anisotropic growth of crystals with different crystallographic orientations, and then most of the new models are attempts to deal with this case because its practical importance in polycrystalline materials. In primary crystallization the growth of the new particles is isotropic and in each grain there is only one crystallographic orientation, thus for our purposes is better to work with a PFM that not introduce an extra non-conserved field (the orientation) because it will be time consuming in the numerical resolution of the phase-field equations.

In chapter 1, section 1.1.2, it was explained that the classical nucleation theory employs a sharp interface separating the two phases which have bulk properties. One of the problems that arise in the study of the nucleation phenomena is that the fluctuations from which the nuclei are formed contain typically from ten to

several hundred molecules, and that is the order of magnitude of the interface width, indicating that these fluctuations are essentially comprised of interface [90]. Therefore, to assume a sharp interface is not appropriate to study nucleation [95]. As PFM use diffuse interfaces they are more adequate to describe crystal nucleation than those based on a sharp interface and hence, there are new PFM able to study this phenomena. These models can be used to simulate the nucleation process and also to calculate the height of the nucleation barrier [90]. In the first case uncorrelated Langevin-noise terms are introduced in the governing equations with amplitudes determined by the fluctuation-dissipation theorem. This kind of nucleation modelling is often prohibitively time consuming. One solution is to increase the amplitude of the noise but this will lead to a fluctuations greater than the real ones. The other solution, and the one adopted in this thesis, is to initiate the nucleation randomly placing nuclei with size slightly greater than the critical size (details can be found in section 3.3), thus avoiding the introduction of extra terms in the equations.

Finally, a new phase-field approach has been constructed to study the dynamics of crystal growth including elastic and plastic deformations [96]. This model, called *phase field crystal* is different from other PFM in that the phase-field variable is periodic with the same periodic crystal symmetry as a given crystalline lattice in the case of the solid state and is uniform in the case of the liquid state. This approximation is extremely useful to study the properties of crystals controlled by elasticity and symmetry. Although this model can also describe nucleation and growth processes, elastic properties are not needed to be taken into account in order to describe primary crystallizations, and then we choose to use a simple and well-know PFM instead of this new approach.

## 2.2 Numerical integration of the phase-field equations

The equations for $\phi(t)$ and $u(t)$ ((2.22) and (2.23)) with the parameters that control their temporal evolution (equations (2.31), (2.32), (2.25) and (2.34)) constitute the PFM that we are solving.

In this work, these equations are numerically solved in two and three dimensions in a square or cubic lattice respectively and are spatially and temporally discretized using finite differences on an uniform grid with a constant mesh spacing $\Delta x$ in all directions. The number of cells of the lattice for all the simulations is 1000x1000 in $2D$ and 450x450x450 in $3D$ with periodic boundary conditions. One exception to this are the one particle simulations where the lattices are set to 256x256 and 256x256x256 cells. We use for the two equations an explicit time-differencing scheme that is first-order accurate in $\Delta t$ and uses a second-order representation for the spatial derivative, the so-called FTCS representation (Forward Time Centered Space) [97]. Once $\Delta x$ is fixed we must ensure the numerical stability of this scheme; as $\phi(t)$ and $u(t)$ have different time scales due to the presence of the $m$ parameter, the most restrictive condi-

tion must be implemented. Neglecting the terms with coupling between $\phi$ and $u$, the stability criterion is:

$$\Delta t \leq \frac{\Delta x^2}{4m} \quad \text{for the } \phi \text{ equation} \tag{2.35}$$

$$\Delta t \leq \frac{\Delta x^2}{4} \quad \text{for the } u \text{ equation} \tag{2.36}$$

As will be shown, $m$ is lower than 1, then $\Delta t$ must obey the second condition (2.36). The effect of the other terms would be a slightly more restrictive condition for the time step. In any case, for each simulation the numerical stability is checked. There are other numerical schemes, more sophisticated, that allow the use of any time step but the equations must fulfill certain conditions. One of this methods is the ADI scheme [97] and can be applied to the phase-field equations of our model in transformations with constant diffusion coefficient, but not when this coefficient is a function of the concentration field $u(t)$. As in our work we will compare simulations of both type of transformations, we opted for using the FTCS scheme.

The simulations can cover several supersaturation regimes, from low to high concentration gradients between the new particles and the amorphous matrix. In particular, values of the $S$ parameter of 0.2, 0.5 and 0.8 have been considered. The remaining PFM parameters have been chosen according to the following guidelines. The characteristic length $w$ must be as large as the longest relevant spatial scale. $\alpha$ is the inverse of a capillary length, i.e, is inversely proportional to the surface free energy that in order to minimize surface effects, must be small; therefore, $\alpha$ has to be large. The value for $\varepsilon$ must be as small as an interface should be, i.e., smaller than the evolving structure in order to approximate the sharp-interface limit, but it should also be large enough to perform the simulations in a reasonable time. That is because $\Delta x$ must be chosen equal or smaller than $\varepsilon$ in order to assure numerical accuracy and then according to (2.36), smaller $\varepsilon$ implies smaller $\Delta t$ and hence more computing time. The reason why $\Delta x$ must be similar to $\varepsilon$ is because the interface must have enough points in the grid in order to be numerically resolved. In this work the values of $\Delta x$ and $\varepsilon$ has been set equal and several tests has been performed in order to assure that the results are independent of this particular choice. In particular is useful to check that diminishing $\Delta x$ does not affect the results significantly and also that using a smaller interface width (and hence, smaller $\Delta x$) will lead to the same results. It is worth to note here that the value of $\Delta x$ has to be small enough in order to avoid the anisotropy in the grain growth as a consequence of the spatial discretization, and hence several simulations have to be done with several $\Delta x$ values to check if this anisotropy really appears. Finally, the $m$ parameter has been chosen in order to minimize the transient stage in which the grains grow by interface and consequently a small value has been used. With all these requirements in mind, the values used in this work are the following:

$$\Delta x = 0.005, \quad \Delta t = 2.5 \cdot 10^{-6}, \quad \varepsilon = 0.005, \quad m = 0.05, \quad \alpha = 400 \tag{2.37}$$

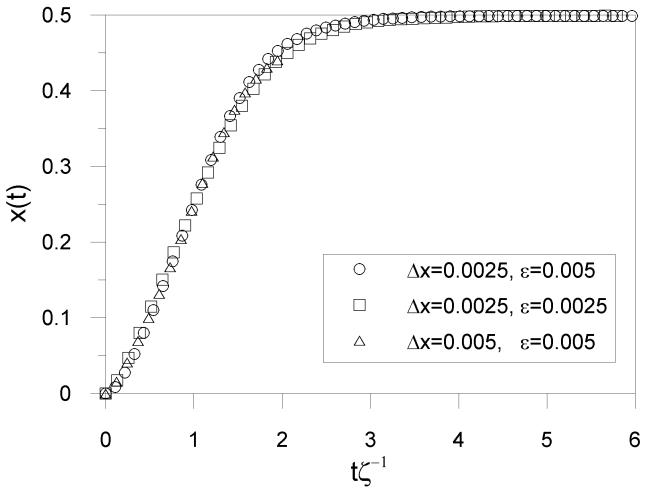


Figure 2.3: Comparison between the transformed fraction of several simulations performed with different values of $\varepsilon$ and $\Delta x$.

for simulations with constant diffusion coefficient, and:

$$\Delta x = 0.0025, \quad \Delta t = 1 \cdot 10^{-6}, \quad \varepsilon = 0.0025, \quad m = 0.05, \quad \alpha = 400 \qquad (2.38)$$

in the case of a diffusion coefficient with a concentration dependence. For high values of the supersaturation ($S$) the second set of parameters has been used for simulations with both kinds of diffusion coefficient. In these cases, as the concentration gradients extend over a small area surrounding the grains, the interface is thinner implying the use of a thinner discretization. In figure 2.3 are shown the results of several simulations for a single particle in $2D$ dimensions with different values of $\Delta x$ and $\varepsilon$ to check that the results are really independent of the particular choice used. As can be seen all the results are equivalent, justifying the use of the chosen $\Delta x$, $\Delta t$ and $\varepsilon$ parameters.

In each simulation each particle grows according to the dynamics given by the phase-field equations from an initial seed that is nucleated following an external nucleation law that can be composition dependent. Details of the several nucleation protocols used throughout this work will be shown in sections 3.3 and 3.4 but in all the cases the seed is randomly placed in the simulation box. The initial value of the $\phi$ and $u$ variables is set to 1 and $-1$ respectively, in the amorphous matrix, and when a nucleus appear the values of these variables in several cells in a square or cubic shape, depending on the dimensionality of the simulation, are changed to 0. The number of cells that constitute the initial nucleus must be enough to assure that its size is bigger than the critical radius below which the nucleus is not stable and is dissolved in the matrix. The initial radius of the simulation is found equaling the area or volume of the initial cells with the area or volume of a spherical grain and then comparing it with the

critical radius. That initial radius must be slightly greater than the critical one due to our simulated radius is square or cubic instead of spherical, and hence it has more superficial energy.

Finally, the results presented in this thesis correspond to the average over 10 simulations. This number of simulations ensures within a 95% of confidence an absolute error that follows a $n^{1/2}$ law, where $n$ is the number of simulations. According to the central limit theorem, performing more simulations will result in a reduction of the absolute error without varying significantly the average. In all the simulations the transformed fraction is calculated as the ratio between the number of cells with $\phi < 0.5$ and the total number of cells and represented as function of $t\zeta^{-1}$, where $\zeta$ is the time needed for the transformed fraction to be the half of its final fraction .

## 2.3 Example cases

Before using the PFM presented in the above sections to study primary crystallization, it will be used to study simpler cases for which analytical results exist. That will allow us to check that this particular PFM is able to reproduce a physical system, and thus, is a useful tool to study complex kinetics in phase transformations. Moreover, as the simulated concentration profiles in a primary crystallization are different than the real ones (recall figures 1.1 and 2.2), it must be assured that the mass is conserved along all the transformation.

### 2.3.1 Diffusionless transformations

The first case that will be simulated is a diffusionless first order phase transformation. In that case, the value of the concentration field is constant along the transformation and thus, there will be no diffusion and no coupling between the the phase-field variable and the concentration field. The propagation rate of an interface and its growth laws are well known [98] and will be compared with the results of simulations with a constant concentration field ($u = -1$).

Following [98] the kinetics of a system towards equilibrium may be described in terms of the time evolution of a pertinent order parameter, in our case the phase-field variable $\phi$. If this parameter is not constrained by any conservation law its time evolution can be described by a Landau-Ginzburg equation:

$$\frac{\varepsilon}{m}\frac{d\phi}{dt} = -\frac{\delta F}{\delta \phi} \tag{2.39}$$

where $F$ is the total free energy that can be expressed in terms of a free energy density $f_0$ that accounts for the homogeneous situation without interface and in terms of a gradient of $\phi$ to take into account the interface, so that equation (2.39) becomes

$$\frac{\varepsilon}{m}\frac{d\phi}{dt} = \varepsilon \overrightarrow{\bigtriangledown}^2 \phi - \frac{\partial f_0}{\partial \phi} \tag{2.40}$$

The free energy density can be expanded in terms of the phase-field parameter as:

$$f_0 = A\phi^2 + B\phi^3 + C\phi^4 + ... \tag{2.41}$$

and unless the coefficient $B$ happens to be identically zero because of symmetry, it is possible to truncate the series after the fourth order term. Assuming that there is no orientational dependence of $\phi$, that the interface width is very small compared to the size of the transformed region and that the interface profile is shape invariant during propagation, equation (2.40) can be written as:

$$\varepsilon\frac{d^2\phi}{dX^2} + \frac{\varepsilon}{m}v\frac{d\phi}{dX} - \frac{\partial f_0}{\partial\phi} = 0 \tag{2.42}$$

where $X$ is the distance measured from $R(t)$ and $v$ is the asymptotic interface velocity:

$$v = \frac{dR}{dt} + \frac{m(p-1)}{R} \tag{2.43}$$

$p$ being the dimensionality. A particular solution of the system of equations (2.42) and (2.43) is:

$$\phi(X) = \frac{1}{1 + exp(\sqrt{\frac{2C}{\varepsilon}}X)} \tag{2.44}$$

$$t = \frac{1}{v}\left\{(R - R_0) + R_c ln(1 + \frac{R - R_0}{R_0 - R_c})\right\} \tag{2.45}$$

$$v = -\frac{m}{4\varepsilon}\sqrt{\frac{\epsilon}{2(-C)}}\left\{3\sqrt{9B^2 - 32AC} - 3B\right\} \tag{2.46}$$

where $R_0$ is the initial radius, $R_c = \frac{m(p-1)}{v}$ is the critical nucleation radius and $A$, $B$ and $C$ can be expressed in terms of the PFM parameters comparing equations (2.22) and (2.40):

$$A = \frac{1}{4\varepsilon}, \qquad B = -10\alpha Su - \frac{1}{2\varepsilon}, \qquad C = 15\alpha Su + \frac{1}{4\varepsilon} \tag{2.47}$$

In these relations, $u$ represents the value of the concentration field at the interface that in that case is fixed to $-1$.

Equation (2.45) has been compared with simulations of the growth of one nucleus in 1, 2 and 3 dimensions and with supersaturation values of 0.2, 0.5 and 0.8 (figure 2.4). One-dimensional simulations correspond to the growth of a planar front and have been carried out in a grid with 1000 cells and with the values for the PFM parameters described in 2.37. Two and three-dimensional simulations correspond to the growth of a disk and a sphere, respectively, and the simulations are performed in the same conditions as the ones described for the one particle simulations in section 2.2. As can be seen the agreement is excellent in all dimensions and with all the supersaturation values except for 0.2. That is because for low supersaturation values the width of the interface

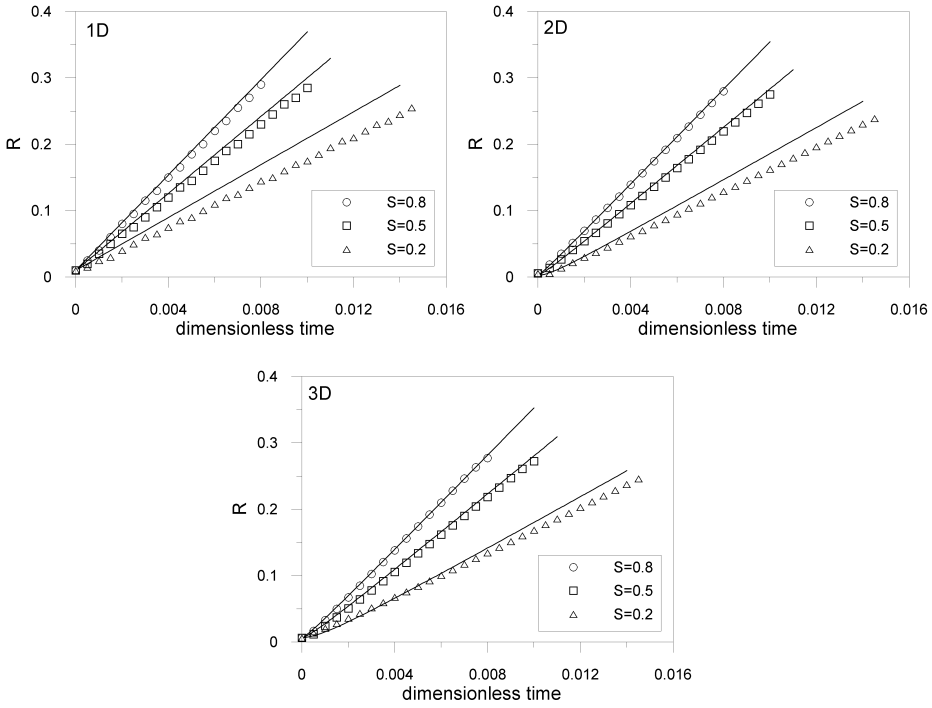


Figure 2.4: Comparison between equation 2.45 (solid lines) and PFM simulations for different supersaturations $S$

becomes larger and then the condition of having a width very small compared with the transformed region is not fulfilled and hence the equation (2.42) is not a good approximation to the system. However, for 2 and 3 dimensions and in the first stages of the transformation, the model reproduces the theory and hence, these approximate expressions describe proprerly the growth of an interface. That result is important for two reasons: *(a)* as explained before, it allow us to check the ability of the PFM to simulate phyisical systems and *(b)* as pointed out in section 1.1.2, the growth of the new phase in a primary crystallization is characterized by a two stage mechanism, being the first one an interface controlled growth that is followed by a diffusion controlled growth. Then, equations (2.45) and (2.46) will be used to describe the interface controlled stage of the growth in the simulations of primary crystallization presented in the next chapters.

### 2.3.2 Concentration profiles

The second case that will be studied is the description of the concentration profiles surrounding the grains of the new phase. In the classic work by Zener

[43] the growth of a spherical precipitate in any dimension from solid solution was analytically calculated. Moreover, the concentration of solute around the precipitate (i.e. the concentration profile) was also calculated. We can compare the results of our PFM simulations with this theoretical result, that we summarize next. It is important to note here that the growth law deduced by Zener can not be used to describe primary crystallization mainly because only the diffusion controlled growth of a grain in an infinite matrix is considered. Therefore, the transient stage in which the grains grow by interface and the impingement between the grain as they grow are not considered. Then, the results of his work are valid in the diffusion controlled regime and before the soft-impingement occurs and it is when the simulated profiles can be compared with the analytical results.

In his work, Zener solves the diffusion equation with a constant diffusion coefficient, $D$, in an infinite region and with the following boundary conditions: *a)* the concentration in any point at the initial time is the concentration in the matrix far away from the precipitate ($c_0$), *b)* the value of the concentration at the interface is the concentration in the matrix which is in equilibrium with the precipitate ($c_l$) and *c)* the rate at which the interface grows is controlled by diffusion. With these conditions, the concentration profile can be written as:

$$c = c_0 + (c_l - c_0)\frac{\xi_\lambda\,(r/(Dt)^{1/2})}{\xi_\lambda\,(\alpha_\lambda)} \tag{2.48}$$

where

$$\xi_\lambda\,(x) = \int_x^\infty e^{-\frac{1}{4}z^2} z^{1-\lambda} dz \tag{2.49}$$

and $\alpha_\lambda$ can be found implicitly with the following equation[1]:

$$S^{-1}(\alpha_\lambda)^\lambda = 2\frac{exp(-\alpha_\lambda^2/4)}{\xi_\lambda\,(\alpha_\lambda)} \tag{2.50}$$

where $\lambda$ is the dimensionality and $S$ the supersaturation value.

In our simulations $c_0 = 0$ and $c_l = 1$. With these values and for a fixed time, we can compare equation (2.48) with the simulation results for 1, 2 and 3 dimensions (see figure 2.5). As can be seen, in all the cases the agreement is excellent. It is worth to note here that we plot the absolute value of the dimensionless concentration (that takes values between $-1$ and 0) in order to compare with the predicted ones (between 0 and 1).

### 2.3.3 Mass balance

To check the mass conservation with this PFM, the concentration $c(\overrightarrow{r})$ must be written in terms of the dimensionless one $u(\overrightarrow{r})$. From equation (2.31) we

[1] To take into account that in the simulations there is a first stage of the growth that is interface controlled, we must multiply this constant by a factor close to 1. That will be explained and justified in chapter 3

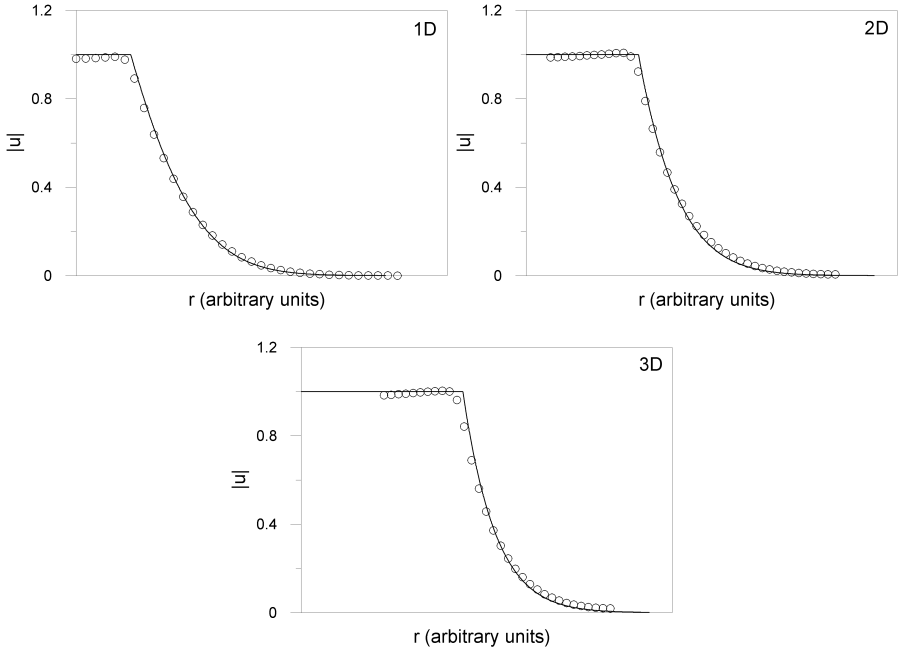


Figure 2.5: Concentration profiles obtained by means of PFM simulations (symbols) with a supersaturation of 0.5 compared with the theoretical profiles calculated by Zener (solid lines)

have:

$$c(\overrightarrow{r}) = 1 + [1 - c_0]\, u(\overrightarrow{r}) \tag{2.51}$$

and from equation (2.32) we can relate $c_0$ with the supersaturation value $S$: $S = 1 - c_0$, equation (2.51) becoming:

$$c(\overrightarrow{r}) = 1 + Su(\overrightarrow{r}) \tag{2.52}$$

As explained in section 2.1.2, in the simulations the new stable crystallites have the same concentration as the equilibrium concentration of the matrix at the interface and hence what we must assure is that at any instant of time the mass outside the crystallites (in the untransformed region) is the same as the mass at the beginning of the transformation, when all the matrix was unstable. Then, the equation that must be verified is:

$$\int_{nt} c(\overrightarrow{r}) d\overrightarrow{r} = \int_{nt} [1 + Su(\overrightarrow{r})]\, d\overrightarrow{r} = c_0 V_{nt}^0 = (1 - S) V_{nt}^0 \tag{2.53}$$

where the subindex $nt$ stands for the non-transformed volume and then $V_{nt}^0$ is the initial non-transformed volume that have $c_0$ at the onset of the transformation. Equation (2.53) has been calculated in all the simulations performed in

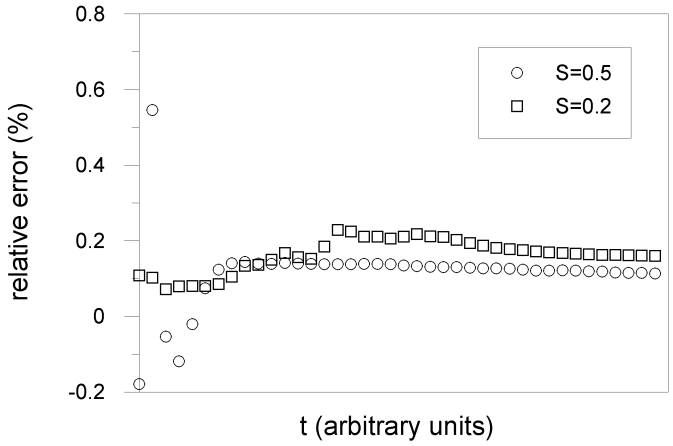


Figure 2.6: Mass conservation in simulations with preexisting nucleation in a 1000x1000 system (symbols).

the next chapters, with the integral being computed with the Simpson's rule [97] and the non-transformed volume as the number of cells with $\phi > 0.5$. Excellent agreement is found in all the cases, as for example $2D$ simulations with 125 preexisting nuclei in a 1000x1000 system and supersaturation values of 0.2 and 0.5 and the PFM parameters described in 2.37 (see figure 2.6). The bigger discrepancies (with relative errors about 1% in all the simulations) are found at the beginning of the transformation when the equilibrium concentration of the matrix at the interface is not reached yet and when the effects of the discretization of the grid are more important.

As an overall conclusion, it can be said that the PFM used in this work is capable of reproducing several physical cases (constant growth rate transformations and the concentration profiles in a diffusion controlled growth) and fulfilling a general physical law (mass conservation). In the next chapters it will be used to the study of primary crystallizations.

# Chapter 3

# Simulations with constant $D$

In this chapter the kinetics of primary crystallization will be studied in two different ways. First of all, the non-random nucleation model introduced in section 1.2.2 will be modified and used as a geometrical first order approximation for taking into account the SI and NRN effects. This model, as well as the mean-field model, also seen in section 1.2.2, will be compared with the features usually observed in actual kinetics of primary crystallization. Then, phase-field model simulations with constant diffusion coefficient will be presented. Two different nucleation protocols will be studied. Firstly, transformations with pre-existing nucleation. In this case, as all the nuclei are born at the same time, possible effects of the nucleation on the kinetics are discarded, thus, allowing to study how the impingement between the concentration gradients of neighbouring grains affects the overall kinetics of the transformation. Secondly, transformations with continuous nucleation are presented. In that case, the effect of the reduction in the nucleation probability due to the stabilization of the amorphous matrix as the crystallization proceeds can be studied. The simulation results will be compared with the theoretical models. Before presenting the results of these systems, simulations of a single isolated particle will be shown. These one-particle simulations yield the kinetics of a non-interacting grain that will be used in order to compute the $N$-particle transformation kinetics.

In all the simulations presented in this chapter and the next one, primary crystallization with a high nuclei density are studied. In this way, nuclei do not lose its spherical shape and the performed analysis does not need to deal with the problem of the unstabilization of the interface.

## 3.1 Kinetic models of primary crystallizations

### 3.1.1 The geometrical model:

This model accounts for the geometrical distribution of the transformed phase and the surrounding stabilized matrix regions [99]. It performs a simplified local mass balance of a growing crystalline grain. A similar approach was already used

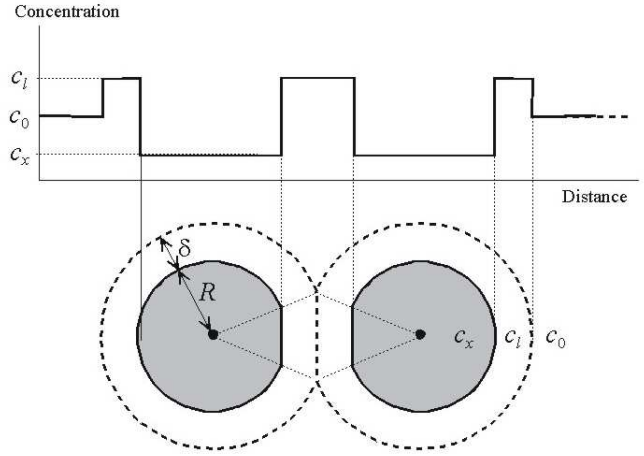


Figure 3.1: Scheme of the geometrical model proposed to approximate the impingement between grains in primary crystallization. Recall that $c_x$ is the crystallite concentration and $c_0$ is the initial concentration of the amorphous precursor.

by Shepilov in [68] with the assumption that the supersaturation should be small ($\gamma < 1$). In the present subsection a relation between $x(t)$ and $\widetilde{x}(t)$ valid for any value of $\gamma$ is derived.

Following reference [99] a drastic simplification of the concentration profile around an isolated grain is considered, substituting it by a completely stabilized boundary zone as sketched in figure 3.1. This stabilized boundary zone, with different thickness $\delta(\tau, t)$ for grains nucleated at different times $\tau$, will be assumed to have an equilibrium concentration $c_l$. In an isolated spherical grain, the thickness $\delta(\tau, t)$ can be obtained by means of a local mass balance between the volume of the stabilized boundary zone and the volume of the corresponding transformed grain. This means

$$R^3(\tau, t)(c_0 - c_x) = \left[[R(\tau, t) + \delta(\tau, t)]^3 - R(\tau, t)^3\right](c_l - c_0) \tag{3.1}$$

$$R_{TB}(\tau, t) \equiv R(\tau, t) + \delta(\tau, t) = \gamma^{-\frac{1}{3}} R(\tau, t) \tag{3.2}$$

where $R$ is the radius of the crystallite and $R_{TB}$ is defined as the radius of the spherical *Transformed plus Boundary* zone including both the crystallized and the stabilized zones.

We will now define $x_{TB}(t)$ as the volume fraction occupied by the transformed phase plus the stabilized boundaries around the growing grains. Neglecting impingement, each individual crystalline grain plus its boundary region has an spherical shape, and consequently its behavior along the growth is the

same as that of virtual *stable phase grains* of radius $R_{TB}(\tau,t)$. Thus, an *extended Transformed plus Boundary* volume fraction, $\widetilde{x}_{TB}$, can be defined as

$$\begin{aligned}\widetilde{x}_{TB}(t) &= \tfrac{4\pi}{3}\int_0^t I(\tau)\left[R_{TB}(\tau,t)\right]^3 d\tau = \\ &= \tfrac{4\pi}{3}\int_0^t I(\tau)\,\gamma^{-1}R^3(\tau,t)\,d\tau\end{aligned} \tag{3.3}$$

and from the extended fraction definition (equation (1.15)) and (3.3)

$$\widetilde{x}(t) = \gamma\widetilde{x}_{TB}(t). \tag{3.4}$$

Interference between the growing grains (SI effect) can now be treated including the stabilized boundary zone. The overlap of the concentration profiles responsible for the SI will be approximated by considering that the crystallite growth does not stop by direct interface impingement, but because of the impingement of the stabilized boundary zones as sketched in figure 3.1. More precisely, let us define $\Omega_i(t)$, the free solid angle function of a certain crystalline grain $i$, as the solid angle of its boundary zone which has not impinged upon other neighboring boundary zones. We will impose that the grain interface corresponding to this solid angle $\Omega_i(t)$ continues growing unaffected by the impingement with the same growth law as an isolated grain, while the growth of the rest of the interface is utterly inhibited. Thus, we can express the transformed fraction due to the $i$-grain as

$$x_i(t) = \int_\tau^t \Omega_i(t')R(\tau,t')^2 G(\tau,t')\,dt' \tag{3.5}$$

where $G(\tau,t) = \frac{dR(\tau,t)}{dt}$ is the growth rate at time $t$ of a grain born at time $\tau$. Therefore, the total transformed fraction will be

$$x(t) = \sum_{i=1}^{N(t)} x_i(t) = \sum_{i=1}^{N(t)} \int_\tau^t \Omega_i(t')R(\tau,t')^2 G(\tau,t')\,dt' \tag{3.6}$$

where $N(t)$ is the number of grains at time $t$.

Similarly, for the transformed plus boundary fraction, remembering that $R_{TB}(\tau,t) = \gamma^{-\frac{1}{3}}R(\tau,t)$, we obtain

$$\begin{aligned}x_{TB}(t) &= \sum_{i=1}^{N(t)} x_{TB,i}(t) = \\ &= \sum_{i=1}^{N(t)} \int_\tau^t \Omega_i(t')R_{TB}(\tau,t')^2 \tfrac{dR_{TB}}{dt'}dt' = \\ &= \gamma^{-1}\sum_{i=1}^{N(t)} \int_\tau^t \Omega_i(t')R(\tau,t')^2 G(\tau,t')\,dt'\end{aligned} \tag{3.7}$$

Then, from equations (3.6) and (3.7), the actual transformed volume fraction is directly related to the transformed plus boundary volume fraction as

$$x(t) = \gamma x_{TB}(t) \tag{3.8}$$

The same relation is obtained considering a global solute mass balance

$$x(t)\, c_x + [x_{TB}(t) - x(t)]\, c_l + [1 - x_{TB}(t)]\, c_0 = c_0 \tag{3.9}$$

Although the untransformed matrix stabilization and the concentration profiles overlap are dealt here with extreme simplification, the shape evolution of actual grains will be very similar to the one resulting from this approximation. Figure 3.1 shows that, in the proposed simplification, the facing grain interfaces are flat. The flat interface is a natural result of the impingement between two grains born at the same time, independently of the growth rate. In the case of grains born at different times, its direct impingement does not lead, in general, to a flat interface, only in the case that the grains' radius follow a parabolic law ($R(\tau, t) \propto (t-\tau)^{\frac{1}{2}}$) as expected in diffusion-controlled growth. In the actual physical situation these interfaces would not be flat, but the relationship between $x(t)$ and $x_{TB}(t)$ would hold equally because it is not dependent on the grain interface shapes, as shown by equation (3.9).

The NRN will be approximated in this model by assuming that nucleation is completely inhibited in the boundary area of completely stabilized untransformed matrix, while remains unaffected in the rest of the untransformed volume. This is also a first order approximation because in a real system the nucleation probability would be related to the matrix concentration value, thus leading to a continuously decreasing nucleation probability when going from far away to near the crystalline grains.

As a consequence of the above assumptions, the evolution of $x_{TB}$ can be seen as a process with random nucleation at the $1 - x_{TB}$ zone, isotropic growth rate $\gamma^{-\frac{1}{3}} G$ and direct impingement between the transformed plus boundary domains, which then satisfies a KJMA-like equation [57]. Thus, $x_{TB}$ can be obtained from

$$\begin{gathered} \frac{dx_{TB}(t)}{d\widetilde{x}_{TB}(t)} = 1 - x_{TB}(t) \\ x_{TB}(t) = 1 - \exp\left[-\widetilde{x}_{TB}(t)\right] \end{gathered} \tag{3.10}$$

Equations (3.4) and (3.8) allow us to rewrite the previous equation as

$$\gamma^{-1} x(t) = 1 - \exp\left[-\gamma^{-1}\widetilde{x}(t)\right], \tag{3.11}$$

showing that $x_{TB}$ is equivalent to $\xi$, the transformed fraction normalized by the supersaturation value defined in section 1.2. This equation leads to a final value of the transformed fraction equal to $\gamma$ because of the exhaustion of the non-stabilized part of the untransformed volume as the crystallized plus stabilized volume occupy the whole space. Equation (3.11) is identical to equation (1.17), which is in fact the common way of using the KJMA theory in primary crystallization [39]. From the geometrical model just exposed, equation (1.17) is just a first order approximation for taking into account the SI and NRN effects.

### 3.1.2 Actual kinetics of primary crystallization:

The geometrical model presented above and the mean field model explained in section 1.2.2 are extremely opposite models of accounting for the same phe-

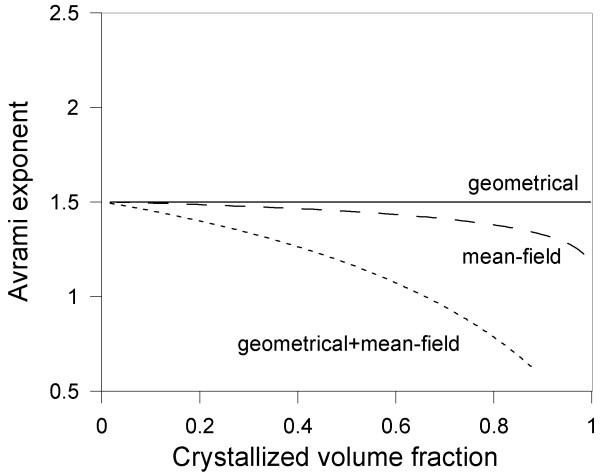


Figure 3.2: Avrami exponents calculated using the geometrical and mean-field models in a transformation with diffusion-controlled growth

nomenon. The geometrical model deals with the stabilization of the untransformed matrix as a pure local effect, utterly modifying in some zones the nucleation and growth kinetics. On the contrary, the mean-field model deals with the stabilization of the matrix as a global effect equally affecting the nucleation and growth of all the growing crystallites. These two approaches are not able to account for the complex behaviors commonly observed in experimental transformed fraction curves of primary crystallization [53, 65, 66, 67].

As already stated, the analysis of primary crystallization is commonly performed using equations (1.17) and (1.18), where the transformed fractions $x(t)$ and $\widetilde{x}(t)$ are substituted by $\xi(t)$ and $\widetilde{\xi}(t)$. A quick examination shows that it is not possible to give physical interpretations to the low Avrami exponents frequently reported in primary crystallization (see section 1.2) using *either* the geometrical model or the mean-field model described above . Figure 3.2 shows the Avrami exponents calculated using equation (1.18) for both the geometrical and the mean-field models in a transformation with pre-existing nuclei and assuming a steady state diffusion-controlled growth given by

$$G(R) = \frac{D}{R}\frac{c_l - c_0}{c_l - c_x} = \gamma\frac{D}{R}, \tag{3.12}$$

which corresponds to equation (1.11) with $\lambda = \left(\frac{c_l - c_0}{c_l - c_x}\right)^{\frac{1}{2}}$. In the case of the mean-field model this growth rate is modified giving

$$G(R) = \frac{D}{R}\frac{c_l - c(t)}{c_l - c_x} = \frac{D}{R}\gamma\varphi(t). \tag{3.13}$$

One can observe that although the mean-field model predicts a decreasing exponent at the final stages of the transformation it is not able to account for the $n < 1$ values shown in figure 1.7. From comparison of figures 1.7 and 3.2 it is clear that the first order approaches to the SI and NRN effects of the previous section are not able to describe the actual kinetics of primary crystallization in amorphous alloys.

Nevertheless, calorimetric data of primary crystallization of amorphous alloys was successfully described within the framework of the KJMA kinetics [48]. In that work the kinetics of primary crystallization in an amorphous metallic alloy were well-described by a kinetic model, which is, in main terms, a juxtaposition of the geometrical and mean-field models discussed above. Experimental data on glass crystallization was interpreted by a mean-field reduction of the kinetic parameters (very similar to the mean-field model above) plus a normalized KJMA equation (geometrical model). Dotted line in figure 3.2 shows that this combination of the geometrical and mean-field models (the *geometrical+mean-field* model) give the low values of the Avrami exponent observed in experimental data. The model in ref. [48] and other similar models available in literature [100][101] were defined as accounting for the SI and NRN effects but, in fact they are taking into account, although in first order approximations, two times such effects; they consider the stabilization of the untransformed matrix as a local geometrical phenomenon and also as global effect.

The next sections and chapters of the present thesis are devoted to the comparison between phase-field model simulations of primary crystallization and the two models discused above, i.e., the geometrical and the mean-field model. Moreover, the fact that the combination of these two models reproduces the features obtained in experimental data will be taken into account. In the PFM simulations, the soft-impingement and the non-random nucleation can be naturally included, so comparing them with the combination of the two models (*geometrical+mean-field* model) will allow us to discern if these two effects are the responsible of the observed kinetics in primary crystallization.

## 3.2 Growth of a single particle

The comparison between the $N$-particle simulations and the theoretical models requires the knowledge of the kinetics of one isolated particle. Thus, single-particle simulations are performed and analysed, yielding the growth of one crystallite that will be used to compute the extended transformed fraction in the models with preexisting and constant nucleation.

Phase-Field equations (2.22) and (2.23) yield a spherical particle growth with two different stages. At the beginning of the transformation a transient interface-controlled growth controls the particle evolution. During this stage, the concentration field is being progressively piled up at the particle/matrix interface. As that process is controlled by the difference in the Gibbs free energy between the two phases, it can be treated as a diffusionless transformation and,

hence, equation (2.45) can be used to describe the temporal evolution of the particle radius. Once the concentration at the interface reaches the equilibrium concentration between the two phases, the growth becomes diffusion-controlled with a growth law of the kind of equation (1.11). Then, the radius of the isolated particle at time $t$ can be written as:

$$R(t) = R_i(t)\theta(t_c - t) + R_d(t)\theta(t - t_c) \tag{3.14}$$

where $R_i(t)$ is the radius for the interface controlled growth obtained implicitly from equation (2.45), $R_d(t)$ is the radius for the diffusion controlled growth obtained from equation (1.11) with the proper continuity conditions at $t_c$, i.e:

$$R_d(t) = \lambda\sqrt{Dt} - \left[\lambda\sqrt{Dt_c} - R_i(t_c)\right] \tag{3.15}$$

and $t_c$ is the time when the growth mechanism changes.

In Zener's work [43] equation (1.11) is derived assuming that the particle grows by a diffusion-controlled mechanism since the initial time, and it also gives an expression for the parameter $\lambda$ as a function of the supersaturation (equation (2.50)). As far as we know, there are no analytical results for the growth of a grain under diffusion taking into account the transient stage in which the growth is interface-controlled, thus we can not use the $\lambda$ values given by Zener. Following reference [44], where it is shown that all the analytical approximations to a diffusion-controlled growth are of the form $\lambda\sqrt{Dt}$ (see section 1.1.2), we will also assume this dependence. Therefore, the $\lambda$ values will be obtained fitting the results of single particle PFM simulations in two and three dimensions and for different supersaturations, and will be compared with the values obtained in the Zener solution.

### 3.2.1 $2D$ simulations:

According to section 2.2, single particle simulations have been performed in a 256x256 lattice. From the computed transformed fraction $x(t)$, the time evolution of the particle radius is:

$$R_{sim}(t) = L\left(\frac{x(t)}{\pi}\right)^{1/2} \tag{3.16}$$

where $R_{sim}(t)$ stands for the radius determined from the PFM simulation in a lattice of $L$x$L$ size. The interface velocity is calculated taking the radius derivative. In order to fit only the growth of an isolated particle, the last stages of the simulation are discarded because of the self-interaction of the particle due to the periodic boundary conditions, causing a loss of spherical simetry and a delay in its growth. The effect of that interaction can be observed in a sudden change of the slope of the velocity vs. time graph (see figure 3.3). In order to fit equation (3.14) to the simulations, $t_c$ must be evaluated. This is done considering that the mechanism with a slower velocity it is the one that controls the growth. Therefore, at any instant of time the velocity of a particle with

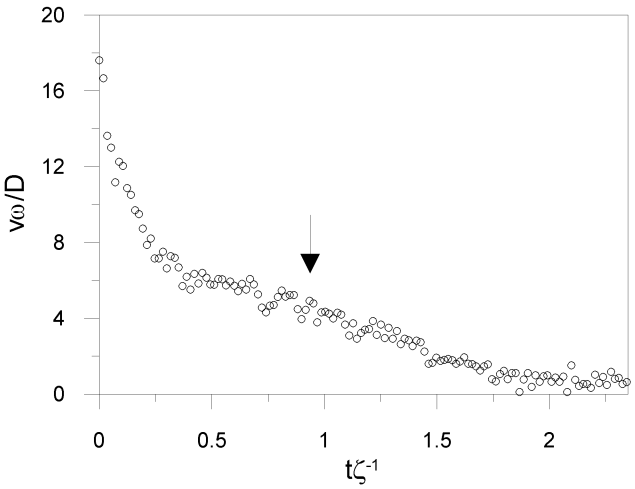


Figure 3.3: Dimensionless velocity versus time from a $2D$ simulation of one single particle growing with a supersaturation of 0.5. The arrow indicates the moment in which the particle begins to interact with itself due to the periodic boundary conditions.

initial radius $R_0$ is calculated according to both mechanisms: *(a)* an interface-controlled growth, from the derivation of the solution of the implicit equation (2.45) and *(b)* a diffusion-controlled growth, from the derivation of equation (3.15). As can be seen in figure 3.4, at the beginning of the transformation the interface velocity is much slower than the diffusion one, whereas after certain time, it is larger and hence, a growth mechanism change occurs. Another factor that must be considered is the value of the concentration field at the interface, $u_{int}$ (that appears in equation (2.46) and needed in (2.45)). This value has been taken as $-0.5$, the mean value of $u_{int}$. In this way, from the one-particle simulation, the $\lambda$ parameter of the Zener's equation is calculated and used for the comparison between the N-particle simulations and the kinetics models.

The results of the fitting can be seen in figures 3.5-3.7 corresponding to the growth of one single particle in $2D$ with different values of the supersaturation: from 0.2 to 0.8. In these figures, the symbols represent the PFM simulations and the solid line the equation (3.14) fitted to the curve in the case of the radius and the derivative of (3.14) in the case of the velocity. As can be seen, the agreement between the simulation results and the theoretical curves is better for lower values of the supersaturation. In these cases the time in which the particle is growing by interface is reduced, thus it can be said that there is only one growth mechanism and then the error introduced in the way $t_c$ is calculated is minimized. This error can be attributed mainly to the way the interface-controlled growth is modelled: a constant Gibbs free energy difference is assumed along all the growth process, a difference that in a real system

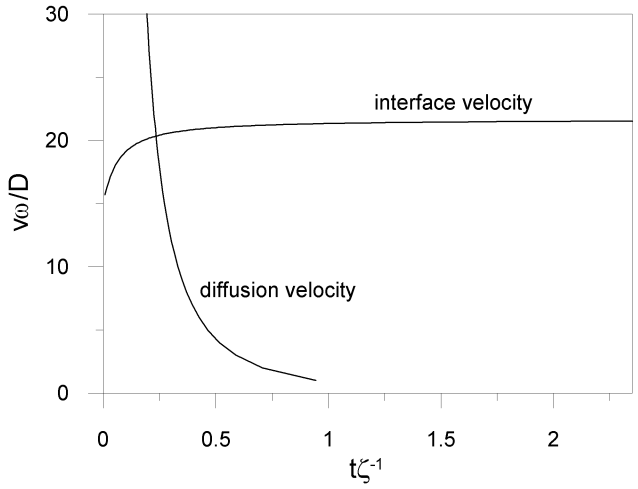


Figure 3.4: Diffusion and interface velocity of a single particle with an initial radius $R_0$ from equations 2.45 and 3.14. When the particle reaches certain size, the diffusion velocity becomes the smaller one, thus controlling the growth.

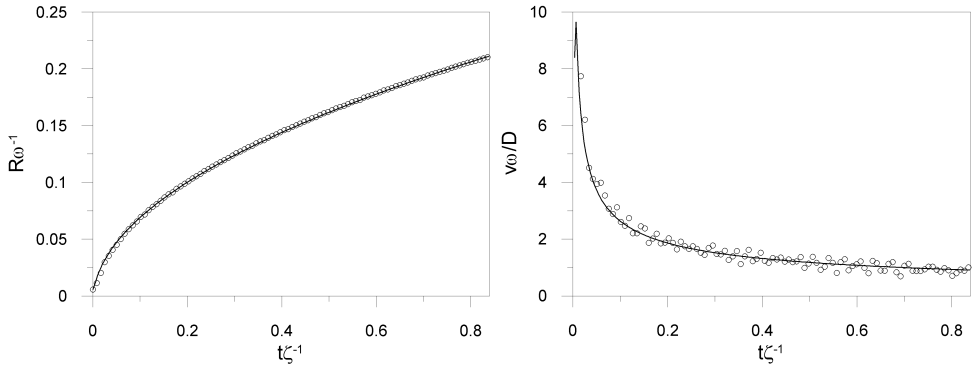


Figure 3.5: Dimensionless radius (left) and velocity (right) for one single particle in $2D$ with a supersaturation of 0.2

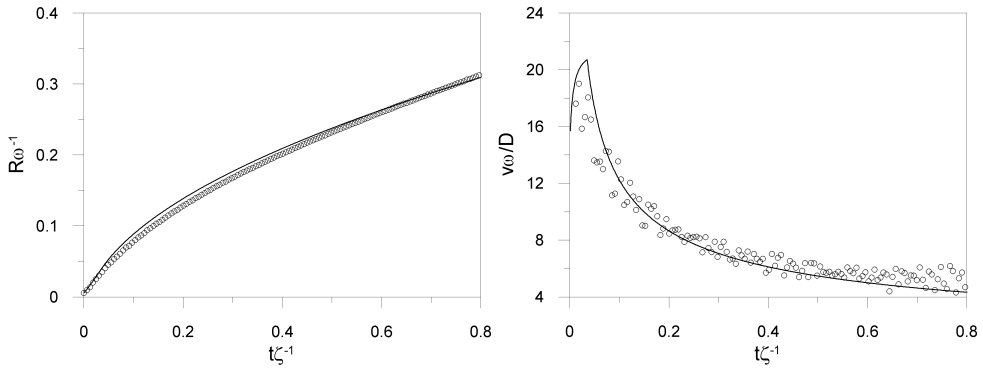


Figure 3.6: Dimensionless radius (left) and velocity (right) for one single particle in $2D$ with a supersaturation of 0.5

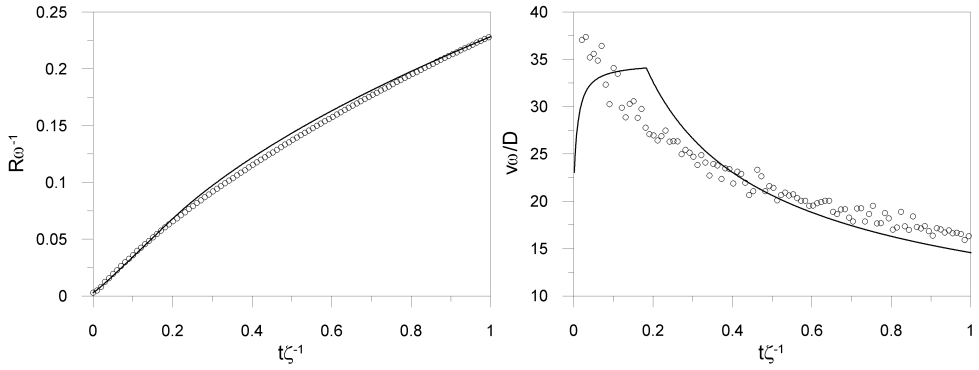


Figure 3.7: Dimensionless radius (left) and velocity (right) for one single particle in $2D$ with a supersaturation of 0.8

| $\gamma$ | $\lambda$ | $\lambda_Z$ | $\lambda/\lambda_Z$ |
|---|---|---|---|
| 0.2 | 0.629 | 0.629 | 1.00 |
| 0.5 | 1.718 | 1.562 | 1.10 |
| 0.8 | 2.909 | 3.636 | 0.80 |

Table 3.1: Values for the fitted parameters in one-single particle simulations in $2D$ as a function of the supersaturation $\gamma$

diminishes until the growth becomes diffusion-controlled. The values of the fitted parameter, namely $\lambda$, can be seen in table 3.1, as well as the quotient between $\lambda$ and the corresponding value obtained by Zener, $\lambda_Z$ (equation (2.50)). These values shows that for low supersaturations, when the time in which the interface-controlled growth transient is reduced, the Zener equation perfectly reproduces the simulation results. From these figures and table, the following conclusions can be stated: *a)* the transient stage before the growth becomes diffusion-controlled is not negligible, except for low values of $S$ and *b)* equation (3.14) is only a first-order approach to the growth of one single particle. Two main corrections can be done. First of all, the interface and diffusive process are simultaneous and not succesive and then, the change from one to the other must be smooth and not sharp as in figure 3.4 (in other words, the derivative of the velocity must be continuous). Secondly, the interface velocity depends on the value of the concentration field at the interface $u_{int}$, value that we fix to $-0.5$ at any time; but as the grain grows the concentration at the interface varies changing the interface velocity and, consequently, the time at which the diffusive velocity becomes smaller. These factors introduce an error in $t_c$ that mainly affects the calculation of the grain's velocity. As shown in figures 3.5-3.7, the radius evolution is well described by equation (3.14). Only in the case of large supersaturations ($S > 0.8$), where the transient is longer, these errors may have some effect. In this way, the transformed fraction evolution of a many particle system is not significantly modified by the approximation used in equation (3.14). Is for that reason, that this equation has been used throughout all this work, without the need of introducing a more precise model for the transition from an interface to a diffusion-controlled growth. Besides, the phase-field model parameters has been chosen in order to minimize as much as possible, this interface-controlled transient stage, as explained in section 2.2.

### 3.2.2 $3D$ simulations:

In the three dimensional case the radius of the growing sphere is obtained from the transformed fraction of a single particle simulation as:

$$R_{sim}(t) = L\left(\frac{3x(t)}{4\pi}\right)^{1/3} \tag{3.17}$$

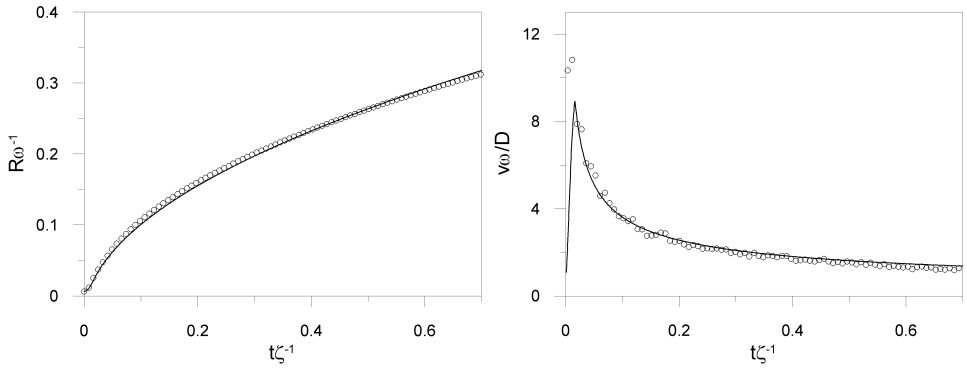


Figure 3.8: Dimensionless radius and velocity for one single particle in $3D$ with a supersaturation of 0.2

| $\gamma$ | $\lambda$ | $\lambda_Z$ | $\lambda/\lambda_Z$ |
|---|---|---|---|
| 0.2 | 0.976 | 0.908 | 1.075 |
| 0.5 | 2.335 | 2.076 | 1.125 |
| 0.8 | 3.674 | 4.593 | 0.80 |

Table 3.2: Values for the fitted parameters in one-single particle simulations in $3D$ as a function of the supersaturation $\gamma$

while the velocity has been calculated in the same way as the $2D$ case. The result of the fittings can be observed in figures 3.8-3.10. In this case, the value of $u_{int}$ has been also fixed to $-0.5$ and the parameter $\lambda$ is obtained from the fitting with the values seen in table 3.2. Observing the fitted curves and the $\lambda/\lambda_Z$ values, the same analysis done in the $2D$ case can be done: the effect of the transient stage is only significant for high values of the supersaturation and it mainly affects the velocity, not being important in the radius.

Moreover, in section 2.3.2, the concentration profiles in $1D$, $2D$ and $3D$ simulations were compared to Zener's analytical results, showing and excellent agreement between simulations and theorethical profiles. Thus, it can be concluded that PFM simulations, jointly with equation (3.14), are a useful tool to study primary crystallization.

## 3.3 Transformations with preexisting nucleation

In this section, simulation results for transformations with preexisting nucleation will be presented and compared with the *geometrical*, *mean-field* and

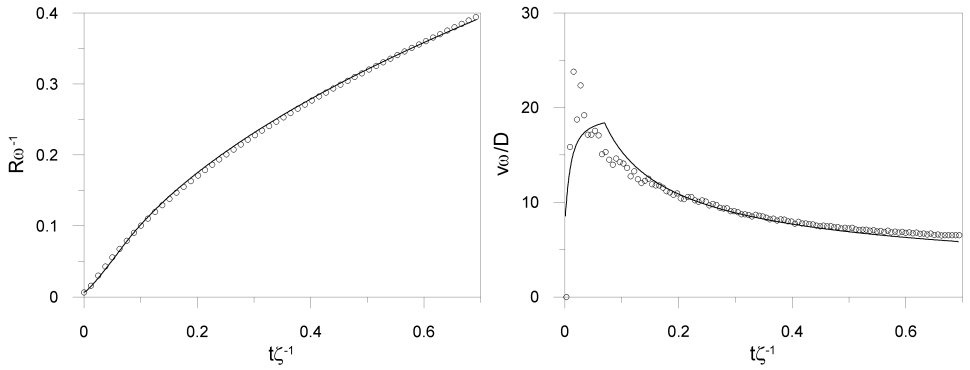


Figure 3.9: Dimensionless radius and velocity for one single particle in $3D$ with a supersaturation of $0.5$

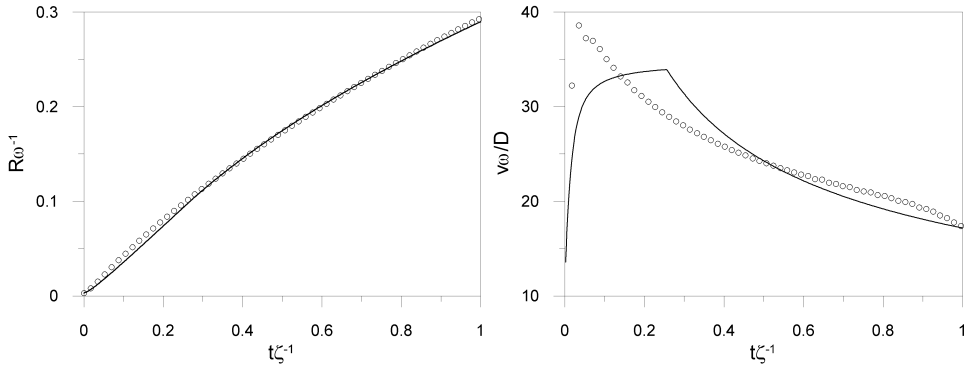


Figure 3.10: Dimensionless radius and velocity for one single particle in $3D$ with a supersaturation of $0.8$

| | $n$ | $R_c$ | $R_0^{sim}$ |
|---|---|---|---|
| $2D$ | 4 | 0.00288 | 0.0056 |
| $3D$ | 8 | 0.00576 | 0.0062 |

Table 3.3: Values for the initial and critical radius for supersaturation values of 0.2

*geometrical+mean-field* models. The extended transformed fraction of these models will be computed using the results for one particle growth obtained in the last section. First of all, the nucleation protocol is described followed by the results for the 2 and 3 dimensional cases and for different supersaturation values. Finally, a discussion about the transformed fraction evolution is presented compared with the expected evolution according to the theoretical models.

## Nucleation protocol

In these transformations a set of randomly distributed particle seeds starts growing with no further nucleation of particles. This case is widely found in the primary crystallization of some glasses, where the annealing treatment activates the growth of already existing quenched-in nuclei. The growth of 125 precipitate particles has been simulated setting for each grain the $u$ and $\phi$ values of $n$ cells to 0, which is the value of the concentration and the phase field variables for the crystalline phase. As explained in 2.2, this results in particles with an initial radius $R_0^{sim}$ equal to:

$$R_0^{sim}(2D) = \left(\frac{n}{\pi}\right)^{1/2} \Delta x \tag{3.18}$$

$$R_0^{sim}(3D) = \left(\frac{3n}{4\pi}\right)^{1/3} \Delta x \tag{3.19}$$

that must be slightly greater than the critical radius $R_c$ defined in equation (2.45). As $R_c$ depends on the supersaturation value (the higher the supersaturation, the lower $R_c$) and the dimensionality ($R_c$ is greater for $3D$ than for $2D$ ), it must be checked that in all the cases the seed is large enough to grow. In table 3.3 can be observed that for $S = 0.2$ (the most limiting case studied) the minimum number of cells is 4 in two dimensions (a 2x2 square) and 8 in three (a 2x2x2 cube). Thus, in order to do all the simulations with the same conditions, this values of $n$ have been used in all the cases.

## Results

In the numerical simulation, the particles have a known growth law detailed in the last section and the evolution of the concentration field in the matrix follows equation (1.7). Hence, the effects of the stabilization of the untransformed

matrix and the overlap of concentration fields of neighboring particles are naturally obtained [102, 99]. This allows us to quantify the SI effect in a system with well-known nucleation and growth laws. It is also worth to note here that the particle radius in the simulations are always in the size range in which the spherical shape is stable. As an example, figure 3.11 shows a view of the transformed phase and concentration field evolution in a partial region of a two-dimensional simulation with supersaturation $S = 0.2$. The interference between precipitated particles due to the overlap of the concentration fields and the change in the matrix concentration are clearly observed. Analogously, figure 3.12 shows the transformed phase in a three-dimensional simulation with $S = 0.2$; in that view, an early stage of the transformation can be seen ($x(t) = 0.003$), so the soft-impingement effect is still not important.

It is well known that nucleation and growth processes have scaling properties. Both the overall kinetics and the developed microstructures can be described in terms of dimensionless time and length parameters depending on the nucleation frequency and growth-rate values. Therefore, the parameters defining the characteristics of the simulated transformations are just the final transformed volume fraction $\gamma$ (that coincides with the supersaturation value $S$), the ratio between interface and diffusion growth rate and, in the case of continuos nucleation, the nucleation parameter $Q$. The growth ratio determines the relative influence of the transient interface-controlled and the diffusion-controlled growth regimes over the particle total growth and as stated before has been chosen to reduce the interface-controlled regime influence as much as possible within the limitations of the simulation process. The influence of the parameter $Q$ will be discused in the next section.

Figure 3.13 show the transformed fraction evolution and the Avrami exponent behavior in $2D$ and $3D$ for a system with a supersaturation of 0.5. This case is specially important because it represents a final transformed fraction of the order usually obtained in actual primary crystallization of metallic glasses [48]. In that figure, the results of the simulations are compared with the *geometrical*, the *mean-field* and the *geometrical+mean-field* models described before. In both two- and three-dimensional simulations the first two models reproduce with accuracy the $x(t)$ evolution while the last one gives always a slower kinetics. The initial values of the Avrami exponents are exactly the theoretical expected; $n = 2$ for two dimensions and $n = 3$ for three dimensions. These values correspond to a transformation with a constant interface-controlled growth and preexisting nuclei. As the transformation proceeds and the growth becomes diffusion-controlled, the Avrami exponents tends to reach the values of 1 and 1.5 for two and three dimensions, respectively. The low $n$ values obtained experimentally in the devitrification of glassy metals are not reproduced by the simulations.

Depending on the supersaturation value, the degree of agreement between the *geometrical* and *mean-field* models and the simulations is slightly different. In figures 3.14 and 3.15, the transformed fraction evolution for systems with $S = 0.2$ and $S = 0.8$ respectively, are shown. The *mean-field* model underestimates the growth for $S = 0.8$, overestimates it for $S = 0.2$ and, as stated before,

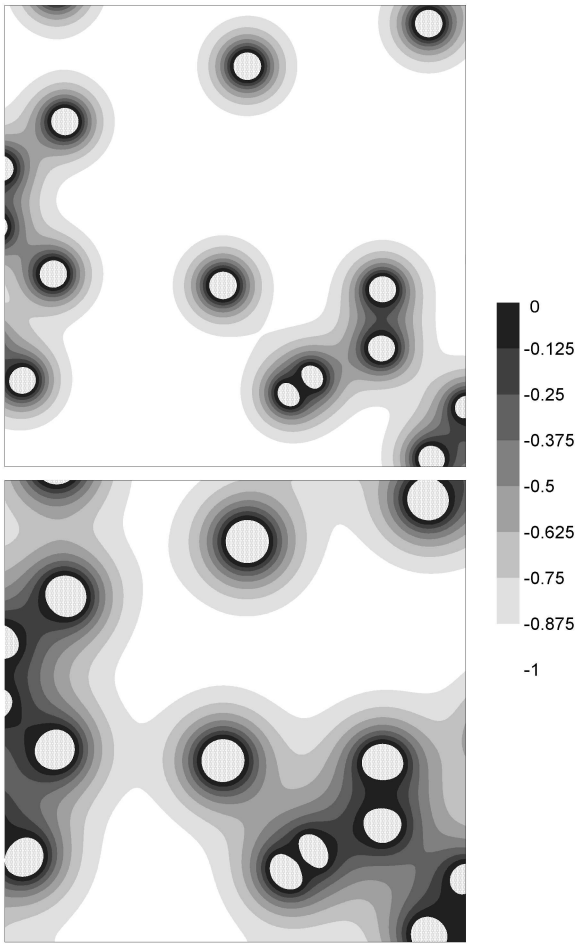


Figure 3.11: Partial view of a $2D$ simulation with preexisting nuclei at two different stages of the transformation ($x = 0.06$ in the upper figure and $x = 0.1$ in the lower). The gray gradient corresponds to the concentration (0 states for $c = c_l$ and $-1$ for $c = c_0$), whereas the dotted regions represent the crystallized phase.

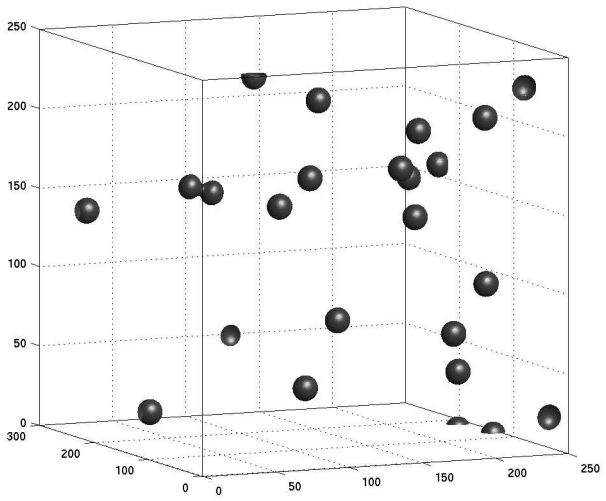


Figure 3.12: Partial view of a $3D$ simulation with preexisting nuclei at an early stage of the transformation. The black spheres correspond to the transformed phase.

describes with accuracy the simulation results for $S = 0.5$. On the contrary, the *geometrical* model perfectly reproduces the growth for $S = 0.8$ and $0.5$ while overestimates it for the lowest value of $S$, but not so much as the *mean-field* model. This behavior can be understood in terms of the concentration gradients surrounding the growing grains. High $S$ values imply high and short concentration gradients and so concentration profiles extend over a small volume fraction making the impingement between grains nearly equivalent to a direct impingement. On the contrary, with low $S$ values the impingement begins when the distance between neighboring grains is long respect to the grain radius, increasing the importance of the SI effect on the overall kinetics. It is worth to note that the *geometrical* model gives a good description of the simulation results for medium and high $S$ values, i.e., when the interaction between grains is more close to a direct impingement, one of the hypotesis of the KJMA equation. However, the *mean-field* model is only able to reproduce the simulated transformed fraction for medium values of the supersaturation. That can be explained again in terms of the concentration profiles. For high supersaturations, the mean concentration of the remaining amorphous precursor overestimate the interference between the concentration profiles of the grains because in that case the gradients are localized in a narrow area surrounding the grain and then, most of the amorphous phase remains with the initial concentration. That overestimation is translated into a slowing down of the kinetics with respect to the simulations as can be seen in figure 3.15. On the contrary, for low supersaturations the *mean-field* model underestimates the interaction between the grains, and hence,

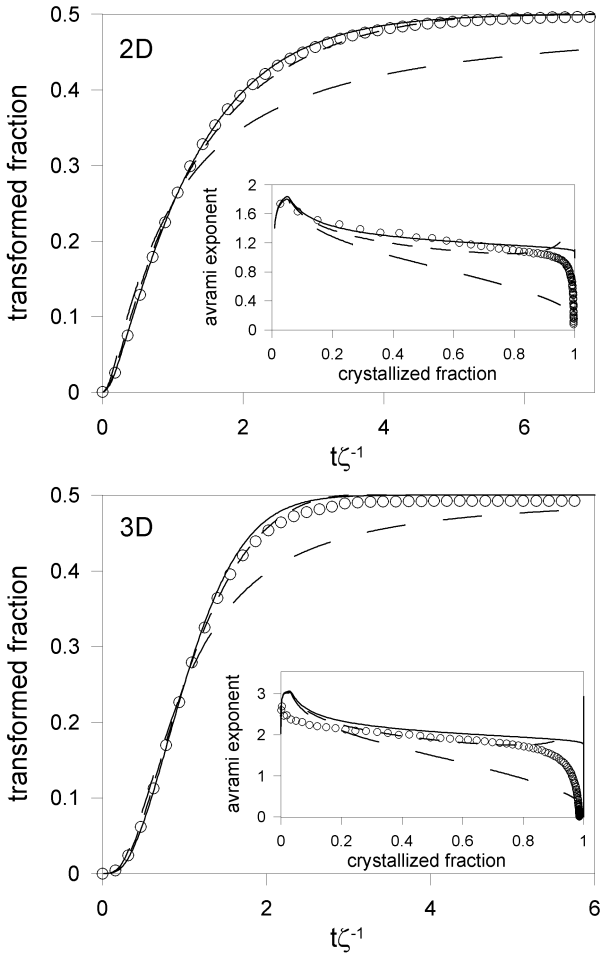


Figure 3.13: Transformed fraction and Avrami exponents for transformations with $S = 0.5$ and preexisting nucleation. Symbols: phase-field model simulation; solid line: *geometrical* model; dashed line: *mean-field* model; long-dashed line: *geometrica+mean-field* model.

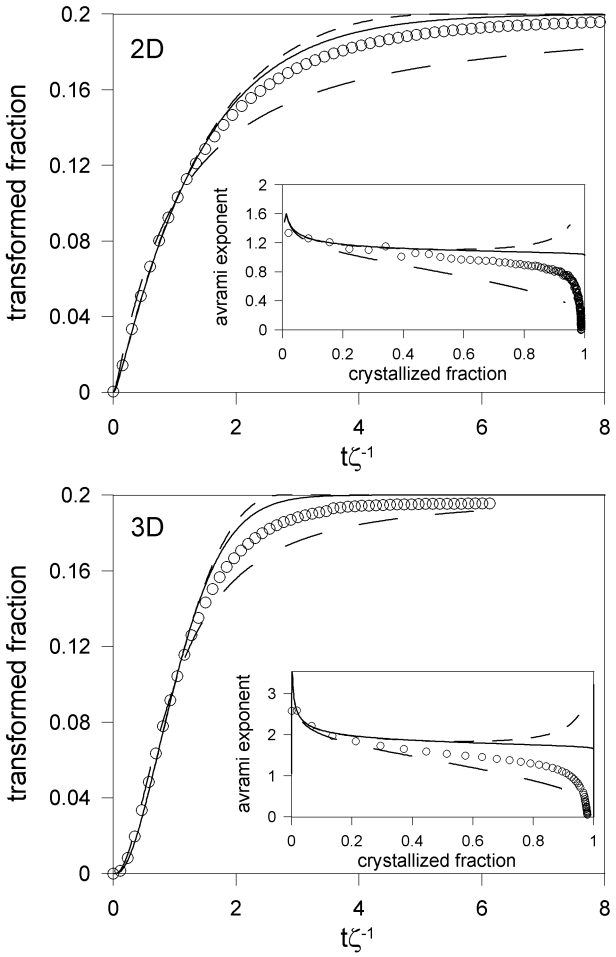


Figure 3.14: Transformed fraction and Avrami exponents for transformations with $S = 0.2$ and preexisting nucleation. Symbols: phase-field model simulation; solid line: *geometrical* model; dashed line: *mean-field* model; long-dashed line: *geometrica+mean-field* model.

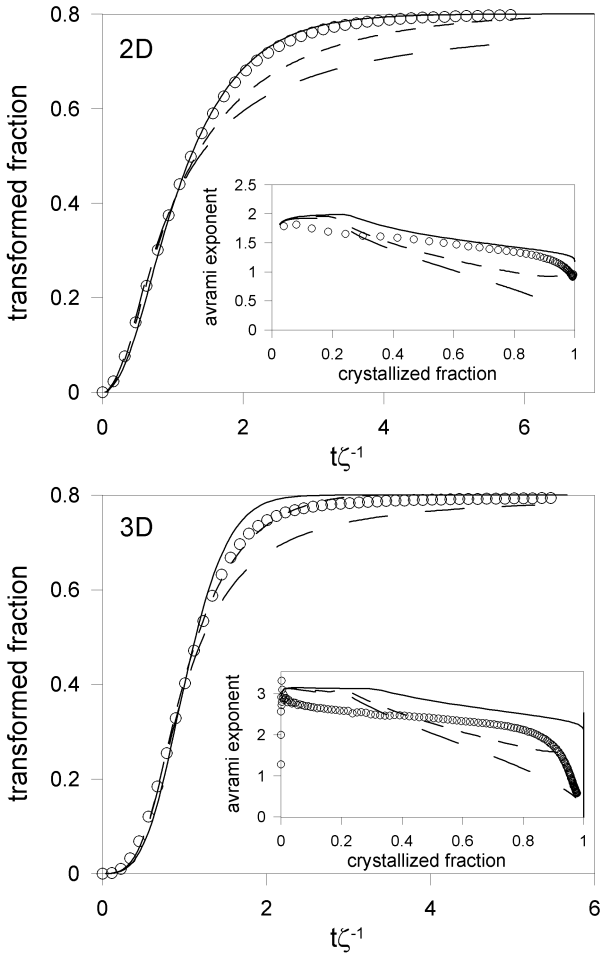


Figure 3.15: Transformed fraction and Avrami exponents for transformations with $S = 0.8$ and preexisting nucleation. Symbols: phase-field model simulation; solid line: *geometrical* model; dashed line: *mean-field* model; long-dashed line: *geometrica+mean-field* model.

the soft-impingement effect, resulting in a faster kinetics (see figure 3.14). This underestimation is due to the randomness of the preexisting nuclei that results in an inhomogeneous system, thus the mean-field approach is able to describe the concentration field between well-separated grains but not in the region between close grains where the SI effect is much more pronounced. For medium values of the supersaturation with not too long or too small concentration profiles, the details of the system are smoothered and the *mean-field* model is able to well reproduce the simulation results as can be seen in figure 3.13. In the $S = 0.8$ case, it can be seen a significant difference between the Avrami exponents obtained from the PFM simulations and from the models (see figure 3.15). This difference, that is more important at the beginning of the transformation is due to the fact that with high supersaturations the transient stage in which the grains grow by interface is larger. And, as explained before, this transient is not well modelled, thus yielding that behaviour of the Avrami exponents. But in any case, it can be seen that once the diffusion-controlled stage begins, the *geometrical* model curve is parallel to the simulation results, i.e. the behavior of the simulation is better reproduced by the *geometrical* model than by the *geometrical+mean field* model.

Having in mind that the *geometrical* model is in fact the KJMA model normalized by the final crystallized fraction, these results shows that the classical KJMA equation is able to describe the kinetics of the simulations (performed with a constant diffusion coefficient) and thus, can be used for the evaluation of the growth and nucleation rates, becoming a good first order approach describing the interference between growing particles even in the case of soft impingement. At the same time, the delay of the transformation kinetics and the corresponding low Avrami exponent experimentally observed in primary crystallization (and in this work represented by the *geometrical+mean-field* model) should not be attributed to the soft-impingement effect.

## 3.4 Transformations with continuous nucleation

Simulation results obtained with a constant nucleation will be compared again with the same kinetic models of the previous section. This constant nucleation is also know as non-random nucleation because, as the transformation proceeds, the matrix surrounding the growing crystallites become more stable, thus in these areas the nucleation is inhibited in comparison with areas of the matrix still with the initial concentration. This kind of nucleation protocol is not expected to introduce a significant modification on primary transformation kinetics. The non-random nucleation (NRN) effect was previously studied in detail by means of stochastic simulations [57]. In this reference, it was demonstrated that the effect on the overall kinetics is of second order compared to the effect of the growth-rate reduction due to diffusion controlled growth and soft-impingement. It was shown that the NRN modifies significantly the transformation kinetics only in systems with nucleation inhibition over an extremely wide area surrounding the particles, and in such cases, the whole system could

| | $\Delta x = 0.005$ | | $\Delta x = 0.0025$ | |
|---|---|---|---|---|
| | $S_L$ | $n$ | $S_L$ | $n$ |
| $2D$ | $\geq 0.065$ | 4 | $\geq 0.11$ | 4 |
| | $< 0.065$ | 16 | $< 0.11$ | 16 |
| $3D$ | $\geq 0.2$ | 8 | $\geq 0.4$ | 8 |
| | $[0.055, 0.2)$ | 64 | $[0.09, 0.4)$ | 64 |
| | $< 0.055$ | 216 | $< 0.09$ | 216 |

Table 3.4: Mininum number of cells of the initial radius needed to have a grain with a radii bigger than the critical one

be considered very close to a preexisting nuclei transformation, that is with no further nucleation after a short initial stage.

## Nucleation protocol

In the simulations, the NRN has been introduced in the following way. First of all, a particular cell has been chosen randomly and the nucleation probability in that cell has been calculated. This probability is directly proportional to the nucleation frequency that depends on the concentration of the cell (equation (1.6)). In terms of the dimensionless concentration ($u$) and the supersaturation ($S$), the nucleation probability can be written as:

$$I(u) = I_0 \exp\left\{-Q\left[\frac{1}{\ln^2(1+Su)} - \frac{1}{\ln^2(1-S)}\right]\right\} \tag{3.20}$$

In order to avoid nucleation in an existing grain, this probability is only computed if the selected cell has $\phi > 0.5$. The nucleation probability at $u = -1$, the composition of the untransformed matrix is $I_0$. Finally, if the probability is bigger than a certain random number, a nucleation event takes places and the $\phi$ and $u$ values are set to 0, the value that corresponds to the crystalline phase, in $n$ cells. The nucleation frequency is controlled through the number of times that an attempt of nucleation is performed, that in all the simulations is done every five time steps.

In contrast to the preexisting case, as the nucleation is possible along all the transformation, the local value of the supersaturation ($S_L = uS$) is different in different areas of the matrix and at different times. Then, in order to assure that all the nucleation events are real, i.e. that the new grain has an initial radius greater than the critical one and does not dissolve, the local supersaturation in the randomly selected cell is used to know the number of cells that the initial nuclei must occupy. The initial radii depends on the used spatial discretization (equations (3.18) and (3.19)), hence the initial number of cells that must be transformed is different for the case $S = 0.8$. The minimum numbers of cells needed to have a viable grain in each case can be seen in table 3.4.

| | $S$ | $Q$ |
|---|---|---|
| $2D$ | 0.2 | 0.0139 |
| | 0.5 | 0.0905 |
| | 0.8 | 0.2500 |
| $3D$ | 0.2 | 0.0155 |
| | 0.5 | 0.0971 |
| | 0.8 | 0.2641 |

Table 3.5: $Q$ values as a function of the supersaturation and the dimensionality. These values assure the same number of nucleation events in a Zener and in a steplike profile.

The parameter $Q$ that appears in equation (3.20) determines the relative size between the particles and the corresponding nucleation inhibited zone surrounding them; a lower $Q$ value implies a smaller region where the nucleation is reduced (recall figure 1.6). In the present work, the value of $Q$ is set in order that the number of nucleation events around an isolated precipitate particle with a Zener concentration profile (which are a good approximation to the profiles obtained by means of the simulation) coincides with the expected number for a steplike concentration profile, as it is considered in the *geometrical* model. With that choice, a comparison between simulations and the theoretical models can be established. To calculate the $Q$ value, the following condition must be fulfilled:

$$\int_R^\infty [1 - P(u)]\, 2\pi r\, dr \quad = \quad \pi \left[(R+\delta)^2 - R^2\right] \tag{3.21}$$

in the $2D$ case and the equivalent one for $3D$:

$$\int_R^\infty [1 - P(u)]\, 4\pi r^2\, dr = \frac{4\pi}{3} \left[(R+\delta)^3 - R^3\right] \tag{3.22}$$

A Zener's profile has been used in the $u(r)$ dependence that appears in $P(u)$, as well as the equation (3.2) and its equivalent for $2D$ ($(R+\delta)^2 = RS^{-1/2}$). The obtained values for each dimensionality and supersaturation can be seen in table 3.5. As an example, figure 3.16 shows the nucleation probability for a $3D$ case with $S = 0.5$, where it can be seen that at a distance approximately equal to two time the radius of a particle, the effect of stabilization of the matrix is negligible.

## Results

In general, similar results to the preexisting nucleation simulations are obtained with continuous nucleation. In figure 3.17, it can be seen how the *geometrical* and the *mean-field* models reproduce with accuracy the PFM results for the case $S = 0.5$, never yielding the expected slower kinetics or the low values

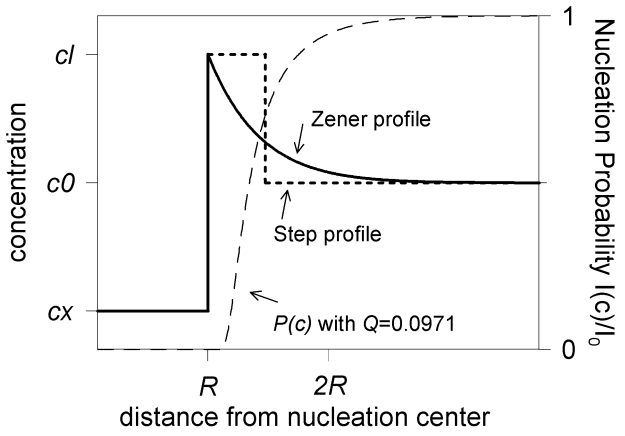


Figure 3.16: Nucleation probability in $3D$ for $S = 0.5$ and $Q = 0.0971$ as a function of the distance from the nucleation center.

of the Avrami exponents. Figures 3.18-3.19 show the results obtained in two- and three-dimensional systems for the other cases, $S = 0.2$ and 0.8. From the inset figures, it could be observed how the Avrami exponents evolve from 3 to 2 and from 4 to 2.5 in two and three dimensions, respectively and for all the studied cases. This corresponds to the change in the growth mechanism from constant interface controlled to diffusion controlled. Again, the Avrami exponent does not reach the low experimental values usually obtained and also given by the *geometrical+mean-field* model. An exception is the case $S = 0.2$ in which it can be observed a diminution of the Avrami exponents at the end of the transformation. On the contrary, the two first order approaches describe well the SI and NRN effect modeled in the simulations.

As can be seen in the figures and in contrast to the preexisting case, the *geometrical* model does not yield better results as the supersaturation increases. In all the studied cases it overestimates the simulated curves in the second part of the transformation, i.e. for $x(t) > S/2$. In contrast, the *geometrical+mean-field* model always yields a slower kinetics than the predicted by the phase-field model. In the case $S = 0.2$, the *mean-field* and the *geometrical* model are very similar and in the three-dimensional case the two models are indistinguishable (see figure 3.18), while as the supersaturation increases the *mean-field* model is able to predict with accuracy the transformed fraction, specially in the two-dimensional case for $S = 0.5$ (figure 3.17) and in any dimension for $S = 0.8$ (figure 3.19). Summarizing, these results show that in the case of continuos nucleation, the *mean field* model is a better approximation than the classical KJMA equation normalized by the final crystallization fraction (i.e., the *geometrical* model).

Figure 3.20 shows the particle density evolution $N(t)$ obtained in the three dimensional simulations and calculated by the kinetic models. The density of

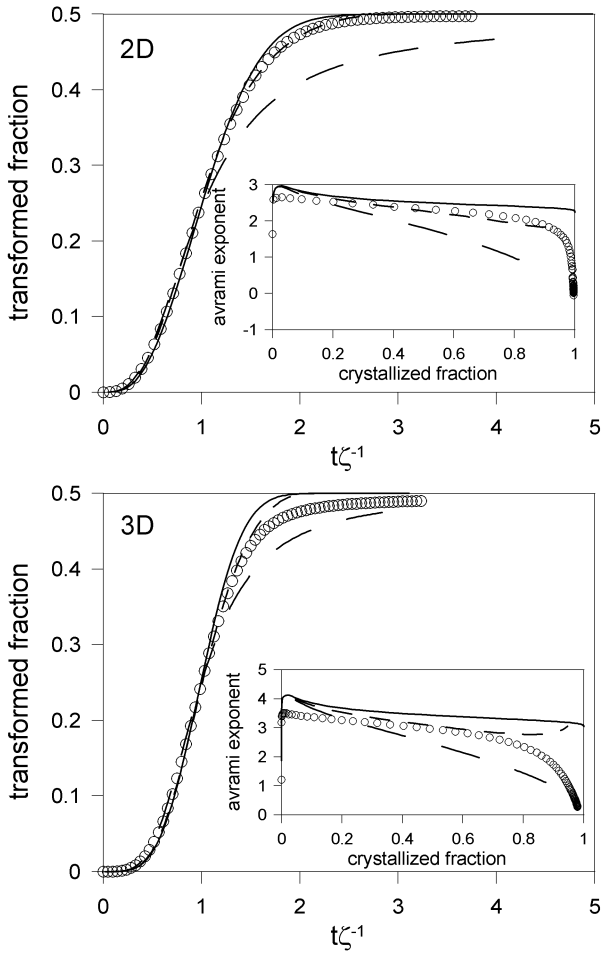


Figure 3.17: Transformed fraction and Avrami exponents for transformations with continuous nucleation and $S = 0.5$ in $2D$ and $3D$. Symbols: phase-field simulation; solid line: *geometrical* model; dashed line: *mean-field* model; and long dashed line: *geometrical+mean-field* model.

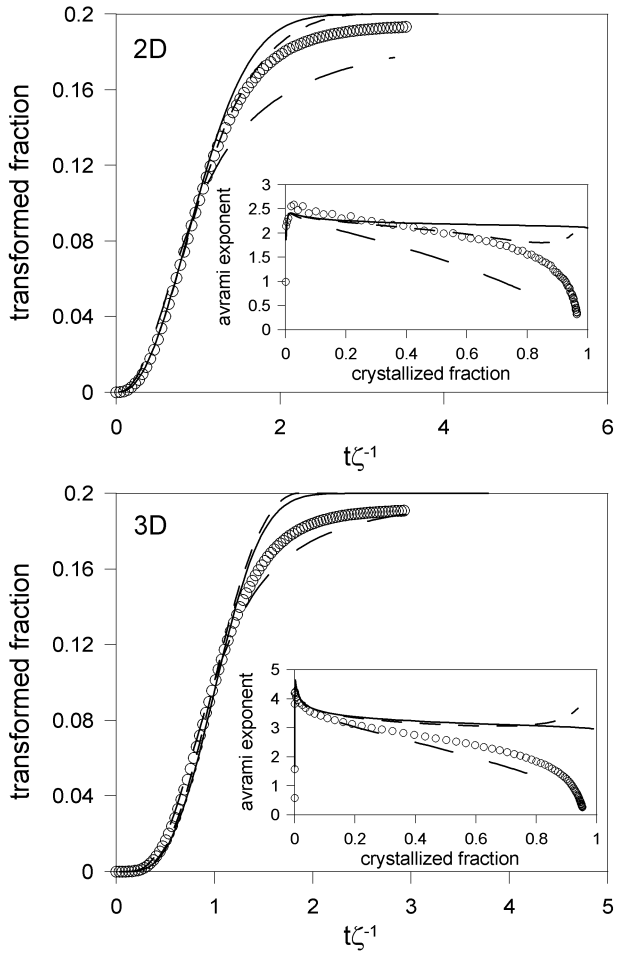


Figure 3.18: Transformed fraction and Avrami exponents for transformations with continuous nucleation and $S = 0.2$ in $2D$ and $3D$. Symbols: phase-field simulation; solid line: *geometrical* model; dashed line: *mean-field* model; and long dashed line: *geometrical+mean-field* model.

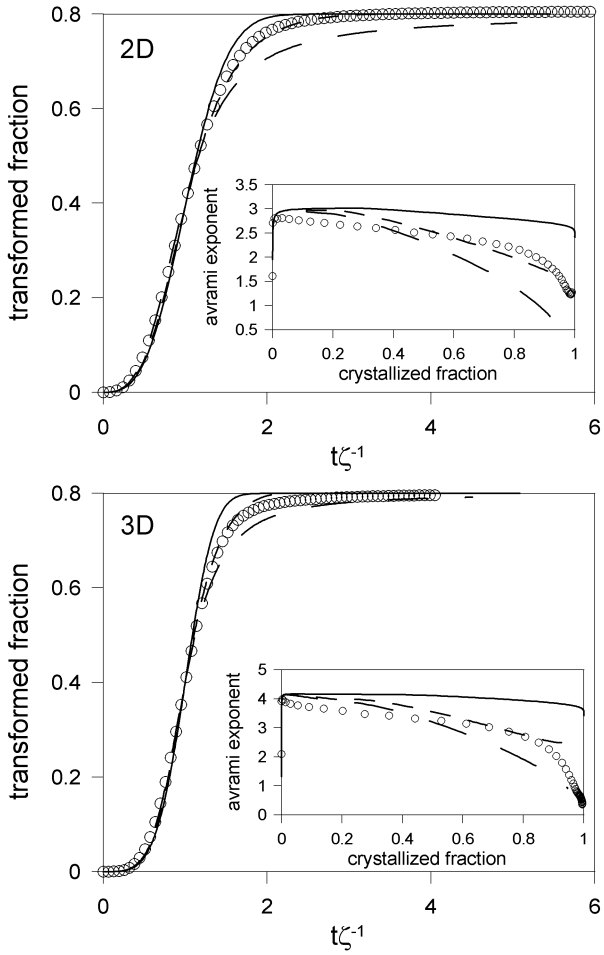


Figure 3.19: Transformed fraction and Avrami exponents for transformations with continuous nucleation and $S = 0.8$ in $2D$ and $3D$. Symbols: phase-field simulation; solid line: *geometrical* model; dashed line: *mean-field* model; and long dashed line: *geometrical+mean-field* model.

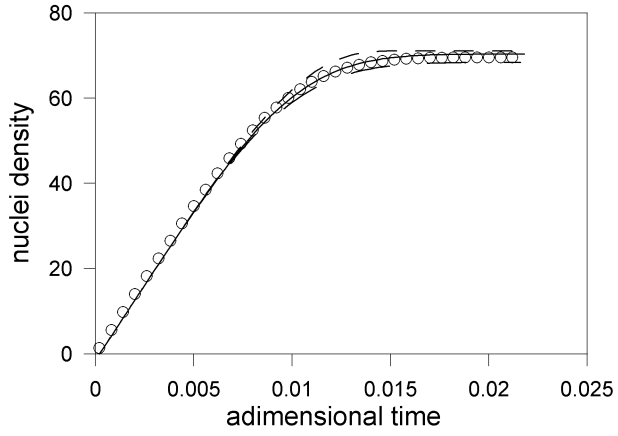


Figure 3.20: Particle density evolution. Symbols:phase-field simulation; solid line: *geometrical* model; dashed line: *mean-field* model; and long dashed line: *geometrical+mean-field* model.

particles per unit time throughout the transformation is given by:

$$\frac{dN}{dt}_{g} = I(c_0)[1 - x_{TB}(t)] = I_0[1 - S^{-1}x(t)]$$

and

$$\frac{dN}{dt}_{mf} = I[c_m(t)][1 - x(t)]$$

for the *geometrical* model and the *mean-field* model, respectively. In the first case the nucleation frequency is constant but only allowed in the nonstabilized zone of the matrix. In the second case nucleation is allowed in all the untransformed volume but the nucleation frequency is progressively reduced as the mean concentration varies in the matrix. $c_m(t)$ is calculated by means of equation (1.24). Similar to results obtained for $x(t)$ and the Avrami exponents both models give a good agreement with the phase-field simulation. Here it must be remarked that the $Q$ value was chosen to provoke an overall nucleation inhibition equal to that given in the geometrical model. Different values of $Q$ would imply a nucleation inhibition distance different from the thicness $\delta$ of the stabilized boundary zone, thus invalidating, in principle, the use of the simple geometric model described here. On the other hand, the agreement given by the *mean-field* model is not expected to change in case parameter $Q$ was modified. Two-dimensional simulations of a system with continuous nucleation, $S = 0.5$ and different values for the $Q$ parameter has been performed in order to check the effect of this parameter. In figure 3.21 it can be seen that, as expected, a

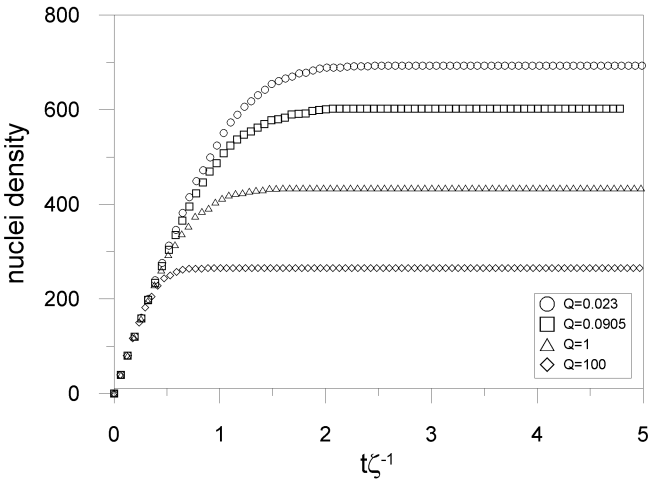


Figure 3.21: Nulcei density as a function of the $Q$ parameter for $2D$ simulations with $S = 0.5$ and continuous nucleation. $Q = 0.0905$ is the value chosen for this system through all this work.

higher value of $Q$ reduces the nucleation density because the size of the nucleation inhibited area is larger. This reduction can be as high as a 50%, but the effect on the transformed fraction is not significant. As shown in figure 3.22, only for very large values of $Q$ (around 100) a small reduction in the kinetics can be observed at the end of the transformation. A $Q$ value of 100 implies that the nucleation probability is different from 0 only in those areas where the matrix concentration is still the initial one $c_0$. Therefore, the $Q$ parameter is not critical, and the criterium used for calculating has more theoretical implications than practical.

### Conclusions

In this chapter, primary crystallization kinetics has been analyzed by means of phase-field model simulations that naturally reproduce the effects of soft-impingement and a concentration dependent nucleation rate. Usually, these mechanisms were meant to cause the complex kinetics commonly observed in primary crystallization. However, the results presented above show that the classical KJMA model is able to describe the kinetics of the simulations with a preexisting nucleation protocol while a mean-field model describes better the simulations with continuous nucleation. The Avrami exponent mantains its meaning, that is, at each instant of the transformation its value gives information about the growth mechanism and the nucleation law. Moreover, the two models presented at the beginning of the chapter can be used for the evaluation of the growth and nucleation rates, becoming a good first order approach describing

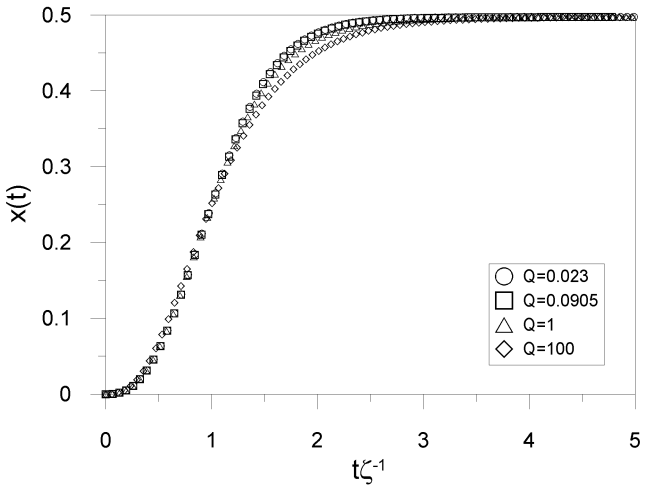


Figure 3.22: Transformed fraction evolution as a function of the $Q$ parameter for $2D$ simulations with $S = 0.5$ and continuous nucleation. $Q = 0.0905$ is the value chosen for this system through all this work.

the interference between growing particles in the case of soft impingement and continuous nucleation.

These results suggest that the delay of the transformation kinetics and the corresponding low Avrami exponent experimentally observed in primary crystallization should not be attributed to the soft-impingement effect or to the non-random nucleation. Additional mechanisms have to be considered in order to explain the slowing down of the kinetics as the transformed matrix becomes progressively stabilized. Next chapter will be devoted to the study of the effect of the local change in the atomic transport properties of the amorphous matrix due to the compositional changes produced in a primary crystallization.

# Chapter 4

# Simulations with a compositional dependent $D$

In the previous section, it was shown that the kinetics of primary crystallization can not be explained by the soft-impingement effect or the non-random nucleation. In the present chapter, a compositional dependence of the diffusion coefficient will be considered and added in the phase-field simulations. First of all, a justification of that dependence will be presented on the basis of the viscosity variation with temperature that is extremely sensitive near the glass transition temperature. Finally, and analogously to the previous chapter, transformations with preexisting and non-random nucleation will be considered and, with the help of simulations of a single isolated particle, compared with the theoretical models.

## 4.1 Relationship between diffusion coefficient and viscosity

As explained at the end of the Introduction (section 1.3), near the glass transition temperature there is a drop of about one order of magnitude in the diffusivity of metallic glasses. That fact with the results of the last chapter induce to think that the kinetics of primary crystallization in metallic glasses is affected by local variations of the diffusion coefficient. In this section a relation between the viscosity and the diffusivity will be presented in the framework of the free-volume theory of metallic glasses and it will be shown that viscosity can be compositional dependent, thus justifying the introduction of a locally varying diffusion coefficient.

**Free volume theory:**

The free volume theory of metallic glasses describes the atomic mobility in terms of defects [103, 104, 105] and the diffusion takes place as a redistribution of the

free volume in the glass. Thus, the fluidity will be directly proportional to the probability of an atom to find free volume in its surroundings, that is, to the concentration of "flow defects", $c_f$ [26]. This concentration can be derived assuming that: *(a)* atomic transport may only occur when voids having a volume greater than some critical value $v^*$ form by redistribution of the free volume, and *(b)* no energy is required for free volume redistribution. Then, $c_f$ is given by:

$$c_f = \exp(-\gamma v^*/v_f) \tag{4.1}$$

where $v_f$ is the average free volume per atom and $\gamma$ is an overlap factor of the order of 0.5. Accordingly, the viscosity of a metallic glass will be inversely proportional to $c_f$:

$$\eta \sim c_f^{-1} \tag{4.2}$$

Compared with the fluidity, the diffusion coefficient is proportional to the concentration $c_d$ of "diffusion deffects":

$$D = D_0^{'} c_d \exp(-H/k_B T) \tag{4.3}$$

where, as explained in section 1.3, $H$ is the activation enthalpy for diffusion, $k_B$ is the Boltzmann constant and $T$ is the temperature.

Classically, the relation between the viscosity and the diffusivity is given by the Stokes-Einstein relation, that at constant temperature is:

$$\eta D = constant \tag{4.4}$$

This implies that the concentration of "diffusion defects" $c_d$ is linearly proportional to the concentration of flow defects ($c_d = K c_f$ where $K$ is a constant). But in recent years, it has been demonstrated that the Stokes-Einstein relationship does not hold in glasses [106, 107, 108]. Instead, a modfication of this relation

$$\eta D^2 = constant \tag{4.5}$$

fitts better the experimental data. Thus, the relation between $c_d$ and $c_f$ is not anymore lineal but quadratic: $c_d = K c_f^{1/2}$. Thus, equation (4.3) can be written as:

$$D = D_0^{'} K c_f^{1/2} \exp(-H/k_B T) = \eta^{-1/2} K^{'} \exp(-H/k_B T) \tag{4.6}$$

At this point, we can proceed in two ways: *(a)* following Cohen and Grest [109], when the metallic glass is in thermal equilibrium, $v_f$ can be approximated by a linear relation around the glass transition temperature:

$$v_f = \gamma v^* \frac{T - T_0}{B_0} \tag{4.7}$$

with $B_0$ and $T_0$ constants; *(b)* describing the viscosity of metallic glasses with a VTF equation (see figure 4.1) :

$$\eta = \eta_0 \exp(\frac{B_0}{T - T_0}) \tag{4.8}$$

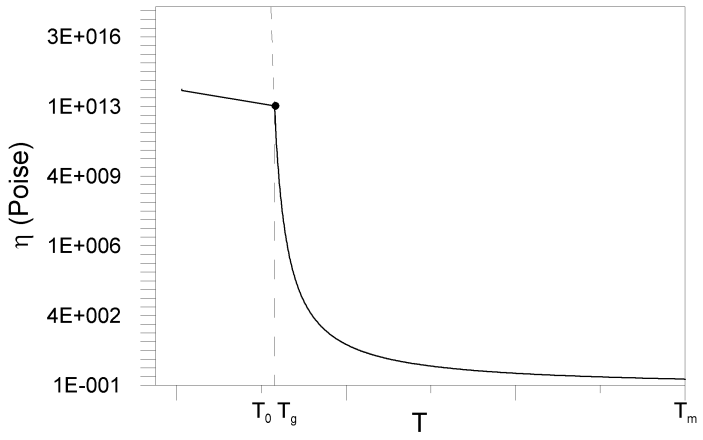


Figure 4.1: Viscosity of a supercooled liquid as function of the temperature showing that $T_g$ is always greater than $T_0$. As the glass transition takes place, the viscosity of the corresponding glass remains finite at a value that depends on the cooling rate.

In both cases the diffusion coefficient can be expresed as (equations (4.6) and (4.7) or (4.8)):

$$D = K^{'} \exp(-H/k_B T) \exp(-\frac{B_0}{T - T_0}) \tag{4.9}$$

Followingly, it will be shown that $T_0$ and $B_0$, the temperature at which the viscosity is predicted to be infinity, depends on the concentration and thus the dependence of $D$ on the local concentration will be justified.

**Composition dependent diffusion coefficient:**

Compositional changes of the amorphous matrix as the primary crystallization proceed can induce changes in the glass transition temperature that in turn, induce changes in the viscosity of the matrix. Thus, it is also expected to observe changes in the diffusion coefficient.

There are several experimental observations that show how $T_g$ depends on the composition of the metallic glass. In [110] the authors show how $T_g$ changes as a certain amount of Ni is substituted by Cu in $Zr_{67}(Ni_{1-x}Cu_x)$ metallic glass. Molecular dynamics simulations also predicts variations of $T_0$ as the concentration of Pd increases in a undercooled Pd-Ni alloy [111]. Another common feature in primary crystallization is the decomposition of the residual amorphous phase. Several exemples can be named: in the $Fe_{65}Nb_{10}B_{25}$ system the nanometer size particles coexist with a complex Nb-enriched disordered phase and a remaining Nb-poor disordered phase [112]; in $Zr_{41.25}Ti_{13.75}Ni_{10}Cu_{12.5}Be_{22.5}$ bulk metallic glass, accompanying precipitation of quasicrystalline phase the composition

of the residual amorphous phase change and become inhomogeneous [113]; a different composition of the same kind of bulk metallic glass decompose in two phases, one rich in Be and the other rich in Ti, being the Be-richest glass the one with a more rigid structure and thus where the diffusion is more slower [114]. Therefore, it is reasonable to suppose that the glass transition temperature changes as the primary crystallization proceeds due to changes in the viscosity produced by the changes in the local structure of the amorphous matrix. Thus, the compositional inhomogenity of the amorphous phase that results from a primary crystallization lead to changes in the atomic transport properties, i.e., in the diffusion coefficient that becomes compositional dependent.

The main hypothesis that will be checked in the next sections by means of phase-field model simulations is that the diminution of the diffusion coefficient of the slowest species that controls the transformation is the responsible of the slowing down of the kinetics in a primary crystallization. This diminution arise from the local changes in the structure, that stabilize it and produce an increase of the viscosity that makes the diffusion more sluggish. It will be supposed that the crystallization temperature is above the glass transition temperature. Thus, a decreasing diffusion coefficient as the transformation proceeds has been implemented in the phase-field model.

In a first order approach and in order to check if this variable diffusion coefficient can really account for the kinetics observed in primary crystallization and the low Avrami exponents, a simple linear dependence was chosen [115]:

$$D(c) = \frac{(D_1 - D_0)}{S}(c - c_l) + D_1 \tag{4.10}$$

where $D_0$ and $D_1$ are the initial and final diffusion coefficients in the amorphous matrix. This dependence stands for a lower diffusion coefficient in the more stable zones of the amorphous matrix, in agreement with the higher viscosity expected in these zones. In figure 4.2 phase-field simulation with this diffusion coefficient is shown (with $D_0/D_1 = 0.5$)[1]. This simulation corresponds to the growth of $3D$ preexisting nuclei. Empty symbols are the evolution in that case while solid simbols represent the evolution with a constant diffusion coefficient (both with $S = 0.5$). For comparison the result of the *geometrical+mean-field* model is also shown. From this figure it can be seen that a reduction of the kinetics is obtained, confirming the assumption made that this varying $D(c)$ can be the responsible of the primary crystallization kinetics. Of course, quantitative comparison with experimental data would require a better model for $D(c)$. In fact, such behavior will depend strongly in several factors such as the gap between $T_g$ and the crystallization temperature, the effect of the matrix composition change on $T_g$, and the change in the transport properties of the different atomic species present in the particular alloy.

Followingly, a more realistic dependence has been considered. As shown in equation (4.9), the diffusion coefficient can be written with a $VTF$-like equation

[1] The implementation of this varying diffusion coefficient in the phase-field equations will be explained in the next section.

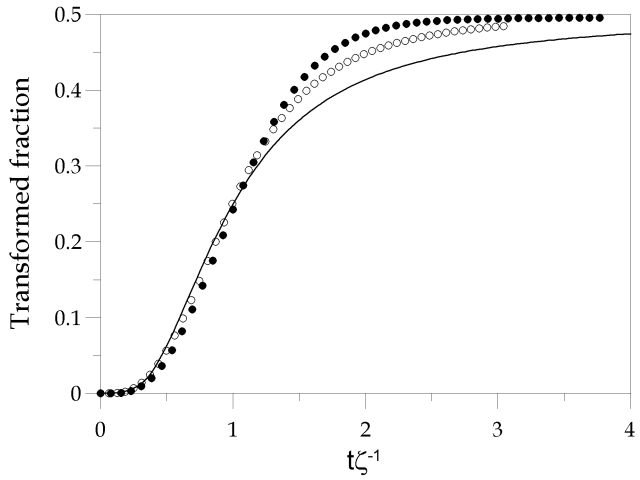


Figure 4.2: Phase-field model simulation with constant $D$ (solid symbols) and with $D(c)$ (empty symbols) compared with the *geometrical+mean-field* model (line).

that depends on $B_0$ and $T_0$ that can be compositional dependent. For the sake of simplicity, it will be assumed that this dependence is solely through $T_0$ and that is analogous to the dependence of the glass transition temperature on the composition. Thus, the diffusion coefficient can be written as:

$$D(c) = D^{'} \exp(-g(c)) \tag{4.11}$$

where $D^{'}$ is a constant in an isothermal process and the particular form of $g(c) = \frac{B_0}{T - T_0(c)}$ will depend on the particular metallic glass under study. To proceed further, the dependence of $T_0$ on $c$ must be stablished and in a first order approach it will be assumed linear. This assumption is backed, for example, by experimental data of $ZrNiCu$ metallic glasses (figure 1 from [110]) and $PdNi$ alloys (figure 10 from [111]) that show that for not too large compositional differences, $T_g$ depends linearly on $c$:

$$T_g = T_{g,0} + kc \tag{4.12}$$

with $k$ a constant.

A particular $g(c)$ will be presented in the next sections of this chapter, as well as the results of phase-field model simulations with this particular dependence.

## 4.2 Phase-field model with non-constant $D$

The phase-field model equations (2.22) and (2.23) presented in chapter 2 were derived assuming a constant diffusion coefficient and the dimensionless time was

obtained dividing by a reference length and $D$ (equation (2.21)). If we want to perform simulations with a varying diffusion coefficient, it is not possible to use $D$ to obtain the dimensionless time; instead of it, a reference diffusion coefficient $D_0$ will be needed. Thus, the new dimensionless time is $\widetilde{t} = t/(\omega^2/D_0)$. With this time and the same dimensionless space, the phase-field model equations for a non-constant $D$ are:

$$\frac{\varepsilon^2}{m'}\frac{\partial\phi}{\partial\tilde{t}} = \phi(1-\phi)[\phi - \frac{1}{2} + 30\varepsilon\alpha Su\phi(1-\phi)] + \varepsilon^2\tilde{\bigtriangledown}^2\phi \tag{4.13}$$

$$\frac{\partial u}{\partial\tilde{t}} + \frac{1}{S}(30\phi^2 - 60\phi^3 + 30\phi^4)\frac{\partial\phi}{\partial\tilde{t}} = \tilde{\bigtriangledown}(\frac{D(u)}{D_0}\tilde{\bigtriangledown}\tilde{u}) \tag{4.14}$$

where now $m^{'} = \frac{\mu\sigma}{D_0}$. In the simulations $\frac{D(u)}{D_0}$ has been set equal to a particular function of the dimensionless concentration ($f(u)$) that will be described later. Moreover, the structural changes that lead to a compositional dependent diffusion coefficient not only affect the diffusion-controlled growth but also the interface-controlled growth through the interface kinetic coefficient $m^{'}$ that will be proportional to this function of the concentration: $m^{'} = \mu\sigma f(u)$. In all the cases, $D_0$ is set equal to 1.

The functional dependence between $D$ and $u$ that has been choosen for this thesis is a decreasing exponential according to the assumptions made in the former section. The only condition that must fulfill this exponential is that $D$ must be equal to 1 (the value taken in the constant $D$ simulations) in the initial untransformed matrix, i.e., $D(-1) = 1$. With these requirements, the diffusion coefficient is written as:

$$D(u) = C_1 \exp(-C_2(u+1)) \tag{4.15}$$

where $C_1 = 1$ and $C_2 = 3$. The value of $C_2$ was choosen in order to obtain a variation of $D$ between $u \in [-1, 0]$ neither too soft nor too strong (figure 4.3). Moreover, this value can be used to estimate the value of $k$ and compare it with the experimental variations of $T_g$ with composition. To do that, equations (4.9) and (4.12) has been considered and values for the several constants have been taken from reference [26]. These values corresponds to the $Pd_{40}Ni_{40}P_{20}$ system and are:

$$B_0 = 7590K \qquad T = 565K \qquad T_0 = 355K$$

and it has been assumed that $T_0 = T_g/\Theta$ where $\Theta$ usually lies between $1.1 - 1.5$. With $\Theta = 1.3$, the remaining constant is set to $T_{g,0} = 462K$. With this set of constants, the $k$ value that reproduces the modelled behavior of $D(u)$ (equation (4.15)) ranges from 48 (for supersaturations of 0.8) to 105 (for $S = 0.2$) (figure 4.3). From the references [111] and [110], experimental values of $k$ can be calculated and they are of the order of 175 in the first case and 50 in the second reference. Thus, the value $C_2 = 3$ used in the simulations implies variations of $T_g$ with the composition of the same order of magnitude than the experimentally observed.

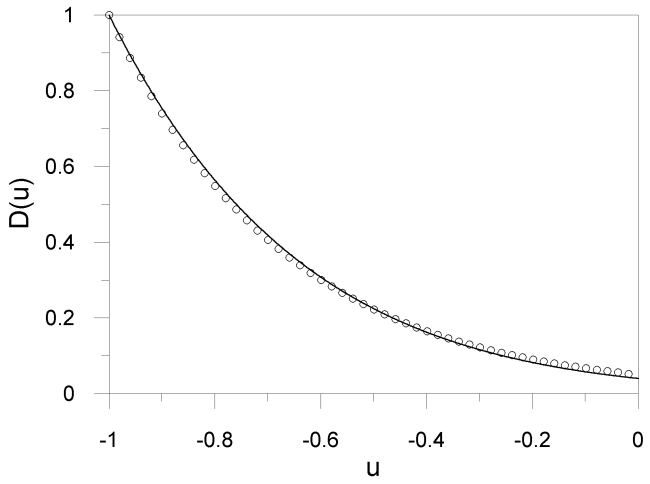


Figure 4.3: Modelled variation of $D$ (symbols) compared with the theoretical variation of $D$ from equation 4.15 with the constants evaluated from reference [26] and assuming $S = 0.5$.

## 4.3 Transformations with preexisting and continuous nucleation

### 4.3.1 Growth of a single particle

Simulations of one single particle with a constant diffusion coefficient allowed us to evaluate the parameter $\lambda$ of the Zener's equation and it was found that for high supersaturations this value departs from the theoretical one derived by Zener. In the present chapter the $\lambda$ values found in section 3.2 are used for analyzing the simulations with a non constant diffusion coefficient. In this case, equation (3.15) can not be used for describing the temporal evolution of the radius of an isolated particle because it does not take into account the variation of the diffusion coefficient. Thus, simulations of one single particle with a compositional dependent diffusion coefficient has been performed and compared to equation (3.15) but with an effective diffusion coefficient $\widetilde{D}$ to take into account its reduction from 1 at the beginning of the growth to values close to 0 at the end of the transformation. The $\widetilde{D}$ value will be obatined from the fitting of the simulated curve. This modified equation will be used to compute the theoretical models to compare with the N-particle simulations. This procedure is similar to the one performed in an actual primary crystallization, where from the calorimetric data an effective diffusion coefficient can be evaluated.

Two and three dimensional simulations of one single particle have been performed with the characteristics described in section 2.2. It is worth to remember here that in order to avoid numerical instabilities in the simulations, the inter-

| $S$ | $2D$ | $3D$ |
|---|---|---|
| 0.2 | 0.475 | 0.475 |
| 0.5 | 0.43 | 0.43 |
| 0.8 | 0.40 | 0.40 |

Table 4.1: Values of the effective diffusion coefficient in each dimension and for all the supersaturation values.

facial width $\varepsilon$ has to be reduced, in this case to the half. Thus, $\Delta x$ has to be also reduced to the half causing a diminution of the time step (equation (2.38)) and then, multiplying by $\sim 30$ the time needed for each simulation.

Three diferent supersaturations have been considered: 0.2, 0.5 and 0.8 and the temporal evolution of the radius has been obtained from the transformed fraction curves and equations (3.16) and (3.17), for two and three dimensions, respectively. Simulation results and the corresponding fitted curve can be seen in figure 4.4 for $2D$ and in figure 4.5 for $3D$. The effective diffusion coefficient evaluated from the fitting of these simulations are shown in table 4.1. The first comment that can be done is that no matters which is the dimensionality of the system, in any case $\widetilde{D}$ has the same value. What is important is the degree of supersaturation: high supersaturations imply a slightly higher reduction in the diffusion coefficient. That can be explained taking into account that in systems with low supersaturations, the equilibrium concentration in the interface between the crystalline and the amorphous phase is more quickly attained that in the case with high supersaturations. Then, it implies that the amount of redistributed solute is smaller and hence, the structural changes are also smaller affecting less the diffusion coefficient.

Looking to figures 4.4 and 4.5, the same observations that were made in the analysis of one single particle simulations with a constant $D$, can be done. That is, the effect of the transient stage is more important for high values of the supersaturation.

### 4.3.2 Transformations with preexisting nucleation

The used nucleation protocol is the same than in the constant $D$ case. The difference lies in the initial number of cells that must be set to the transformed value due to the change in the space discretitzation $\Delta x$. As a result, all the two-dimensional simulations have an initial radius with 4 cells and all the three-dimensional ones have 8 cells except for supersaturations of 0.2 in which case the minimum number of cells required to have an initial radii greater than the critical one is 64.

In figures 4.6-4.8 the results of the simulations with a non-constant diffusion coefficient and preexisting nucleation can be seen. The behaviour of the theoretical models has not change with respect the constant $D$ case because the possible variation in the atomic transport properties is not included in them. Hence, the

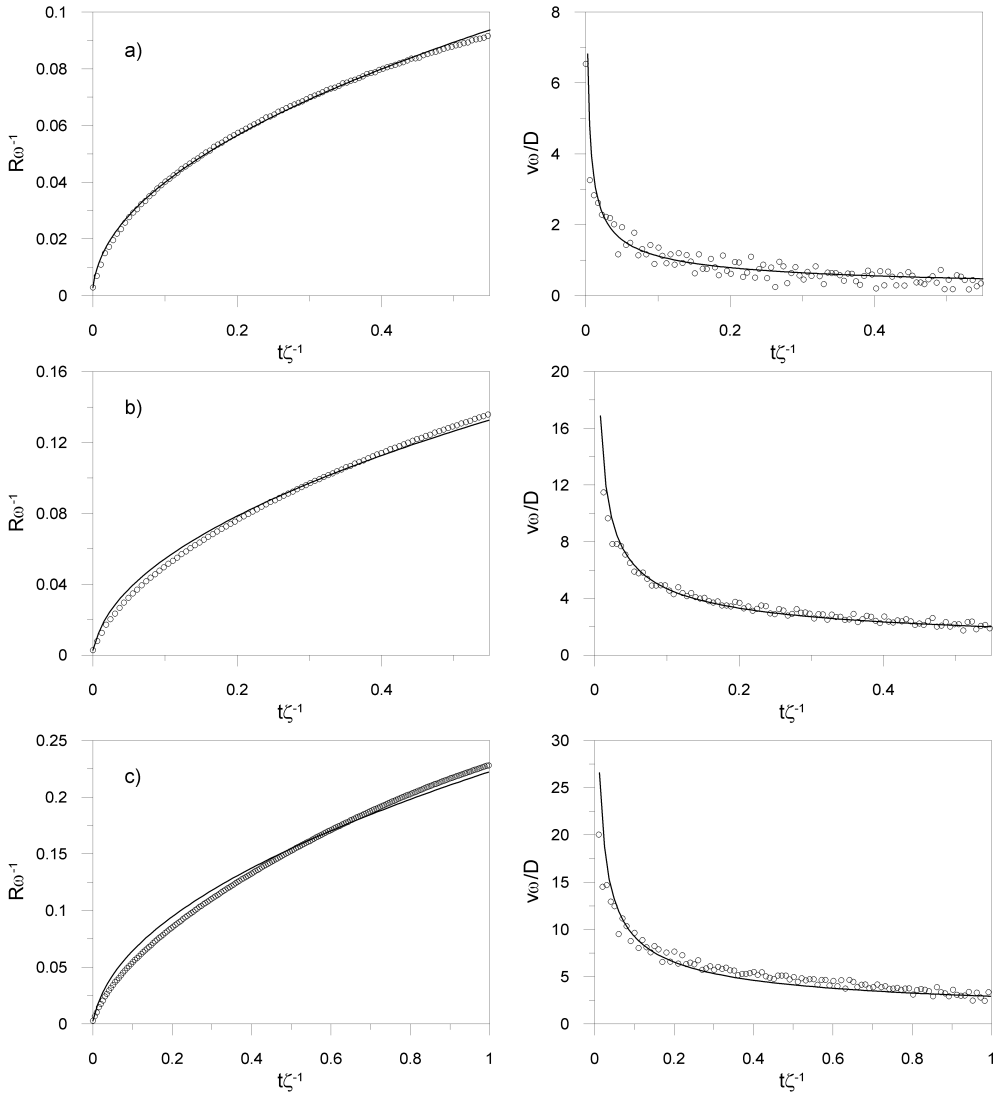


Figure 4.4: Dimensionless radius (left) and velocity (right) for one single particle in $2D$ with supersaturation values of: a) 0.2, b) 0.5 and c) 0.8. Symbols: simulation results; solid line: theoretical curve.

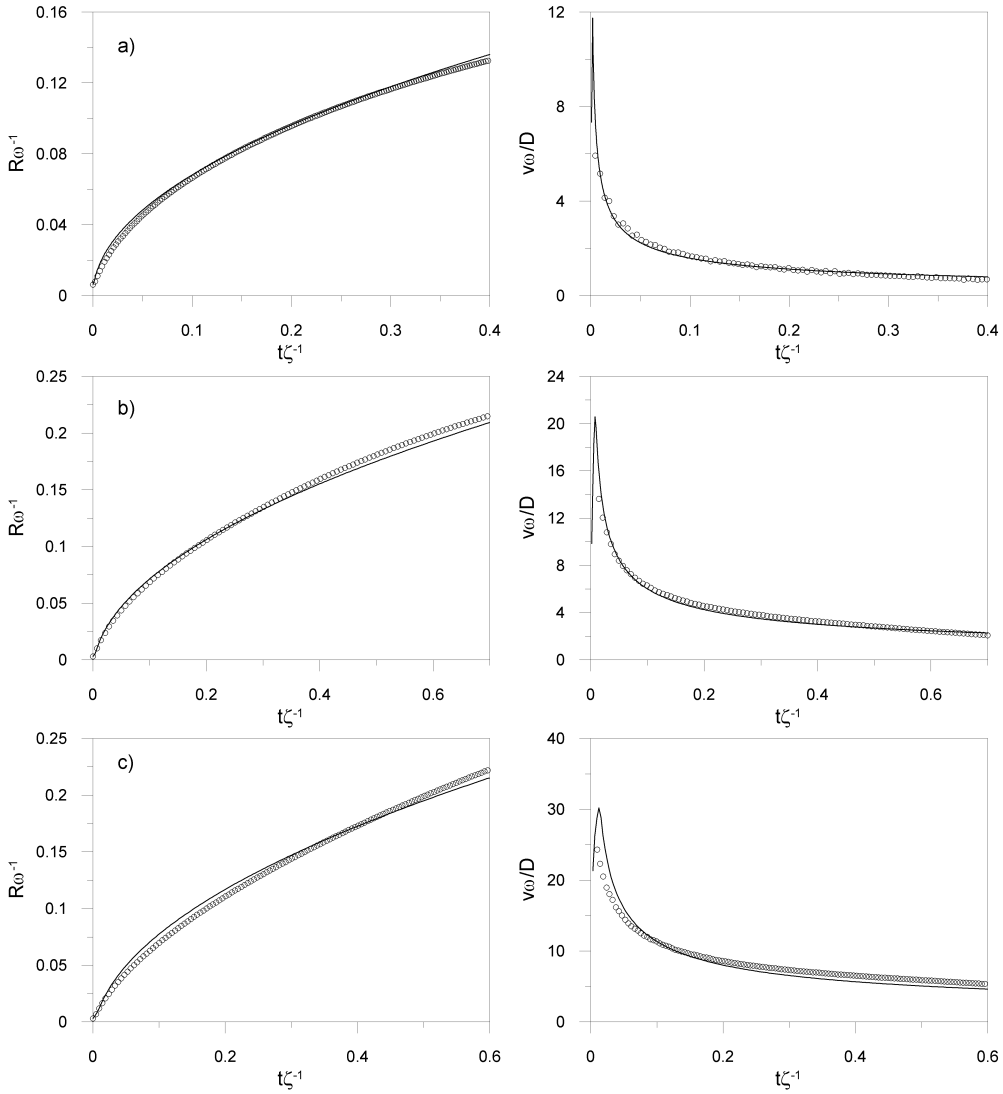


Figure 4.5: Dimensionless radius (left) and velocity (right) for one single particle in $3D$ with supersaturation values of: a) 0.2, b) 0.5 and c) 0.8. Symbols: simulation results; solid line: theoretical curve.

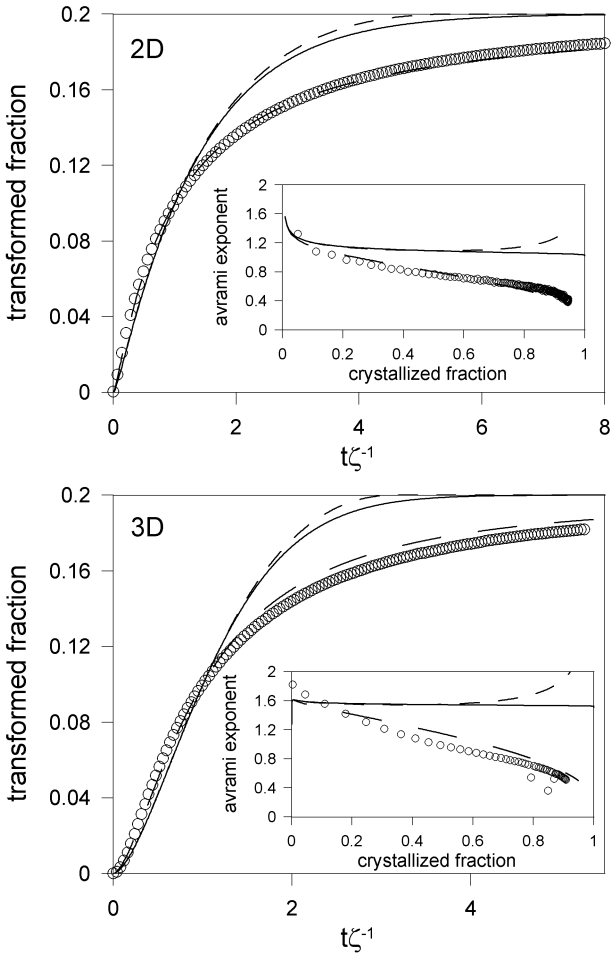


Figure 4.6: Transformed fraction and Avrami exponents for transformations with $S = 0.2$ and preexisting nucleation. Symbols: phase-field model simulation; solid line: *geometrical* model; dashed line: *mean-field* model; long-dashed line: *geometrica+mean-field* model.

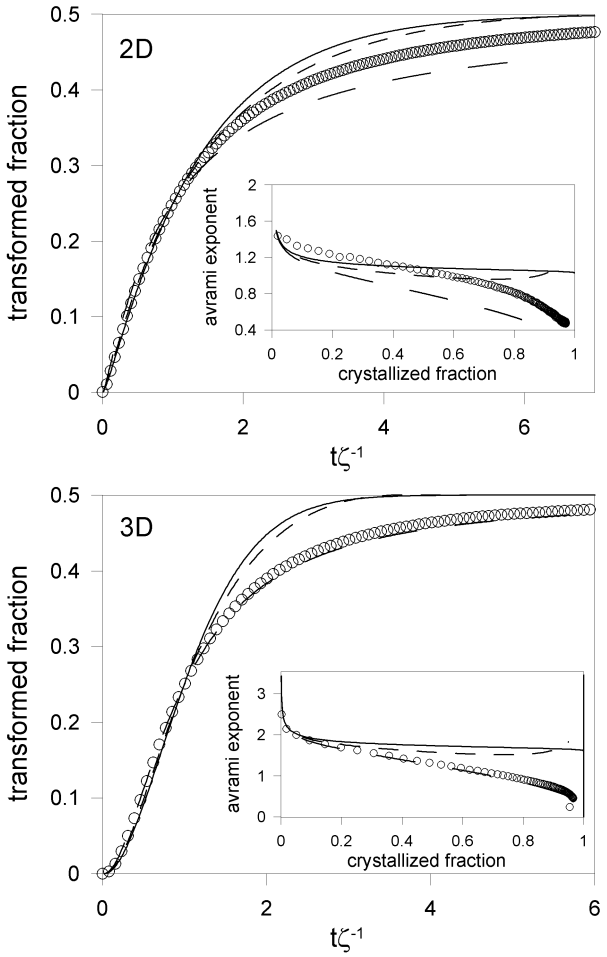


Figure 4.7: Transformed fraction and Avrami exponents for transformations with $S = 0.5$ and preexisting nucleation. Symbols: phase-field model simulation; solid line: *geometrical* model; dashed line: *mean-field* model; long-dashed line: *geometrica+mean-field* model.

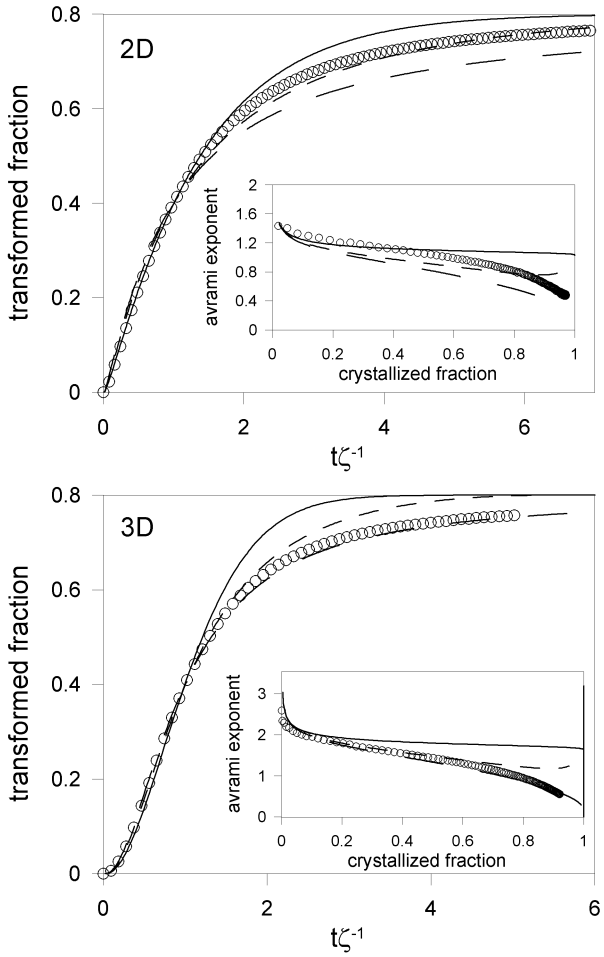


Figure 4.8: Transformed fraction and Avrami exponents for transformations with $S = 0.8$ and preexisting nucleation. Symbols: phase-field model simulation; solid line: *geometrical* model; dashed line: *mean-field* model; long-dashed line: *geometrica+mean-field* model.

same features described in the last chapter regarding the temporal evolution of the *geometrical* and the *mean-field* models can be equally observed in these figures. An important difference can be seen comparing the two-dimensional simulations with the three-dimensional ones. In $3D$ the concentration dependence introduced in the diffusion coefficient yields with an excellent agreement the kinetics expected in an actual primary crystallization, that is represented by the *geometrical+mean-field* model. And not only the kinetics but also the Avrami exponents obtained evolve from the theoretically expected values at the beginning of the transformation to values lower than 1 at the end, as it is observed in actual primary crystallization. The difference in the Avrami exponents behavior between the constant and the variable $D$ cases can be clearly seen in figure 4.9. The simulation results for the Avrami exponents in the $3D$ system are shown, in the case $S = 0.5$ and with both types of nucleation: preexisting and continuous. It can be seen how in the constant $D$ case the exponents reach a constant value while in the variable $D$ case, a diminution of the exponents is observed.

In contrast, in the $2D$ case, a reduction in the kinetics is also obtained but not as much as predicted by the *geometrical+mean-field* model. However, the Avrami exponents evolution along the transformation is qualitatively the same as the predicted: it reaches the expected low values at the end in contrast with the evolution of the *geometrical* and the *mean-field* models in which the exponents remain constant at the value for a diffusion controlled growth. That difference between the two and three-dimensional simulation and the *geoemtrical+mean-field* model can be understood taking into account the fact that this model was used to explain the actual primary crystallization of the metallic glass FINEMET, that is, a $3D$ system and then, it is not necessaryly suitable to reproduce $2D$ primary crystallization. Additionally, it can be argued that $2D$ systems are not physical. We are not simulating a $2D$ growth in a $3D$ system, but a $2D$ growth in a $2D$ system. But these results can become useful in the study of primary crystallization in thin films, a system that can be considered as $2D$ in a first approximation. The kinetics of primary crystallization in these systems is also studied on the KJMA framework [116, 117, 118], then, looking to figures 4.6-4.8 it can be stated that for low values of the supersaturation, the *geometrical+mean-field* model is still a valid approach to the crystallization, implying the important role of the compositional dependent diffusion coefficient. In contrast, for high supersaturations, it seems that this dependence is not so important and the *mean-field* model is the one that reproduces better the growth of the crystallites.

### 4.3.3 Transformations with continuous nucleation

As the spatial discretization used in the simulations with a varying diffusion coefficient is set to $\Delta x = 0.0025$, the initial number of cells that must be set to the value corresponding to the transformed phase can be seen in the last column of table 3.4. As before, initial radius with less number of cells are not stable and thus, dissolve. The $Q$ parameter does not depend on the diffusion

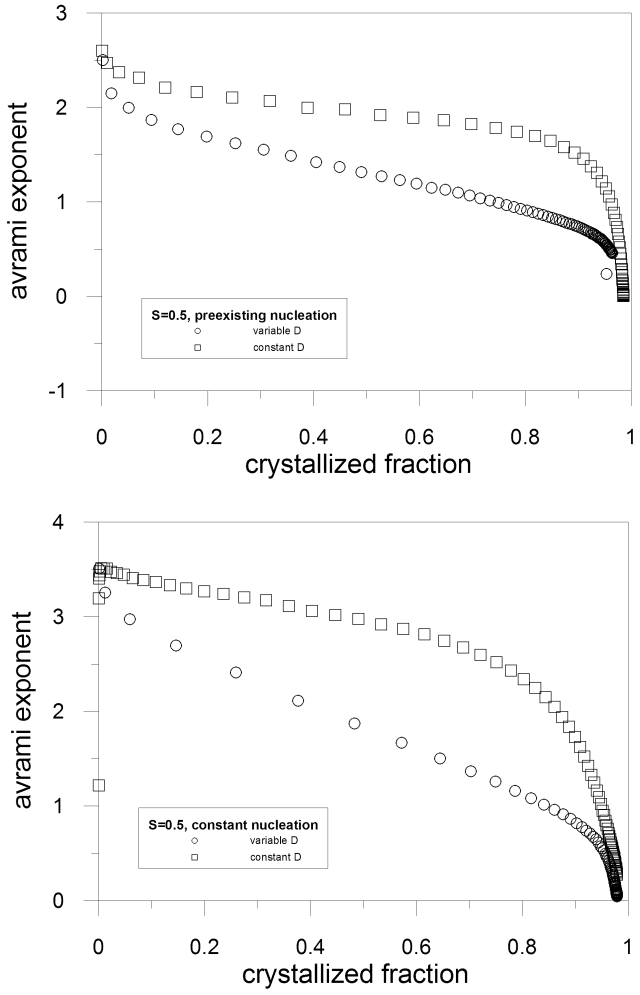


Figure 4.9: Avrami exponents for preexisting (top) and continuous (bottom) nucleation in $3D$ aand $S = 0.5$. Circles correspond to simulations with a variable diffusion coefficient while squares correspond to simulations with a constant diffusion coefficient

coefficient and accordingly, the values of table 3.5 are used in this section.

The transformed fraction evolution as well as the Avrami exponents obtained with a phase-field model simulation with a concentration dependent diffusion coefficient and continuous nucleation are shown in figures 4.10-4.12. These simulated curves are, again, compared with the theoretical models. In contrast with the preexisting nucleation case, the agreement between the phase-field model and the *geometrical+mean-field* model is excellent in all the cases, regardless the dimensionality of the system. In all the cases, the slower kinetic obtained in actual primary crystallization is reproduced and the evolution of the Avrami exponents is also well predicted. Depending on the supersaturation, this agreement is slightly different. For high supersaturations, the simulated transformed fraction follows almost perfectly the *geometrical+mean-field* model, specially for $S = 0.5$. In contrast, for the lowest supersaturation studied ($S = 0.2$) in the $3D$ case the theoretical model is slower than the simulations up to the half of the transformation whereas is faster afterwards. That behaviour, but with smaller differences, can also be seen in the $2D$ case. This also happens with higher supersaturations but with smaller differences, thus not affecting significantly the transformed fraction. Nevertheless, the expected slower kinetics is also reproduced as well as the evolution of the Avrami exponents as the transformation proceed. Similarly, the evolution of the nuclei density is also well reproduced. In figure 4.13, it is shown the nuclei density evolution for the $S = 0.5$ case and it can be seen how the models yield a good agreement with the phase-field model simulations.

Thus, in the two nucleation protocols studied, the experimentally expected kinetics in a primary crystallization is well modelled introducing a compositional dependent diffusion coefficient in the phase-field model simulations.

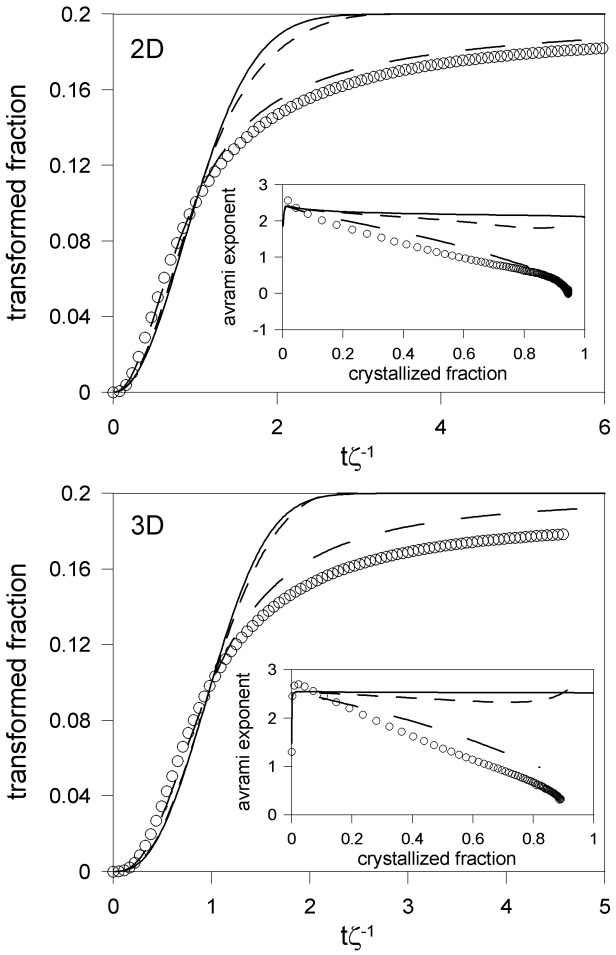


Figure 4.10: Transformed fraction and Avrami exponents for transformations with continuous nucleation and $S = 0.2$ in $2D$ and $3D$. Symbols: phase-field simulation; solid line: *geometrical* model; dashed line: *mean-field* model; and long dashed line: *geometrical+mean-field* model.

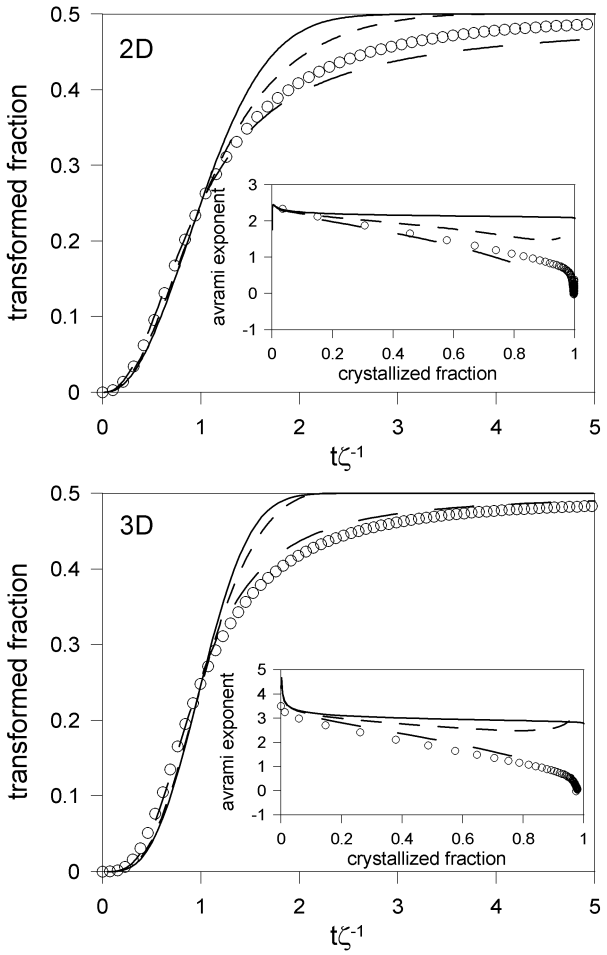


Figure 4.11: Transformed fraction and Avrami exponents for transformations with continuous nucleation and $S = 0.5$ in $2D$ and $3D$. Symbols: phase-field simulation; solid line: *geometrical* model; dashed line: *mean-field* model; and long dashed line: *geometrical+mean-field* model.

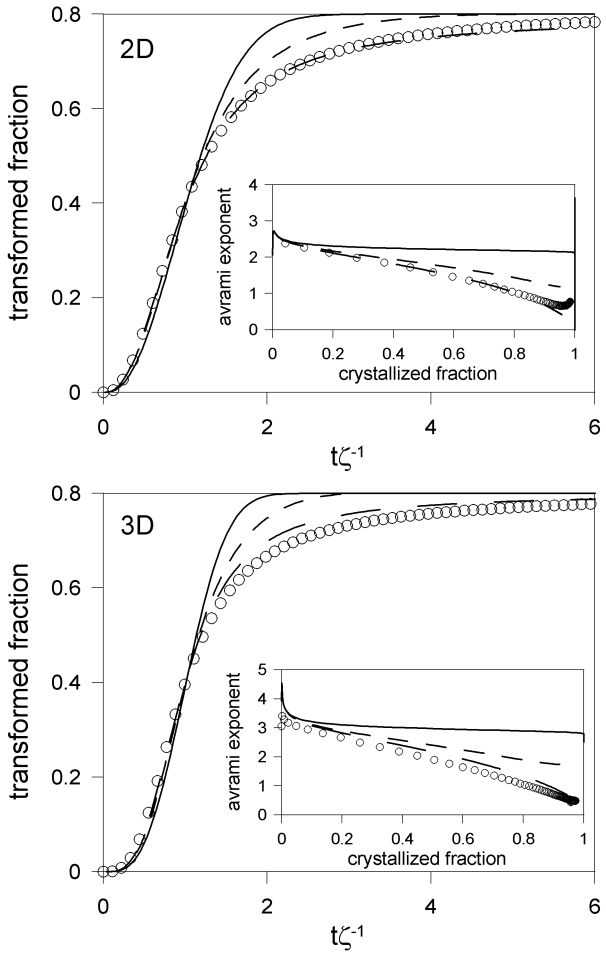


Figure 4.12: Transformed fraction and Avrami exponents for transformations with continuous nucleation and $S = 0.8$ in $2D$ and $3D$. Symbols: phase-field simulation; solid line: *geometrical* model; dashed line: *mean-field* model; and long dashed line: *geometrical+mean-field* model.

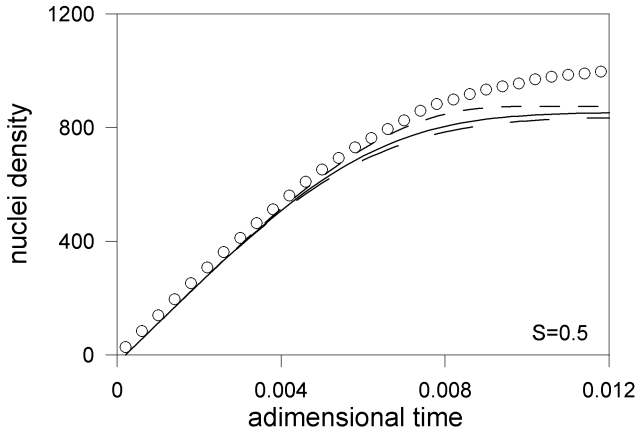


Figure 4.13: Nuclei density for simulations with continuous nucleation in $3D$, $S = 0.5$ and a compositional dependent diffusion coefficient. Symbols: phase-field simulation; solid line: *geometrical* model; dashed line: *mean-field* model; and long dashed line: *geometrical+mean-field* model.

# Chapter 5

# Conclusions

The aim of this thesis was to study primary crystallization kinetics by means of phase-field model simulations. Experimental data of this kind of transformations obtained from calorimetric studies is usually analyzed in the framework of the KJMA model. The KJMA equation that yields the temporal evolution of the transformed fraction is derived with two main assumptions: *(a)* a random distribution of particle nuclei and *(b)* isotropic growth with direct impingement. However, in primary crystallization the overlap of the concentration gradients that surrounds the particles breaks these two assumptions. On one hand, the impingement between the growing grains is not directly through its interfaces but through the concentration gradients, the so called soft-impingement effect. On the other hand, the evolution of these concentration gradients produces changes in the matrix concentration, stabilizing the areas surrounding the grains and thus, inducing a non-random nucleation. Thus, the slower kinetics observed in primary crystallization compared with the KJMA model was attributed to these two effects. In order to overcome these problems, modifications of the KJMA equation have been used on the basis of geometrical considerations (the exhaustion of the available space makes the growth rate slower) or mean-field approaches (the kinetics parameters diminishes as the transformation proceed). Nevertheless, these modified KJMA models are not able to reproduce the observed kinetics in primary crystallization. In order to take into account the soft-impingement effect in a reallistic way, the diffusion equation must be solved in all the space. And that can be done with phase-field models through the introduction of the phase-field variable that takes different values in each of the existing phases in the transformation. Moreover, phase-field model simulations also allow to use different nucleation protocols and thus, study the effect of the non-random nucleation on the primary crystallization kinetics.

The results of this thesis can be divided in three aspects. First of all, the most used equation in the analysis of calorimetric data is the KJMA equation with the transformed fractions (real and extended) normalized by the final value of the crystallized fraction. This normalization stands for the exhaustion of the space but it is not clearly justified. Thus, we derived this equation on the basis

of geometrical considerations and valid for any value of the supersaturation of the system, yelding a theoretical background to the use of this equation in experimental data. Secondly, phase-field model simulations of primary crystallization with three different values for the supersaturation and two nucleation protocols (preexisting nuclei and constant nucleation) were performed. These simulations (in 2 and $3D$) were compared to the modified KJMA equations and to the model that reproduces the experimental results obtained from the nanocrystallization of the metallic glass FINEMET. The obtained transformed fraction evolution does not reproduce the experimental data. On the contrary, phase-field model simulations allow us to conclude that the modified KJMA equations are a good first-order approach to transformations with soft-impingement and non-random nucleation. Thus, these two effect are not the responsible of the slower kinetics observed. Finally, it has been proposed that the compositional changes in the amorphous matrix have an important effect in the kinetics. As the transformation proceed, these changes in the amorphous precursor lead to changes in its structure modifying locally the glass transition temperature. As the viscosity is very sensible to the glass transition temperature, these changes in the amorphous produces changes in the atomic transport properties. That has been modelled through a compositional dependent diffusion coefficient on the basis of a modified Stokes-Einstein relation between viscosity and diffusion coefficient. The functional dependence of the diffusion coefficient with composition has been chosen in order to reproduce variations of the glass transition temperature with composition of the same order of magnitude than the experimentally observed. Phase-field model simulations with this diffusion coefficient yield the expected slower kinetics, showing an excellent agreement with the observed kinetics in primary crystallization of metallic glasses. Hence, phase-field model simulations confirm that are the atomic transport properties the ones that rule this kind of transformations.

This work can be extended in three main points. First of all, the phase-field method has revealed as a useful tool to study the kinetics of primary crystallization and it is also a well-known tool for studying microstructures. Thus, the following step will be the microstructural study of primary crystallization computing the size distribution of the nanocrystals and its evolution and comparing it with the existing models. Secondly, the simulations of this thesis have been compared with a model that reproduces the experimental results from a particular metallic glass (FINEMET). Thus, notwithstanding the fact that a varying diffusion coefficient seems to be the responsible of the kinetics, the particular dependence of it on the concentration may vary with the particular metallic glass studied. Thus, several primary crystallizations can be studied and compared to phase-field model simulations to check if the dependence proposed in this work is or is not general for any metallic glass. Finally, some improvements can be done in the analysis of the simulations. As explained in the corresponding chapter, we consider the transition from interface to diffusion-controlled growth sharp. Additionally, in order to calculate the interface velocity we need the value of the concentration at the interface, value that we fix to $-0.5$. But as the crystallite grows the concentration at the interface changes, and thus the interface velocity

also changes modifying the moment in which the growth regime takes place. Thus, a better modelling of this transition can be done as a further work of this thesis.

# Bibliography


[1] Y. Yoshizawa, S. Oguma and K. Yamauchi, J. Appl. Phys., **64**, 6044 (1988)

[2] Y. Yoshizawa, K. Yamauchi, Mater. Trans., JIM, **31**, 307 (1990)

[3] T.H. Noth, M.B. Lee, H.J. Kim and I.K. Kang, J. Appl. Phys., **67**, 5568 (1990)

[4] K. Hono, K. Hiraga, Q. Wang, A. Inoue and T. Sakurai, Surf. Sci., **266**, 385 (1992)

[5] G. Herzer, Phys. Scr., **T49**, 307 (1993)

[6] N. Clavaguera and J.A. Diego, Intermetallics, **1**, 187 (1993)

[7] J.A. Diego, M.T. Clavaguera-Mora and N. Clavaguera, Mat. Sci. & Eng. A, **179-180**, 526 (1994)

[8] K. Nazako, Y. Kawamura, A.P. Tsai and A. Inoue, Appl. Phys. Lett., **63**, 2644 (1993)

[9] T. Benameur and A. Inoue, Mat. Sci. Forum, **179-181**, 813 (1995)

[10] R. Wagner and R. Kampmann, Mat. Sci. and Tech., **5**, 213 (1991)

[11] M.E. Mc.Henry, M.A. Willard and D.E. Laughlin, Progr. Mat. Sci., **44**, 291 (1999)

[12] Y.H. Kim, A. Inoue and T. Masumoto, Mater. Trans. J.I.M., **31**, 747 (1990)

[13] H. Chen, Y. He, G.J. Shiflet and S.J. Poon, Scr. Metall. Mater., **25**, 1421 (1991)

[14] K. Suzuki, N. Kataoka, A. Inoue and T. Masumoto, Mater. Trans. J.I.M., **32**, 93 (1991)

[15] J.J. Croat, J.F. Herbst, R.W. Lee and F.E. Pinkerton, J. Appl. Phys., **55**, 2078 (1984)

[16] J.R. Davis (Ed.), 'Cast Iron', ASM Speciality Handbook, **81**, USA (1996)

[17] S. Dawson, JOM, **44** (1994)

[18] C.D. Van Siclen, Phys. Rev. B, **54**, 11845 (1996)

[19] A. Almansour, K. Matsugi, T. Hatayama and O. Yanagisawa, Mater. Trans. J.I.M., **37**, 1595 (1996)

[20] M. Tomellini and M. Fanfoni, Phys. Rev. B, **55**, 14071 (1997)

[21] M.D. Ediger, C.A. Angell and S.R. Nagel, J. Phys. Chem., **100**, 13200 (1996)

[22] P.G. Debenedetti and F.H. Stillinger, Nature, **410**, 259 (2001)

[23] H. Vogel, Phys. Zeit, **22**, 645 (1921)

[24] G. Tammann and W. Hesse, Z. Anorg. Allg. Chem, **156**, 245 (1926)

[25] G.S. Fulcher, J. Am. Ceram. Soc., **8**, 339 (1925)

[26] A. van den Beukel, Acta Metall. Mater., **42**, 1273 (1994)

[27] F.E. Luborsaky, "Amorphous metallic alloys", Butterworth Monographs in Materials, London (1983)

[28] F. Faupel, W. Frank, M-P. Macht, V. Naundorf, K. Rätzke, H. Schober, S. Sharma and H. Teichler, Rev. Mod. Phys., **75**, 237 (2003)

[29] H.H. Liebermann, Mater. Sci. Eng., **43**, 203 (1980)

[30] H.W. Kui, A.L. Greer and D. Turnbull, Appl. Phys. Lett., **45**, 615 (1984)

[31] H.J. Leamy and A.G. Dirks, J. Phys. D, **10**, L95 (1977)

[32] C.C. Koch, O.B. Cavin, C.G. McKamey and J.O. Scarbrough, Appl. Phys. Lett., **43**, 1017 (1983)

[33] A. Inoue, N. Nishiyama and T. Matsuda, Mat. Trans. JIM, **37** (1996)

[34] W.H. Wang, C. Dong and C.H. Shek, Materials Science and Engineering R, **44**, 45 (2004)

[35] M Volmer and A.Weber, Z. Phys. Chem., **119**, 227 (1926)

[36] R. Becker and W. Döring, Ann. Phys., **24**, 719 (1935)

[37] D. Turnbull, J. Appl. Phys., **21**, 1022 (1950)

[38] K.F. Kelton, A.L. Greer and C.V. Thompson, J. Chem. Phys., **79**, 6261 (1983)

[39] J.W. Christian, "The theory of Transformations in Metals and Alloys", Pergamon Press, Oxford (1975)

[40] J. D. Gunton, J. Stat. Phys. **95,** 903 (1999)

[41] M.C. Weinberg, J. Non-Cryst. Solids, **255**, 1 (1999)

[42] K.F. Kelton, Intermetallics, **14**, 966 (2006)

[43] C. Zener, J. App. Phys., **20**, 950 (1949)

[44] H.B. Aaron, D. Fainstein and G.R. Kotler, J. App. Phys., **41**, 4404 (1970)

[45] W. W. Mullins, and R. F. Sekerka, J. Appl. Phys., **34**, 323 (1963).

[46] Y. Couder, J. Maurer, R. Gonzalez-Cinca and A. Hernández-Machado, Phys. Rev. E **71**, 031602 (2005).

[47] U. Koster, U. Herold, H. G. Hillenbrand, and J. Denis, J. Mater. Sci., **15**, 2125 (1980) .

[48] M. T. Clavaguera-Mora, N. Clavaguera, D. Crespo, and T. Pradell, Prog. Mater. Sci., **47**, 559 (2002).

[49] A. N. Kolmogorov, Dokl. Akad. Nauk SSSR, Phys. Ser., 1**,** 355 (1937).

[50] W. A. Johnson, and P. A. Mehl, Trans. AIME, **135**, 416 (1939).

[51] M. Avrami, J. Chem. Phys., **7**, 1103 (1939); J. Chem. Phys., **8**, 212 (1940); J. Chem. Phys., **9**, 177 (1941).

[52] M.C. Weinberg, J. Non-Cryst. Solids, **127**, 161 (1991)

[53] T. Pradell, D. Crespo, N. Clavaguera, and M. T. Clavaguera-Mora, J. Phys.: Cond. Mat., 10**,** 3833 (1998).

[54] A. Korobov, J. Math. Chem., **24**, 261 (1998).

[55] V. Sessa, M. Fanfoni, and M. Tomellini, Phys. Rev. B, **54**, 836 (1996) .

[56] P. Uebele, and H. Hermann, Model. Simul. Mater. Sci. Eng., **4**, 203 (1996) .

[57] E. Pineda, T.Pradell, and D. Crespo, Philos. Mag. A, **82**, 107 (2002).

[58] M. P. Shepilov, and D. S. Baik, J. Non-cryst. Solids, 171**,** 141 (1994).

[59] D. P. Birnie, and M. C. Weinberg, J. Chem. Phys., **103**, 3742 (1995).

[60] F. S. Ham, J. Phys. Chem. Solids, **6,** 335 (1958).

[61] J.W. Cahn, Acta metall, **4**, 449 (1956)

[62] K.F. Kelton, J. Non-cryst. Solids, **163**, 283 (1993)

[63] O.R. Myhr and O. Grong, Acta mater, **48**, 1605 (2000)

[64] D. R. Uhlmann, J. Non-Cryst. Solids, **7,** 337 (1972).

[65] D. Hampel, A. Pundt, and J. Hesse, J. Phys: Condens. Matter, **4,** 3195 (1992).

[66] A. Cserei, J. Jiang, F. Aubertin, and U. Gonser, J. Mat. Sci., **29**, 1213 (1994).

[67] D. Jacovkis, Y. Xiao, J. Rodriguez-Viejo, M. T. Clavaguera-Mora, and N. Clavaguera, Acta Mater., **52**, 2819 (2004).

[68] M. P. Shepilov, J. Non-cryst. Solids, **208,** 64 (1996).

[69] D. R. Allen, J. C. Foley, and J. H. Perepezko, Acta Mater., **46**, 431 (1997).

[70] E. Ben-Jacob, I. Cohen and H. Levine, Advances in Physics, **49**, 395 (2000)

[71] D.M. Anderson, G.B. McFadden and A.A. Wheeler, Ann. Rev. of Fluid Mech., **30**, 139 (1998)

[72] J.D. van der Walls, Z. Phys. Chem., **13**, 657 (1894)

[73] J.W. Cahn and J.E. Hilliard, J. Chem. Phys., **28**, 258 (1958)

[74] J.W. Cahn, Acta Metall., **9**, 795 (1961)

[75] S.M. Allen and J.W. Cahn, J. Phys., **38**, C7 (1977)

[76] P.C. Hohenberg and B.I. Halperin, Rev. Mod. Phys., **49**, 435 (1977)

[77] L.Q. Chen, Annu. Rev. Mater. Res., **32**, 113 (2002)

[78] R. González-Cinca, L. Ramírez-Piscina, J. Casademunt and A. Hernández-Machado, Phys. Rev. E, **63**, 051602 (2001)

[79] H-J. Jou and M.T. Lusk, Phys. Rev. B, **55**, 8114 (1997)

[80] P. Shewmon, "Diffusion in solids", The Minerals, Metals & Materials Society, Pennsylvania (1989)

[81] G.B. Fedorov, "Mobility of atoms in crystal lattices", edited by V.N. Svechnikov, 1970

[82] H. Mehrer, "Diffusion in Solid Metals and Alloys", Landolt-Börnstein, New Series, Group III, **26**, Springer, Berlin (1990)

[83] F. Faupel, K. Rätzke and P. W. Hüppe, , Defect Diffus. Forum, **95-98**, 1175 (1993)

[84] F. Spaepen, "Physics of defects", edited byR. Balian, M. Kléman and J.P, Poirer, North-Holland, Amsterdam, 135 (1981)

[85] W. Götze and A. Sjölander, Rep. Prog. Phys., **55**, 241 (1992)

[86] S.L. Wang, R.F. Sekerka, A.A. Wheeler, B.T. Murray, S.R. Coriell, R.J. Braun and G.B. McFadden, Physica D, **69**, 189 (1993)

[87] R. González-Cinca, L. Ramírez-Piscina, J. Casademunt, A. Hernández-Machado, T. Tóth Katona, T. Börzsönyi and Á. Buka, J. Cryst. Growth, **193**, 712 (1998)

[88] J.S. Langer, Rev. Mod. Phys., **52**, 1 (1980)

[89] R. González-Cinca, "A phase-field model study of pattern formation in crystal growth" Thesis. (2000)

[90] L. Gránásy, T. Pusztai and J. Warren, J. Phys.: Condens. Matter., **16**, R1205 (2004)

[91] D. Fan and L.Q. Chen, Acta Mater., **45**, 611 (1996)

[92] I. Steinbach, F. Pezzola, B. Nestler, M. Seesselberg, R. Prieler, G. Schmitz and J.L.L. Rezende, Physica D, **94**, 135 (1996)

[93] A. Karma and W.J. Rappel, Phys. Rev. E, **57**, 4323 (1998)

[94] L.Gránázy, T. Börzsönyi and T. Pusztai, Phys. Rev. Lett., **88**, 206105 (2002)

[95] L.Gránázy, T. Börzsönyi and T. Pusztai, J. Cryst. Growth, **237-239**, 1813 (2002)

[96] K.R. Elder and M. Grant, Phys. Rev. E, **70**, 051605 (2004)

[97] W.H. Press, S.A. Teukolsky, W.T. Vetterling and B.P. Flannery. "Numerical Recipes in Fortran" Cambridge University Press, Cambridge, second edition (1992)

[98] S-K. Chan, J. Chem. Phys., **67**, 5755 (1977)

[99] P. Bruna, E. Pineda, R. González-Cinca and D. Crespo, J. Appl. Phys., **100**, 054907 (2006)

[100] H. Hermann, Europhys. Lett., **41**, 245 (1998)

[101] H. Hermann, Europhys. Lett., **51**, 127 (2000)

[102] P.Bruna, E.Pineda, D.Crespo and R.González-Cinca, in "Solid State Transformation and Heat Treatment", edited by Hazotte, Alain, ISBN 3-527-31007-X, Wiley-VCH, Weinheim (2004)

[103] D. Turnbull and M.H. Cohen, J. Chem. Phys., **29**, 1049 (1958)

[104] M.H. Cohen and D. Turnbull, J. Chem. Phys., **34**, 120 (1961)

[105] F. Spaepen, "Les Houches Lectures on Physics of Defects", edited by J. J. Poirer and M. Kleman. North Holland, Amsterdam (1979)

[106] A. van den Beukel, Scripta metall., **22**, 887 (1988)

[107] A. van den Beukel, Acta metall. mater., **39**, 2709 (1991)

[108] P.A. Duine, J. Sietsma and A. van den Beukel, Phis. Rev. B, **48**, 6957 (1993)

[109] M.H. Cohen and G.S. Grest, Phys. Rev. B, **20**, 1077 (1979)

[110] M. Mao, Z. Altounian and D.H. Ryan, J. Non-Cryst. Solids, **205-207**, 476 (1996)

[111] S.Özdemir Kart, M. Tomak, M. Uludogan and T. Çagin, Mat. Sci. Eng. A, **435-436**, 736 (2006)

[112] J. Torrens-Serra, P. Bruna, J. Rodríguez-Viejo, M.T. Clavaguera-Mora and T. Pradell, in "Industrial Applications of the Mössbauer Effect", edited by M. Gracia, J.F. Marco and F. Plazaola, American Institute of Physics, pag. 250 (2005)

[113] G. Wang, J. Shen, J.F. Sun, B.D. Zhou, J.D. Fitz Gerald, D.J. Llewellyn and Z.H. Stachurski, Scripta Materialia, **53**, 641 (2005)

[114] M.P. Macht, V. Naundorf, P. Fielitz, J. Rüsing, Th. Zumkley and G. Frohberg, Mat. Sci. Eng. A, **304-306**, 646 (2001)

[115] P. Bruna, E. Pineda, R. González-Cinca, T. Pradell and D. Crespo, TMS Letters, **2**, 11 (2005)

[116] Q.Z. Hong, K. Barmak and L.A. Clavenger, J. Appl. Phys., **72**, 3423 (1992)

[117] X. Dong and J. Wu, Mat. Sci. Eng. A, **339**, 297 (2003)

[118] T. Missana, C.N. Afonso, A.K. Petford-Long and R.C. Doole, Phil. Mag. A, **79**, 2577 (1999)